LBL-11518

Lawrence Berkeley Laboratory
UNIVERSITY OF CALIFORNIA

Materials & Molecular Research Division

MASTER

WAVE MIXING SPECTROSCOPY

Robert William Smith
(Ph.D. Thesis)

August 1980

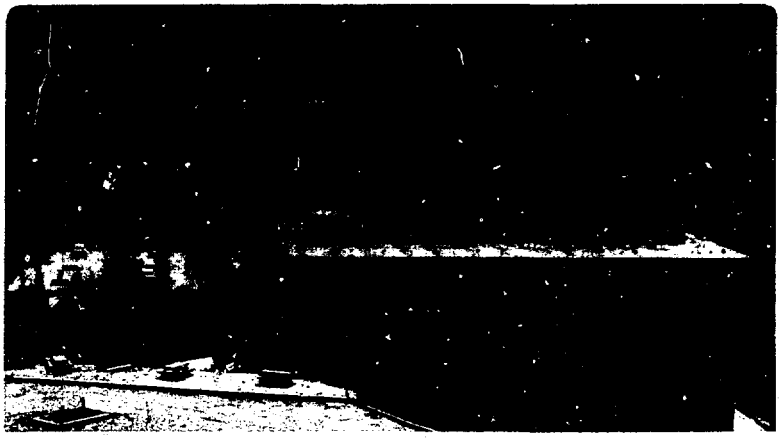

Prepared for the U.S. Department of Energy under Contract W-7405-ENG-48

DISTRIBUTION OF THIS DOCUMENT IS UNLIMITED

DISCLAIMER

This book was prepared as an account of work sponsored by an agency of the United States Government. Neither the United States Government nor any agency thereof, nor any of their employees, makes any warranty, express or implied, or assumes any legal liability or responsibility for the accuracy, completeness, or usefulness of any information, apparatus, product, or process disclosed, or represents that its use would not infringe privately owned rights. Reference herein to any specific commercial product, process, or service by trade name, trademark, manufacturer, or otherwise, does not necessarily constitute or imply its endorsement, recommendation, or favoring by the United States Government or any agency thereof. The views and opinions of authors expressed herein do not necessarily state or reflect those of the United States Government or any agency thereof.

a

Wave Mixing Spectroscopy

Robert William Smith
Lawrence Berkeley Laboratory
University of California, Berkeley 94720

ABSTRACT

We have investigated several new aspects of nonlinear or wave mixing spectroscopy, utilizing the polarization properties of the nonlinear output field and the dependence of this field upon the occurrence of multiple resonances in the nonlinear susceptibility.

First, it is shown theoretically that polarization-sensitive detection may be used to either eliminate or controllably reduce the nonresonant background in coherent anti-Stokes Raman spectroscopy (CARS), allowing weaker Raman resonances to be studied. These new four-wave mixing techniques are called background suppression-CARS and optical heterodyned detection-CARS. These are experimentally demonstrated by studying the 992 cm^{-1} Raman mode of benzene diluted in carbon tetrachloride, with an attained detection sensitivity of 100 ppm of benzene. This corresponds to a ratio of resonant to nonresonant susceptibilities of about 4×10^{-3}. A discussion of experimental techniques, possible applications, and limitations of these techniques are also given.

The features of multi-resonant four-wave mixing are examined in the case of an inhomogeneously broadened medium. It is found that the linewidth of the nonlinear output narrows considerably (approaching the homogeneous width) when the quantum mechanical expressions for the doubly- and triply-resonant susceptibilities are averaged over a Dop-

DISTRIBUTION OF

pler or strain broadened profile. Experimental studies of nonlinear processes in Pr^{+3}:LaF_3 verify this linewidth narrowing, but indicate that this strain broadened system cannot be treated with a single broadening parameter as in the case of Doppler broadening in a gas. We also measure several susceptibilities from which we deduce dipole matrix elements and Raman polarizabilities related to the $^3H_4$, $^3H_6$, and $^3P_0$ levels of the praseodymium ions.

DEDICATION AND ACKNOWLEDGEMENTS

This thesis is dedicated to my wife, Sandra, and my children, Emily and Melany, whose loving devotion and sacrifice have made this thesis a reality.

There are many other people to whom I am indebted for their support during the course of this work. I would like to particularly thank:

Professor Y. R. Shen for his guidance and patience during my research and in the preparation of this thesis and for instilling in me his high standards of physics;

Drs. Donald Bethune, Steven Chu, and Jean-Louis Oudar, co-workers and co-authors, who have imparted to me their wisdom of experimental physics;

Alex Jacobson, Chenson Chen, Ray Hsu, Gary Boyd and the other fellow students and post-docs of the Shen Group who were always available for discussions of life and science;

Rita Jones and Gloria Pelatowski for their expert assistance in preparing this manuscript.

This work was supported by the Division of Materials Sciences, Office of Basic Energy Sciences, U. S. Department of Energy under Contract 7405-ENG-48.

TABLE OF CONTENTS

	Page
I. INTRODUCTION	1
II. REVIEW OF FOUR-WAVE MIXING SPECTROSCOPY	5
A. Semiclassical Theory of Nonlinear Optics	5
B. Physical Properties of the Nonlinear Output Field	9
C. Analysis Techniques	11
D. Stimulated Raman Processes vs. Signal Generation Processes and Specific Examples	24
E. Signal to Noise Analysis	39
References	50
Figure Captions	52
Figures	54
III. EXPERIMENTAL DEMONSTRATION AND DISCUSSION OF BACKGROUND SUPPRESSION-CARS AND OPTICAL HETERODYNED DETECTION-CARS	62
A. The Standard Amplitude-CARS Technique and Apparatus	63
B. Polarization-Sensitive CARS Techniques and Apparatus	67
C. Background Suppression- and Optical Heterodyned Detection-CARS: Experimental Measurements and Analysis	72
D. Applications and Limitations of Polarization-Sensitive CARS Techniques	86
References	96
Figure Captions	98
Figures	100
IV. MULTI-RESONANT FOUR-WAVE MIXING IN INHOMOGENEOUSLY BROADENED MEDIA — THEORY	110
A. Multi-Resonant Nonlinear Susceptibilities	111

Page

B. Inclusion of Inhomogeneous Broadening 116

C. Effects of One-Photon Absorption 125

References 129

Figure Captions 131

Figures 132

V. MULTI-RESONANT FOUR-WAVE MIXING IN INHOMOGENEOUSLY BROADENED MEDIA — EXPERIMENT 135

A. Sample — $Pr^{+3}:LaF_3$ 136

B. Linear Absorption: $^3H_4 \rightarrow {}^3P_0$ 138

C. Triply-Resonant RIKES 143

D. Doubly-Resonant CARS — Raman Resonance 151

E. Doubly-Resonant CARS — Upper State Resonance 161

References 165

Figure Captions 167

Figures 169

I. Introduction

The primary goal of general spectroscopy is to provide information about the physical properties of materials through the use of external probes. In particular, the interaction of matter and radiation, optical spectroscopy, has been extremely fruitful in obtaining data on material transitions and excitations. The development of the laser has further stimulated the growth of this area of spectroscopy, with such techniques as Raman scattering and Brillouin scattering being commonly utilized. The demonstration of tunable dye lasers in the late 1960's has led to the development of yet another form of spectroscopy — nonlinear or wave mixing spectroscopy.

Four-wave mixing spectroscopy, one of the better known examples, involves the interaction of three optical fields within a medium to create a fourth coherent optical field. The coupling between these fields is embodied in the nonlinear optical susceptibility, which contains all pertinent information about the material system, e.g. the characteristic resonances. With frequency-tunable input fields it is possible to probe the material excitations through the resonant interaction, thus observing resonant enhancement of the output field. In this way, four-wave mixing may be used as a form of spectroscopy which should be observable in media of any macroscopic symmetry.

Wave mixing spectroscopy has many advantages over the conventional forms of linear spectroscopy, e.g. spontaneous Raman scattering. First of all, the nonlinear techniques are coherent with the output field propagating in a well defined direction. Such collimated output allows collection efficiencies to approach unity and discriminates

against unwanted background fluorescence. This, together with the fact that the nonlinear signals are usually much stronger than spontaneous signals, greatly reduces the time required to make a spectrum (nonlinear spectra require only minutes compared to the hours necessary to make some spontaneous spectra). Also, in coherent forms of spectroscopy, the frequency resolution is determined by the linewidths of the input lasers (as low as 10^{-4} cm^{-1}), rather than the bandpass of the detection system as in spontaneous scattering experiments. Finally, using pulsed lasers, it is possible to obtain time resolved studies of transient phenomena. Exploiting these features, four-wave mixing spectroscopy has been applied to many areas of research, including high resolution spectroscopy, combustion research, and studies on highly fluorescent biological samples.

As the area of four-wave mixing spectroscopy matures, there are many variations of the basic wave mixing concept which have developed. In Section II we review the general formalism used to describe these effects, with emphasis placed on the various methods of analyzing the nonlinear output beam, i.e. polarized and unpolarized detection. The processes are then further classified by the frequency mixing involved, with stimulated Raman scattering-type processes (output frequency degenerate with an input frequency, e.g. Stimulated Raman Gain Spectroscopy, SRGS) distinguished from signal generation processes (output frequency distinct from the input frequencies, e.g. Coherent Anti-Stokes Raman Spectroscopy, CARS). We then describe the theoretical analysis of two new forms of four-wave mixing: background suppression-CARS and optical heterodyned detection-CARS. Using these new techniques it is possible to produce spectra dependent upon either

$|\chi_R|^2$, $\mathrm{Im}[\chi_R]$, or $\mathrm{Re}[\chi_R]$ (where χ_R is the resonant susceptibility) with the background nonresonant contribution to the signal either eliminated or greatly reduced. A formal signal to noise analysis of the various forms of CARS is performed to compare the techniques.

Section III contains the experimental demonstration of these new CARS techniques. We first discuss the general methods and apparatus used in conventional CARS, then include modifications needed to make polarization-sensitive measurements. Experimental spectra are presented of the 992 cm^{-1} Raman mode of benzene diluted in carbon tetrachloride, which confirm the expected lineshapes of the different techniques. Measurement of the ratio of resonant to nonresonant susceptibilities is analyzed and compared to previous work; and the minimum detectable value of this ratio is established. Possible applications and limitations of the polarization-sensitive CARS techniques are also discussed.

In the first part of this thesis, we consider four-wave mixing processes with only a single resonance (the most interesting case being two-photon resonances, e.g. Raman). In Section IV we include the possibility of multiple resonances in the nonlinear susceptibility, with explicit, quantum mechanical expressions presented for several doubly- and triply-resonant susceptibilities. We then consider the consequences of inhomogeneous broadening on these multi-resonant susceptibilities — the cases of Doppler broadening and strain broadening considered as examples. After averaging over such broadening, it is shown that in certain cases four-wave mixing processes show a linewidth narrowing that approaches the homogeneous width of the transition. Criteria are established to predict which processes will dis-

play this narrowing effect. The effects of linear absorption on the nonlinear output signal are also important in multi-resonant cases and are considered here in detail.

An experimental system used to examine the multi-resonant processes in the presence of strain broadening is described in Section V. Using the sharp electronic lines of Pr^{+3} ions doped in lanthanum trifluoride, the expected narrowing effects were observed (although the presence of "accidental degeneracy" broadened the nonlinear output). Measurements were also made to evaluate the strengths of the multi-resonant susceptibilities associated with the $^3H_4$, $^3H_6$, and $^3P_0$ levels of the Pr^{+3}, from which the values of the dipole matrix elements and Raman polarizability were determined. Although some values have large uncertainties, new experiments are proposed to improve the measurements.

II. REVIEW OF FOUR-WAVE MIXING SPECTROSCOPY

A. Semiclassical Theory of Nonlinear Optics

In the classical theory of radiation,[1] the electromagnetic fields are governed by Maxwell's equations with the properties of the material system introduced through the constitutive relations

$$\vec{D}(\omega) = \overleftrightarrow{\epsilon}(\omega)\vec{E}(\omega) \qquad \text{and} \qquad \vec{B}(\omega) = \overleftrightarrow{\mu}(\omega)\vec{H}(\omega).$$

In general, the Fourier components of the fields at frequency ω are coupled by electric and magnetic permeability tensors, $\overleftrightarrow{\epsilon}$ and $\overleftrightarrow{\mu}$ respectively, which are not only frequency dependent, but also field dependent. It is this nonlinear dependence of $\vec{D}$ on $\vec{E}$ which leads to the classical theory of most nonlinear optical phenomena (magnetic related phenomena will not be discussed here). In developing nonlinear optics theory,[2] interest is usually focused on the polarization vector $\vec{P} = (\vec{D} - \vec{E})/4\pi$ which contains the information about the material system and its nonlinearities. It is assumed that the nonlinear effects are small so the polarization can be expanded in a power series in the electric field

$$\vec{P}(\omega) = \overleftrightarrow{\chi}^{(1)}(-\omega,\omega) \cdot \vec{E}(\omega) + \overleftrightarrow{\chi}^{(2)}(-\omega,\omega_a,\omega_b):\vec{E}(\omega_a)\vec{E}(\omega_b)$$

$$+ \overleftrightarrow{\chi}^{(3)}(-\omega,\omega_a,\omega_b,\omega_c):\vec{E}(\omega_a)\vec{E}(\omega_b)\vec{E}(\omega_c) + \ldots \qquad (1)$$

The first term of this expansion is the linear response of the medium to the electric field $\vec{E}(\omega)$. It is described by the first-order susceptibility $\overleftrightarrow{\chi}^{(1)}$, of which the real part contributes to the linear refractive

index and the imaginary part determines the linear absorption at ω. The second-order term, restricted to $\omega = \omega_a + \omega_b$, describes nonlinear mixing processes involving two input fields, $\vec{E}(\omega_a)$ and $\vec{E}(\omega_b)$, such as sum-frequency generation or optical parametric amplification. The cubic field dependence of the next term is coupled to the polarization by the third-order nonlinear susceptibility $\overleftrightarrow{\chi}^{(3)}(-\omega,\omega_a,\omega_b,\omega_c)$ where now $\omega = \omega_a + \omega_b + \omega_c$. This term characterizes the parametric interaction of the "four-wave mixing" process and will be examined in detail in this thesis.

Greater insight can be given to the susceptibilities if we regard the medium as a quantum mechanical system, although still treating the fields as classical quantities. This is the semiclassical treatment, which is sufficient to describe stimulated emission phenomena, however it fails to predict any spontaneous emission phenomena. Expressions for the susceptibilities can be found using the density matrix formalism applied to perturbation theory of the electromagnetic interaction.[2] In particular the expression for $\overleftrightarrow{\chi}^{(3)}$ contains 48 terms.[3] Fortunately in most spectroscopic applications the particular resonance of interest appears in only a few of the possible terms, while the other terms remain essentially nondispersive. Often a formal separation of these terms is desirable

$$\overleftrightarrow{\chi}^{(3)} = \overleftrightarrow{\chi}^{(3)}_{NR} + \overleftrightarrow{\chi}^{(3)}_{R} \tag{2}$$

where $\overleftrightarrow{\chi}^{(3)}_{R}$ and $\overleftrightarrow{\chi}^{(3)}_{NR}$ are the resonant and nonresonant susceptibilities respectively.

The susceptibilities relate macroscopic fields, thus the quantum mechanical susceptibilities for individual atoms or molecules must be

suitably averaged over the spatial arrangement of the atoms or molecules. Therefore the tensor elements of $\overleftrightarrow{\chi}^{(3)}$ are constrained by the spatial symmetry of the macroscopic medium. Examination of all symmetries indicates that $\overleftrightarrow{\chi}^{(3)}$ is never necessarily identically zero, consequently "four-wave mixing" processes can occur in all materials. Since electric-dipole second-order processes are forbidden in isotropic media, third-order processes are the lowest order nonlinear effects observable in liquids and gases.

Returning to Maxwell's equations, we use the nonlinear polarization as a source term and write the driven wave equation for $\vec{E}(\omega)$ as

$$\nabla^2\vec{E}(\vec{r},\omega) + \frac{n^2(\omega)\omega^2}{c^2}\vec{E}(\vec{r},\omega) = -\frac{4\pi\omega^2}{c^2}\vec{P}^{(3)}(\vec{r},\omega) \tag{3}$$

where, $\vec{P}^{(3)}(\vec{r},\omega) \equiv \overleftrightarrow{\chi}^{(3)}(-\omega,\omega_a,\omega_b,\omega_c)\vdots\vec{E}(\vec{r},\omega_a)\vec{E}(\vec{r},\omega_b)\vec{E}(\vec{r},\omega_c)$ and all fields are assumed to be plane waves of the form

$$\vec{E}(\vec{r},\omega_j) = \vec{\mathcal{E}}(\vec{r},\omega_j)e^{i\vec{k}_j\cdot\vec{r}}.$$

The z-axis is chosen to coincide with $\vec{k}$, the output wavevector. Assuming the rate of change of $\vec{\mathcal{E}}(\vec{r},\omega)$ across one wavelength is small, we can write Eq. (3) as

$$\frac{\partial\vec{\mathcal{E}}(z,\omega)}{\partial z} = i\,\frac{2\pi\omega}{n(\omega)c}\,\overleftrightarrow{\chi}^{(3)}(-\omega,\omega_a,\omega_b,\omega_c)\vdots\vec{\mathcal{E}}(\omega_a)\vec{\mathcal{E}}(\omega_b)\vec{\mathcal{E}}(\omega_c)e^{i\Delta\vec{k}\cdot\vec{z}} \tag{4}$$

with $\Delta\vec{k} = \vec{k}_a + \vec{k}_b + \vec{k}_c - \vec{k}$ being the wavevector mismatch due in part to the linear dispersion of the refractive index and in part to the geometry of the wavevectors. Integration of Eq. (4) with the boundary of the

nonlinear medium at $z = 0$ yields

$$\vec{\mathcal{E}}(z,\omega) = \vec{\mathcal{E}}(0,\omega) + i\,\frac{2\pi\omega}{n(\omega)c}\,\overleftrightarrow{\chi}^{(3)}(-\omega,\omega_a,\omega_b,\omega_c) : \vec{\mathcal{E}}(\omega_a)\vec{\mathcal{E}}(\omega_b)\vec{\mathcal{E}}(\omega_c)\left\{\frac{e^{i\Delta\vec{k}\cdot\vec{z}} - 1}{i\Delta\vec{k}\cdot\hat{z}}\right\} \tag{5}$$

$\vec{\mathcal{E}}(0,\omega)$ is the field at ω incident on the nonlinear medium at $z = 0$. Here we assume the small signal limit, i.e. there is no depletion or alteration of the polarization state of the beams at ω_a, ω_b, ω_c as they propagate through the medium, although these assumptions may be lifted.[4]

The importance of the wavevector mismatch is shown by the bracketed term in Eq. (5), which has a maximum value of z when $\Delta\vec{k} = 0$ and falls to zero when $\Delta\vec{k}\cdot\vec{z} = 2\pi$. Thus we must ensure that $\Delta\vec{k}$ is minimized to have maximum output. In the normal experimental setup, one can usually control the directions of the beams to achieve phasematching in many possible ways. In some cases, the choice of four-wave mixing process gives automatic phasematching — independent of the beam geometry. More often though, the beam geometry determines both the phasematching and the interaction length, z, of the input beams. In the following discussion, it is assumed that phasematching has been achieved.

The output field of a four-wave mixing experiment is thus described by

$$\vec{\mathcal{E}}(z,\omega) = \vec{\mathcal{E}}(0,\omega) + i\beta\overleftrightarrow{\chi}^{(3)}(-\omega,\omega_a,\omega_b,\omega_c) : \vec{\mathcal{E}}(\omega_a)\vec{\mathcal{E}}(\omega_b)\vec{\mathcal{E}}(\omega_c) \tag{6}$$

where we define $\beta = \frac{2\pi\omega z}{n(\omega)c}$. This result follows using infinite plane waves, but the use of other beam profiles only alters the form of β. The analysis of this signal field depends only on the general form of Eq. (6), not the specific form of β, and is the subject of the next

part of this section.

B. Physical Properties of the Nonlinear Output Field

To begin the discussion of the analysis of the nonlinear output, we first enumerate the physical properties upon which this output field is dependent. In nonlinear optical experiments these are (1) the output frequency; (2) the polarization state of the output field; (3) the temporal behavior of the input beams and the response time of the medium; (4) the momentum-space dependence of the output. The latter two properties will not be considered here beyond the fact that we are concerned with steady-state, phasematched solutions to the wave equation as given in Eq. (6). Work in the time domain and momentum space can be found in the literature.[5,6] In this section emphasis will be placed on the spectral and polarization properties of the nonlinear output.

In all spectroscopy experiments the output field $\vec{\mathcal{E}}(z,\omega)$ is strongly dependent on the output frequency. It is this strong variation which allows these nonlinear techniques to be used as spectroscopic techniques. The spectral dependence of $\vec{\mathcal{E}}(z,\omega)$ is determined by the frequency dependence of the nonlinear susceptibility which is contained in the resonant part of $\overleftrightarrow{\chi}^{(3)}$. It is informative to show explicitly one term from the quantum mechanical expression for $\overleftrightarrow{\chi}_R^{(3)}$.[3] One term of

$$[\chi_R^{(3)}(-\omega,\omega_a,\omega_b,\omega_c)]_{ijk\ell} = \sum_{g,n,n'n''} \frac{Ne^4}{\hbar^3} \times \frac{\langle g|r_i|n''\rangle\langle n|r_j|g\rangle\langle n'|r_k|n\rangle\langle n''|r_\ell|n'\rangle\rho_{gg}^{(0)}}{(\omega_{ng}-\omega_a-i\Gamma_{ng})(\omega_{n'g}-(\omega_a+\omega_b)-i\Gamma_{n'g})(\omega_{n''g}-\omega-i\Gamma_{n''g})} \tag{7}$$

where, $\hbar\omega_{ng} = E_n - E_g$ is the energy difference and Γ_{ng} the phenomenolo-

gical damping constant between quantum states $|n\rangle$ and $|g\rangle$, $-e\langle n|r_j|g\rangle$ is the i th component of the electric dipole matrix element, $\rho_{gg}^{(0)}$ is the fractional population initially in state $|g\rangle$, and N is the density of particles. Examination of Eq. (7) shows both one-photon and two-photon resonances are included in $\overleftrightarrow{\chi}_R^{(3)}$. Single photon resonances, e.g. $\omega_a \rightarrow \omega_{ng}$, also appear in the linear susceptibility and thus can be probed through linear spectroscopy. The major interest in four-wave mixing spectroscopy has been to examine two-photon resonances, e.g. $\omega_a + \omega_b \rightarrow \omega_{n'g}$. Two-photon absorption (TPA) resonances occur when $\omega_a > 0$, $\omega_b > 0$; and Raman resonances occur when $\omega_a > 0$ and $\omega_b < 0$. The output frequency in either case is still $\omega = \omega_a + \omega_b + \omega_c$, where ω_c can be independently chosen. For example, choosing $\omega_c > 0$ we can monitor an infrared (Raman) transition and have the output frequency in the visible (where photomultipliers are more efficient). This is a very attractive feature of four-wave mixing spectroscopy.

Of equal interest to the spectral variation of the susceptibility is a complete description of the polarization properties of the output field $\vec{\mathcal{E}}(z,\omega)$. We show below that in general the polarization state of $\vec{\mathcal{E}}(z,\omega)$ is also dispersive, i.e., explicit expressions for parameters describing the polarization state show resonance behavior, similar to the resonant susceptibility. This allows the added freedom of polarization analysis of nonlinear signals to determine spectroscopic information.

To see that the output polarization state is dispersive we begin by rewriting Eq. (6) using the formal separation of Eq. (2)

$$\vec{\mathcal{E}}(\omega) = \vec{\mathcal{E}}(0,\omega) + i\beta\overleftrightarrow{\chi}_{NR}^{(3)}(-\omega,\omega_a,\omega_b,\omega_c)\vdots\vec{\mathcal{E}}(\omega_a)\vec{\mathcal{E}}(\omega_b)\vec{\mathcal{E}}(\omega_c) \qquad \text{cont'd}$$

$$+ i\beta\overleftrightarrow{\chi}_{\Gamma}^{(3)}(-\omega,\omega_a,\omega_b,\omega_c)\vdots\vec{\mathcal{E}}(\omega_a)\vec{\mathcal{E}}(\omega_b)\vec{\mathcal{E}}(\omega_c). \tag{8}$$

(The z-dependence of the output field will henceforth be suppressed.) We gather the first and second terms together and write Eq. (8) as

$$\vec{\mathcal{E}}(\omega) = \vec{\mathcal{E}}_{LO}(\omega) + \vec{\mathcal{E}}_{R}(\omega) \tag{9}$$

where $\vec{\mathcal{E}}_{LO}(\omega) \equiv \vec{\mathcal{E}}(0,\omega) + i\beta\overleftrightarrow{\chi}_{NR}^{(3)}(-\omega,\omega_a,\omega_b,\omega_c)\vdots\vec{\mathcal{E}}(\omega_a)\vec{\mathcal{E}}(\omega_b)\vec{\mathcal{E}}(\omega_c)$ and $\vec{\mathcal{E}}_{R}(\omega) \equiv i\beta\overleftrightarrow{\chi}_{R}^{(3)}(-\omega,\omega_a,\omega_b,\omega_c)\vdots\vec{\mathcal{E}}(\omega_a)\vec{\mathcal{E}}(\omega_b)\vec{\mathcal{E}}(\omega_c)$. Note that as the resonance is scanned $\vec{\mathcal{E}}_{LO}$ (the so-called local oscillator field) is unchanging, while the resonant field $\vec{\mathcal{E}}_{R}$ will vary in magnitude and changes phase relative to $\vec{\mathcal{E}}_{LO}$. The combination of these two fields leads to a total output polarization state which is dispersive. Only if $\vec{\mathcal{E}}_{R}$ and $\vec{\mathcal{E}}_{LO}$ are in the same polarization state will there be no dispersion in the output polarization state.

Thus we see that there are two physical properties of the output which allow four-wave mixing to be used as a spectroscopic technique. One can find the dispersion in the nonlinear susceptibility by measuring the variation of the output field amplitude. Or one can obtain similar information by determining the change in the output field's polarization state as the resonance is scanned. Detailed analysis of these techniques and possible hybrid techniques are discussed in section IIC.

C. Analysis Techniques

In this sub-section we consider four possible general forms of four-wave mixing spectroscopy experiments. Explicit expressions are given for the detected signal in each case, and the important features

of each technique are emphasized. The discussion begins with a description of the detection system to be considered.

In all of the experimental arrangements proposed, it is assumed that the optical detector, either photomultiplier or photodiode, is operated at light levels such that it is a perfect square-law detector. The important quantity is not the output field reaching the detector $\vec{\mathcal{E}}_D(\omega)$, but its square magnitude $|\vec{\mathcal{E}}_D|^2$. As part of the detection system, we include the possible use of a general elliptical polarization analyzer which transmits the polarization state $\hat{e}_\alpha$ to be described below. In this case only the α-component of output field actually arrives at the detector. It is assumed that the photocurrent is electronically processed and eventually displayed on a recorder versus the relevant frequency parameter. (In the last case considered below, we assume that the polarization analyzer is adjusted to give a null signal from the optical detector.)

It is useful at this point to review and define some terms related to the general elliptical polarization state.[7] Several sets of parameters are commonly used to describe the general polarization state. These are (1) the two components of the field along orthogonal axes, (2) the complex number which is the ratio of these two components and (3) the inclination angle of the semimajor axis and the eccentricity angle of the ellipse. Figure 1 shows the relationship between these pairs of parameters. A useful form for the general polarization unit vector is

$$\hat{e}_\alpha = (\cos\theta \cos\phi + i \sin\theta \sin\phi)\hat{x} + (\sin\theta \cos\phi - i \cos\theta \sin\phi)\hat{y} \qquad (10)$$

where θ is the inclination angle of the semimajor axis relative to an arbitrary x-axis, $0 \leq \theta < \pi$; and ϕ is the eccentricity angle, $\phi = \pm \tan^{-1}(b/a)$ as in Fig. 1, $-\pi/4 \leq \phi \leq \pi/4$. The sign of ϕ is taken positive for right elliptical polarizations, and negative for left elliptical polarizations. For example, $\theta = 0$, $\phi = \pi/4$ represents the right circular polarization state (RCP), $\theta = 0$, $\phi = -\pi/4$ represents left circular polarization (LCP), and states with $\phi = 0$ are linearly polarized. If $\hat{e}_\beta$ is polarization state orthogonal to $\hat{e}_\alpha$, we have for unit vectors

$$\hat{e}_\alpha^* \cdot \hat{e}_\beta = 0 \qquad \hat{e}_\alpha^* \cdot \hat{e}_\alpha = \hat{e}_\beta^* \cdot \hat{e}_\beta = 1 \qquad \hat{e}_\beta^* = \hat{z} \times \hat{e}_\alpha \tag{11}$$

$(\hat{e}_\alpha, \hat{e}_\beta, \hat{z})$ form a generalized orthonormal coordinate system to describe a vector field $\vec{\mathcal{E}}$ propagating in the z-direction. $\vec{\mathcal{E}}$ is separated into components as

$$\vec{\mathcal{E}} = (\hat{e}_\alpha^* \cdot \vec{\mathcal{E}})\hat{e}_\alpha + (\hat{e}_\beta^* \cdot \vec{\mathcal{E}})\hat{e}_\beta .$$

With this background we now return to the analysis of the four-wave mixing output field $\vec{\mathcal{E}}(\omega)$.

1. Amplitude Analysis

Amplitude analysis is the simplest form of analysis technique, and is thus the most widely used method in four-wave mixing spectroscopy.[8,9] The simplicity of this approach arises because no form of polarization analysis is performed, so the typical apparatus needs only the minimum equipment with the detection system consisting primarily of the optical detector. This type of experimental arrangement measures $|\vec{\mathcal{E}}(\omega)|^2$. The

appropriate physical quantity for this discussion is the optical intensity at the detector $I_D(\omega)$. Using Eq. (9), we have

$$I_D(\omega) = \frac{cn}{8\pi} |\vec{\mathcal{E}}_{LO}(\omega) + \vec{\mathcal{E}}_R(\omega)|^2$$

$$= \frac{cn}{8\pi} |\vec{\mathcal{E}}_{LO}|^2 + \frac{cn}{8\pi} |\vec{\mathcal{E}}_R|^2 + \frac{cn}{4\pi} \mathrm{Re}[\vec{\mathcal{E}}^*_{LO} \cdot \vec{\mathcal{E}}_R]$$

$$= I_{LO} + I_R + I_H \tag{12}$$

where $I_H \equiv \frac{cn}{4\pi} \mathrm{Re}[\vec{\mathcal{E}}^*_{LO} \cdot \vec{\mathcal{E}}_R]$ is the heterodyned intensity, I_{LO} (I_R) is the intensity at the detector if only $\vec{\mathcal{E}}_{LO}$ ($\vec{\mathcal{E}}_R$) is present, and n is the index of refraction at ω. Of particular interest in spectroscopy is the lineshape of the output signal which depends strongly on the relative strengths of the three terms I_{LO}, I_R, and I_H. We examine two extreme cases — $I_R \gg I_{LO}$ and $I_R \ll I_{LO}$.

If $|\vec{\mathcal{E}}_R| \gg |\vec{\mathcal{E}}_{LO}|$, the output signal shows a resonance proportional to the square magnitude of the resonant susceptibility, and so the strength of this resonance will increase quadratically with N, the density of resonant scatterers. The lineshape, in this case, is complicated by the presence of the local oscillator and may show a relative minimum anywhere within the spectrum due to the interference effects of the heterodyne term, I_H. Unlike I_{LO} and I_R which represent the actual intensities of the separate fields, the heterodyne intensity, I_H, is not a true intensity and can take on either positive or negative values. Furthermore, when several closely-spaced resonances are involved, the lineshape is determined by $|\vec{\mathcal{E}}_{LO} + \sum_i (\vec{\mathcal{E}}_R)_i|^2$ with the sum over all resonances. Cross-terms between different resonant fields severely distort

the spectrum, limiting its usefulness for spectroscopy.

At the other extreme, for a weak resonance with $I_{LO} \gg I_R$, the dispersive signal is carried on the heterodyne term, I_H (assuming the component of $\vec{\mathcal{E}}_{LO}$ along $\vec{\mathcal{E}}_R$ is much larger than $|\vec{\mathcal{E}}_R|$). The output signal now consists of the large nondispersive off-set due to the strong local oscillator upon which is superimposed the lineshape of a linear combination of the real and imaginary parts of the resonant susceptibility from I_H. The resonant signal will decrease linearly with N instead of quadratically, thus the sensitivity falls off in the same way as in linear scattering experiments. When several resonances are present, the signal term becomes $\frac{cn}{4\pi} \sum_i \mathrm{Re}[\vec{\mathcal{E}}^*_{LO} \cdot (\vec{\mathcal{E}}_R)_i]$, so all contributions are linearly superimposed. In such a spectrum, it is relatively easy to separate the individual resonances.

When dealing with the ultimate detection sensitivity of these nonlinear techniques, this weak resonance limit is of interest. In particular the modulation depth of the signal is important, as defined by

$$M_{AMP} \equiv \frac{I_H}{I_{LO}} = \frac{2\mathrm{Re}[\hat{e}^*_{LO} \cdot \vec{\mathcal{E}}_R]}{|\vec{\mathcal{E}}_{LO}|} \tag{13}$$

where we let $\vec{\mathcal{E}}_{LO} = |\vec{\mathcal{E}}_{LO}|\hat{e}_{LO}$. The condition of a weak resonance ensures that $M_{AMP} \ll 1$. This ratio of dispersive signal to nondispersive signal will be useful in determining the detection limit as described in part E of this section.

2. Polarization Analysis - Nulled Local Oscillator

This technique of analysis requires the addition of a general polarization analyzer in the detection system,[10,11] consisting of a quar-

ter-wave plate followed by a linear analyzer. Adjusting the axes of these two optical elements any pure elliptical polarization state can be analyzed. Figure 2 shows the orientation of the axes to transmit the polarization state $\hat{e}_\alpha$ as defined in Eq. (10).

With the introduction of a polarization analyzer before the detector we reduce the output field reaching the detector to

$$\vec{\mathcal{E}}_D = (\hat{e}_\alpha^* \cdot \vec{\mathcal{E}}(\omega))\hat{e}_\alpha$$

$$= (\hat{e}_\alpha^* \cdot \vec{\mathcal{E}}_{LO} + \hat{e}_\alpha^* \cdot \vec{\mathcal{E}}_R)\hat{e}_\alpha . \tag{14}$$

A particularly interesting situation occurs when the analyzer exactly nulls the contribution to $\vec{\mathcal{E}}_D$ from the local oscillator. This is the case when $\hat{e}_\alpha^* \cdot \hat{e}_{LO} = 0$. The intensity at the detector becomes

$$I_D(\omega) = \frac{cn}{8\pi} |\hat{e}_\alpha^* \cdot \vec{\mathcal{E}}_R|^2 . \tag{15}$$

Only the component of the resonant field which is orthogonal to the local oscillator contributes to the signal. There is no nondispersive contribution to the signal — the spectrum shows only resonances.

The result given in Eq. (15) is independent of the relative strength of $\vec{\mathcal{E}}_R$ and $\vec{\mathcal{E}}_{LO}$, but does depend on the square magnitude of the resonant susceptibility. Unlike the amplitude analysis case discussed above, with the local oscillator rejected the detected signal is always quadratic in the density N. Thus, although the constant background has been removed, the small signal from a weak resonance may be obscured by various noise sources, leading to reduced sensitivity (see section IIE

for the signal to noise analysis).

We note that the detected intensity depends on $\hat{e}_\alpha^* \cdot \vec{\mathcal{E}}_R$, where $\hat{e}_\alpha$ is orthogonal to the local oscillator field. For a given resonant and nonresonant susceptibilities and input field strengths, the magnitude of $\hat{e}_\alpha^* \cdot \vec{\mathcal{E}}_R$ depends only on the choice of the polarization states of the input fields. Varying the input polarizations alters the direction of $\vec{\mathcal{E}}_R$ and $\vec{\mathcal{E}}_{LO}$ (and thus $\hat{e}_\alpha$), while the magnitude of $\vec{\mathcal{E}}_R$ (and the nonlinear portion of $\vec{\mathcal{E}}_{LO}$) also changes. Thus the detected intensity in Eq. (15) can be optimized by the proper choice of input polarization states. This type of optimization applies to all forms of analysis discussed in this section, with specific examples given in subsection D.

So far we have dealt only with the nulling of the nondispersive local oscillator, but this nulling technique can also be extended to include cancellation of contributions from particular resonances. Consider, for example, two resonances separated in frequency by several linewidths — one resonance greatly dominating the other. The total output field is

$$\vec{\mathcal{E}}(\omega) = \vec{\mathcal{E}}_{LO}(\omega) + \vec{\mathcal{E}}_{R1}(\omega) + \vec{\mathcal{E}}_{R2}(\omega)$$

with $\vec{\mathcal{E}}_{R1}$ ($\vec{\mathcal{E}}_{R2}$) due to the strong (weak) resonance. In a limited spectral range around the central frequency of the weak resonance, the field $\vec{\mathcal{E}}_{R1}(\omega)$ will change only slightly in magnitude and phase. Thus the polarization analyzer may be adjusted to nearly null the local oscillator and the strong resonance fields in this spectral region. In this case the output signal shows essentially only the component of $\vec{\mathcal{E}}_{R2}$ orthogonal to $(\vec{\mathcal{E}}_{LO} + \vec{\mathcal{E}}_{R1})$. This generalization may be useful to study previously

undetectable resonances.

3. Polarization Analysis - Heterodyned Local Oscillator

Another form of polarization analysis, the heterodyned local oscillator technique,[10,11] combines the attractive features of the two previously described methods. In this case, the polarization analyzer is rotated away from the position of nulled local oscillator discussed above, allowing a small fraction of this field to be transmitted. The strength of this leakage local oscillator field can be adjusted such that it is dominant over the resonant field while still being much weaker than the full local oscillator field. Thus, as in the nulled local oscillator case, the spectrum shows quite strongly the dispersive signal, while this signal now comes from the heterodyning of the leakage local oscillator and resonant fields and is linear in χ_R, as in the amplitude analysis case. This polarization technique allows one to scale the strength (and to alter the phase) of the local oscillator so that the modulation depth of the resonant signal is fixed above the possible noise fluctuations of the leakage local oscillator.

To formalize this discussion, we assume the polarization analyzer now transmits the polarization state $\hat{e}_{\alpha'}$ which is close to the state $\hat{e}_{\alpha}$ which exactly nulls the local oscillator field. We define a generalized complex small angle Θ between the polarization state $\hat{e}_{\alpha'}$ and the local oscillator unit vector $\hat{e}_{LO}$.

$$\hat{e}^{*}_{\alpha'} \cdot \hat{e}_{LO} = \Theta \ . \tag{16}$$

The quantity Θ then describes the amount of local oscillator to be al-

lowed to leak through the analyzer. The output field at the detector from Eq. (14) becomes

$$\vec{\mathcal{E}}_D(\omega) = [(\hat{e}^*_{\alpha'} \cdot \hat{e}_{LO})|\vec{\mathcal{E}}_{LO}| + \hat{e}^*_{\alpha'} \cdot \vec{\mathcal{E}}_R]\hat{e}_{\alpha'}$$

$$= [\Theta\,|\vec{\mathcal{E}}_{LO}| + \hat{e}^*_{\alpha} \cdot \vec{\mathcal{E}}_R]\hat{e}_{\alpha'} \tag{17}$$

where we have assumed that $|\Theta| \ll 1$ so that $\hat{e}^*_{\alpha'} \cdot \vec{\mathcal{E}}_R = \hat{e}^*_{\alpha} \cdot \vec{\mathcal{E}}_R$, and the detected intensity is

$$I_D(\omega) = \frac{cn}{8\pi}\left|\Theta\,|\vec{\mathcal{E}}_{LO}| + \hat{e}^*_{\alpha} \cdot \vec{\mathcal{E}}_R\right|^2$$

$$= |\Theta|^2\, I_{LO} + I'_R + I'_H \tag{18}$$

where I_{LO} is the intensity at the detector due to the full local oscillator, I'_R is the resonant intensity at the detector as in the nulled local oscillator case, and

$$I'_H = \frac{cn}{4\pi}\,\mathrm{Re}[(\Theta^*|\vec{\mathcal{E}}_{LO}|)(\hat{e}^*_{\alpha} \cdot \vec{\mathcal{E}}_R)]$$

$$= \frac{cn}{4\pi}|\vec{\mathcal{E}}_{LO}|\,\mathrm{Re}[\Theta^*(\hat{e}^*_{\alpha} \cdot \vec{\mathcal{E}}_R)]. \tag{19}$$

Neglecting the term I'_R in the case of a weak resonance, Eq. (18) shows explicity the reduced local oscillator intensity and the heterodyned signal term. From Eq. (19) the complex nature of Θ can be exploited to examine both the real and imaginary parts of $\hat{e}^*_{\alpha} \cdot \vec{\mathcal{E}}_R$.

An informative expression for Θ can be derived when the state $\hat{e}_{\alpha'}$

is obtained from $\hat{e}_\alpha$ by infinitesimal changes in the characteristic angles θ and ϕ of $\hat{e}_\alpha$. We have

$$\hat{e}_{\alpha'} \simeq \hat{e}_\alpha + \frac{\partial \hat{e}_\alpha}{\partial \theta} d\theta + \frac{\partial \hat{e}_\alpha}{\partial \phi} d\phi$$

$$= \hat{e}_\alpha + \hat{e}^*_\beta \, d\theta - i \, \hat{e}_\beta \, d\phi$$

with $\hat{e}_\beta$ orthogonal to $\hat{e}_\alpha$. So,

$$\Theta \equiv \hat{e}^*_{\alpha'} \cdot \hat{e}_{LO}$$

$$= (\cos 2\phi \; d\theta - i \; d\phi)(\hat{e}^*_\beta \cdot \hat{e}_{LO}) \tag{20}$$

where there is an overall phase factor $\hat{e}^*_\beta \cdot \hat{e}_{LO}$ of the local oscillator state relative to polarization state $\hat{e}_\beta$, $d\theta$ is the change in the inclination angle of the axis and $d\phi$ is the change in the eccentricity angle of the elliptical polarization state. Relating these angles to the inclination angles of the quarter-wave plate, η, and the linear analyzer, ζ, as in Fig. 2, we have

$$\Theta = [- i \; d\zeta + (\cos 2(\zeta - \eta) + i) d\eta](\hat{e}^*_\beta \cdot \hat{e}_{LO}). \tag{21}$$

Simple cases occur when $d\eta = 0$, i.e., heterodyning by only uncrossing the linear analyzer ($\Theta = -i d\zeta(\hat{e}^*_\beta \cdot \hat{e}_{LO})$ and when $d\eta = d\zeta$, i.e., uncrossing both quarter-wave plate and linear analyzer by the same amount ($\Theta = \cos 2(\zeta - \eta) d\zeta(\hat{e}^*_\beta \cdot \hat{e}_{LO})$). Thus by proper choice of $d\eta$ and $d\zeta$ the phase of Θ can assume any value and can be adjusted to display only the real

or the imaginary part of the susceptibility. This added flexibility over the standard amplitude analysis technique makes this heterodyned local oscillator method more useful to sort out complicated spectra. Again, to determine the sensitivity and to compare this case with the amplitude case, we define the modulation depth as

$$M_{HET} \equiv \frac{I'_H}{|\Theta|^2 \, I_{LO}} = \frac{2\mathrm{Re}[\Theta^*(\hat{e}_\alpha^* \cdot \vec{\mathcal{E}}_R)]}{|\Theta|^2 \, |\vec{\mathcal{E}}_{LO}|} \, . \tag{22}$$

A crude comparison of this expression with Eq. (13) shows that the heterodyne case improves the modulation by a factor of about $|\Theta|^{-1}$. Since typically $|\Theta| \sim 10^{-2} - 10^{-3}$, there will be two or three orders of magnitude improvement in the detection sensitivity when using this polarization analysis technique. This is born out in the more detailed signal to noise calculation of section IIE.

4. Polarization Analysis - Coherent Nonlinear Ellipsometry

An alternate form of spectroscopy, coherent ellipsometry,[12] examines explicitly the dispersion of the output field's polarization state. This can be done by measuring the angles (θ,ϕ) describing the elliptical polarization as a function of the characteristic frequency parameter. As in normal ellipsometry, these angles are determined by varying both the quarter-wave plate and the linear analyzer to obtain a null of the nonlinear signal. In principle, one can then relate this dispersion of the polarization state to the dispersion of the resonant susceptibility.

To begin this discussion, we introduce two angles (θ',ϕ') which are easily determined from the components of the output field $\vec{\mathcal{E}}(\omega)$. The components are taken with respect to the orthogonal polarization

states $\hat{e}_\alpha$ and $\hat{e}_\beta$, with $\hat{e}_\alpha$ orthogonal to the local oscillator as before.

$$\vec{\mathcal{E}} = (\hat{e}_\alpha^* \cdot \vec{\mathcal{E}}_R)\hat{e}_\alpha + (\hat{e}_\beta^* \cdot \vec{\mathcal{E}}_{LO} + \hat{e}_\beta^* \cdot \vec{\mathcal{E}}_R)\hat{e}_\beta = \mathcal{E}_\alpha \hat{e}_\alpha + \mathcal{E}_\beta \hat{e}_\beta .$$

The angles θ' and ϕ' are given by the relations

$$\tan 2\theta' = \frac{2\mathrm{Re}[\mathcal{E}_\alpha^* \mathcal{E}_\beta]}{|\mathcal{E}_\alpha|^2 - |\mathcal{E}_\beta|^2}$$

$$\sin 2\phi' = \frac{2\mathrm{Im}[\mathcal{E}_\alpha^* \mathcal{E}_\beta]}{|\mathcal{E}_\alpha|^2 + |\mathcal{E}_\beta|^2} . \tag{23}$$

The definition of these angles is a generalization of the inclination and eccentricity angles which are defined with the same relations as Eq. (23) but with respect to the linear polarization states $\hat{e}_x$ and $\hat{e}_y$. By using the "natural" polarization states of the problem, the interpretation of the dispersion is clearer. For example, when the resonance is weak, we have $|\mathcal{E}_\alpha| \ll |\mathcal{E}_\beta| \simeq |\hat{e}_\beta^* \cdot \vec{\mathcal{E}}_{LO}|$ and

$$\tan 2\theta' \simeq 2\theta' \simeq -\frac{2\mathrm{Re}[(\hat{e}_\alpha^* \cdot \vec{\mathcal{E}}_R)^*(\hat{e}_\beta^* \cdot \vec{\mathcal{E}}_{LO})]}{|\hat{e}_\beta^* \cdot \vec{\mathcal{E}}_{LO}|^2}$$

$$\sin 2\phi' \simeq 2\phi' \simeq \frac{2\mathrm{Im}[(\hat{e}_\alpha^* \cdot \vec{\mathcal{E}}_R)^*(\hat{e}_\beta^* \cdot \vec{\mathcal{E}}_{LO})]}{|\hat{e}_\beta^* \cdot \vec{\mathcal{E}}_{LO}|^2} , \tag{24}$$

thus θ' is dispersive as the real part of an effective resonant field while ϕ' shows the dispersion of the imaginary part of this field. These angles are both linear in the resonant susceptibility with all the advantages this entails.

Of course, in any experiment the angles θ and ϕ describing the polarization state are measured, but θ' and ϕ' can be deduced from the re-

lations

$$\tan 2\theta' = \frac{\sin 2\theta \cos 2\phi}{\sin 2\phi_\alpha \sin 2\phi + \cos 2\phi_\alpha \cos 2\phi \cos 2\theta}$$

$$\sin 2\phi' = \cos 2\phi_\alpha \sin 2\phi - \sin 2\phi_\alpha \cos 2\phi \cos 2\theta. \tag{25}$$

These relations are derived using Eq. (23) with $\mathcal{E}_\alpha$ and $\mathcal{E}_\beta$ written in terms of x,y coordinates. In Eq. (25), we have assumed that the state $\hat{e}_\alpha$ is described by an inclination angle θ_α chosen to be zero, and an eccentricity angle equal to ϕ_α.

Although coherent nonlinear ellipsometry involves actual determination of elliptical polarization angles θ and ϕ, it is closely related to the previously described polarization analysis techniques. In the nulled and heterodyned local oscillator techniques the analyzer is fixed at one polarization state as the frequency is scanned through the resonance, while in ellipsometry the analyzer and frequency are simultaneously adjusted. Th latter requires a point by point spectrum be taken, incrementing the frequency, then searching for the null. It is often easier to make a polarization-sensitive spectrum of intensity through a fixed analyzer versus frequency, as in the previously described techniques. Basically, the simplicity of the nulled or heterodyned local oscillator technique occurs because information is being determined about either $\mathrm{Re}(\chi_R)$, $\mathrm{Im}(\chi_R)$, or $|\chi_R|^2$, whereas the ellipsometry technique determines both $\mathrm{Re}(\chi_R)$ and $\mathrm{Im}(\chi_R)$ in the course of one spectral scan.

Since an ellipsometry experiment searches only for a null, in principle it does not depend at all on the input beams absolute power or the

fluctuations in the power. This, together with the simple dependence on the resonant susceptibility, makes coherent ellipsometry a useful alternate form of nonlinear spectroscopy.

D. Stimulated Raman Processes vs. Signal Generation Processes and Specific Examples

In the previous discussions of the theory of four-wave mixing and the various analysis techniques, the general frequency mixing case is used throughout. We now want to consider the further classification of these nonlinear techniques by the particular type of frequency mixing that is involved. (This approach can be contrasted to that of Owyoung[13] in which the frequency classification has primary importance.) A distinction is made between stimulated Raman processes with the output ω and $\vec{k}$ degenerate with one of the input beams, although the polarization may be different, and signal generation processes with ω being at a frequency not identical to the three pump frequencies. We consider briefly the general characteristics of these two types of processes, then more specific examples are detailed. Emphasis is placed on signal generation processes, which are demonstrated in the experimental section (section III).

1. Stimulated Raman Scattering (SRS) Processes

In the SRS processes we have

$$\omega_c = \omega \qquad \text{and} \qquad \vec{k}_c = \vec{k}, \tag{26}$$

thus the input field at ω_c also serves as the linear local oscillator

field, $\vec{\mathcal{E}}(0,\omega)$. The nonlinear signal appears as a change in magnitude and/or polarization of this beam as it passes through the nonlinear mixing region. For energy conservation and phase matching, we require that

$$\omega_b = -\omega_a \quad \text{and} \quad \vec{k}_b = -\vec{k}_a ,$$

which is simply satisfied by the presence of a single input beam, called the "pump" beam. In this case, phasematching is automatic, i.e., requires no special geometry. Another advantage of this type of process is that it is easily analyzed since one monitors induced changes in the "probe" beam at ω_c. Typically, the probe beam is intense enough that detection can be done using high quantum efficiency photodiodes. A serious difficulty with this SRS-type process is the need for a stable intensity probe beam when doing amplitude analysis, for the full intensity of the probe beam strikes the detector. In practical cases the detection sensitivity in amplitude analysis will be limited by the intensity fluctuations in the probe laser. A second problem arises with the polarization analysis techniques — linearly scattered light of the probe beam also strikes the detector. This problem can be minimized but it cannot be prevented, for there is no possibility of frequency discrimination against this noise source. Thus, there are some disadvantages to using the SRS processes as forms of nonlinear spectroscopy.

Most experimental work which has been done using the SRS process has involved studies of Raman-type two-photon resonances. As each analysis technique has been established, it has been given a new name. For example, the SRS form of amplitude analysis has been highly developed by Owyourg[9,13] and has the acronym SRGS, for Stimulated Raman Gain Spec-

troscopy. The polarization analysis counterparts have been studied predominantly by Levenson[10,14] under the acronyms RIKES (Raman Induced Kerr Effect Spectroscopy) and OHD-RIKES (Optical Heterodyned Detection-RIKES). A brief description of typical experimental arrangements used in these forms of nonlinear spectroscopy is included below.

As mentioned above, in SRGS the most serious problem is the stability of the probe laser, thus it is very desirable to use a CW laser rather than a pulsed laser. It is found that the amplitude noise spectrum of a CW laser using a commercial noise suppression system is greatly reduced if one examines only the higher frequency components. This is accomplished by modulating the pump beam (another CW laser) at 25kHz and using lock-in detection for signal collection (see Fig. 3). Since CW lasers are used for both pump and probe, very high resolution spectra (10^{-4} cm^{-1}) are obtainable. However, due to the low power level of the CW pump the gain coefficient, G, is quite small ($G \sim 10^{-5}$ have been observed with the setup). This technique is used predominantly with linear input polarizations in gaseous, and therefore isotropic, media. In this case, Eq. (17) becomes

$$I_D(\omega) = I(\omega)\left\{1 - \frac{16\pi\beta}{cn} \mathrm{Im}[\hat{e}_c^* \cdot \overleftrightarrow{\chi}_R \vdots \hat{e}_a \hat{e}_a^* \hat{e}_c] I(\omega_a)\right\}$$

$$= I(\omega)\{1 + G\} \tag{27}$$

where $I(\omega)$ is the intensity at the probe frequency, $I(\omega_a)$ is the intensity at the pump frequency, $\hat{e}_c$ and $\hat{e}_a$ describe the polarization states of the probe and pump fields, respectively. If all fields are along the x-direction, SRGS examines the tensor element $[\chi_R(\omega = \omega_a - \omega_a + \omega_c)]_{1111}$

describing polarized scattering. With the pump beam along $\hat{x}$ and the probe along $\hat{y}$, $[\chi_R(\omega = \omega_a - \omega_a + \omega_c)]_{1221}$, related unpolarized scattering, is studied.

The polarization forms of stimulated Raman scattering, RIKES and OHD-RIKES, involve slightly different setups as shown in Fig. 4 (also see Ref. 15). The rejection of nearly all the probe (local oscillator) field makes these techniques much less sensitive to probe laser stability, so experiments can be done with either CW or pulsed probe lasers and pulsed pump lasers. The common setup uses a CW-probe laser at a fixed frequency and a tunable, high power, pulsed dye laser as the pump laser. The probe beam may be chopped to prevent sample heating. Gated detection examines the signal only during the pulsewidth of the pump laser.

In the nulled local oscillator technique, RIKES, we have from Eq. (15)

$$I_D(\omega) = \left(\frac{8\pi}{cn}\right)^2 \rho^2 |\hat{e}_\alpha^* \cdot \overleftrightarrow{\chi}_R(\omega = \omega_a - \omega_a + \omega_c) : \hat{e}_a \hat{e}_a^* \hat{e}_c|^2 I^2(\omega_a) I(\omega_c) \quad (28)$$

where $\hat{e}_\alpha$ is defined such that $\hat{e}_\alpha^* \cdot \hat{e}_c = 0$. The standard RIKES setup has $\hat{e}_c = \hat{x}$ and $\hat{e}_a = \frac{1}{\sqrt{2}}(\hat{x} + \hat{y})$, so the effective susceptibility is $\frac{1}{2}\{[\chi_R(\omega_c = \omega_a - \omega_a + \omega_c)]_{1122} + [\chi_R(\omega_c = \omega_a - \omega_a + \omega_c)]_{1212}\}$ for an isotropic medium. To date, a slight variation of this experiment has been performed — for convenience, only the linear part of the local oscillator is nulled, i.e., the probe beam is nulled when the pump beam is not present. In this case the nonresonant susceptibility must be included with the resonant susceptibility above.

If the polarization analyzer is now adjusted such that $d\zeta = d\eta = \theta_o$, we have one possible heterodyned form of RIKES. For the same input

fields considered above, the OHD-RIKES intensity at the detector (Eq. (18)) becomes

$$I_D(\omega) \approx I(\omega_c)\left\{\theta_o^2 - \frac{16\pi\beta}{cn}\,\theta_o \mathrm{Im}\,\tilde{\beta}_2\{[\chi_R]_{1122} + [\chi_R]_{1212}\}\right]I(\omega_a)\right\} \qquad (29)$$

where the frequency dependence of the susceptibility has been suppressed. Comparing this to the SRGS expression, there is the expected reduction of the local oscillator and the improved signal modulation depth. One distinction in this case is that SRGS examines either $[\chi_R]_{1111}$ or $[\chi_R]_{1221}$ while this case of OHD-RIKES involves $[\chi_R]_{1122} + [\chi_R]_{1212} = [\chi_R]_{1111} - [\chi_R]_{1221}$ (the last equality being true in isotropic media although not necessarily true for other material symmetries[16]). Therefore, OHD-RIKES measures the difference between the polarized and unpolarized scattering while SRGS measures each separately. Further discussion of these SRS processes can be found in the two recent review articles.[10,13]

2. Signal Generation Processes

The second frequency mixing case considered here is the class of processes known as signal generation processes.[17] In this case, the output frequency and wavevector are not identical to any of the three input pump fields. Furthermore, it is generally true that there is no linear term in the expression for the local oscillator field. The principal advantage of the signal generation process is that the output is at an independent frequency, therefore frequency dispersive elements can be used to totally isolate the output signal from the pump frequencies. No linear background light from the input lasers should reach the detector.

In dispersive media, there is the added advantage that the output wavevector is spatially separated from the others, due to the phasematching condition. In signal generation processes (without a linear local oscillator) there are also much less restrictive requirements on laser stability. In fact, we shall see below that the presence of the nonlinear local oscillator can be used to provide a nonlinear reference signal for normalization against laser fluctuations.

On the other hand, the nonlinear nature of the output means that the signal is weak, requiring photomultipliers as detectors with their relatively low quantum efficiency and high shot noise. Another disadvantage is the lack of automatic phasematching. This has several ramifications: (1) the linear dispersion of the medium must be known well enough to achieve phasematching, (2) once achieved, the phasematching must be maintained over the desired spectral range,[18] and (3) the usual finite crossing angles of the input beams limit the interaction length and so limit the strength of the output signal. (In some studies requiring high spatial resolution within the medium, the latter point is considered an advantage.[19]) Often in signal generation experiments a double monochromator is needed to separate the signal from the pump lasers. It is then necessary to ensure that the monochromator is scanned synchronously with the changing output frequency. Even with these disadvantages, signal generation processes have become a popular form of nonlinear spectroscopy.

As with the SRS processes, Raman resonances have received the most attention for study by signal generation processes. In these experiments, the frequency difference, $\omega_a - \omega_c$, of two of the input beams is scanned near the Raman resonance frequency, ω_R. The most straightfor-

ward experiments, involving only two input frequencies, $\omega_b = \omega_a$ or $\omega_b = \omega_c$, mix one of the two input frequencies with this difference frequency. The resulting output frequency is at either

$$\text{(a)} \quad \omega = \omega_a + (\omega_a - \omega_c) = 2\omega_a - \omega_c \simeq \omega_a + \omega_R$$

or

$$\text{(b)} \quad \omega = \omega_c - (\omega_a - \omega_c) = 2\omega_c - \omega_a \simeq \omega_c - \omega_R.$$

In the first case, the output is upshifted to approximately the anti-Stokes frequency from ω_a, while the second case downshifts the output to the Stokes side of ω_c. The mixing process expressed in (a) has been dubbed: CARS for Coherent Anti-Stokes Raman Spectroscopy.[20] By analogy the second case is called CSRS (pronounced scissors) or Coherent Stokes Raman Spectroscopy.

Next we consider the possible ways to analyze the output from these signal generation processes. With only two exceptions, the only analysis technique previously used is the amplitude scheme described in the first part of section IIC. The two exceptions are the recent work of Akhmanov, et al.[12] on coherent Raman ellipsometry and Song, et al.[21] on a specialized form of nulled local oscillator detection (background suppression) involving the use of three independent input frequencies. This thesis contains a complete discussion of the polarization analysis techniques as they are applied to the signal generation case, and section III presents experimental work deomonstrating the usefulness of polarization-sensitive detection in a CARS experiment.

Before the new techniques of polarization analysis are described, we review the standard form of CARS (for example) in which only the amplitude of the nonlinear signal is measured. Figure 5 shows the normal CARS setup in which two input lasers are used, with $\omega_b = \omega_a$ and $\vec{k}_b = \vec{k}_a$. The output signal is linear in the intensity $I(\omega_c)$ and quadratic in $I(\omega_a)$, thus pulsed lasers are often used. The angle between the two input beams is adjusted to achieve phasematching $\vec{k} = 2\vec{k}_a - \vec{k}_c$, and the double monochromator is set to transmit the output frequency, $\omega = 2\omega_a - \omega_c$. As one of the input frequencies is scanned (usually ω_c), the output signal will show enhancement from the resonant susceptibility. The detected intensity is given by Eq. (12)

$$I_D(\omega) = \frac{cn}{8\pi}\beta^2 |\overleftrightarrow{\chi}_{NR}(-\omega,\omega_a,\omega_a,-\omega_c):\vec{\mathcal{E}}(\omega_a)\vec{\mathcal{E}}(\omega_a)\vec{\mathcal{E}}^*(\omega_c)$$

$$+ \overleftrightarrow{\chi}_R(-\omega,\omega_a,\omega_a,-\omega_c):\vec{\mathcal{E}}(\omega_a)\vec{\mathcal{E}}(\omega_a)\vec{\mathcal{E}}^*(\omega_c)|^2$$

$$= \left(\frac{8\pi}{cn}\right)^2\beta^2|[\chi_{NR}]_{1111} + [\chi_R]_{1111}|^2 I^2(\omega_a)I(\omega_c). \qquad (30)$$

The latter expression applies to the case of linear input polarizations parallel to the x-axis in an isotropic medium, a typical experimental situation. The interference effects between resonant and nonresonant susceptibilities are clearly shown in this expression. For this example the modulation depth of the resonant signal is simply

$$M_{AMP-CARS} = \frac{2Re([\chi_R]_{1111})}{[\chi_{NR}]_{1111}}$$

where we have assumed that the nonresonant susceptibility is a pure

real quantity. In most experimental arrangements, the limiting value of $M_{AMP-CARS}$ will be determined by the fluctuations in the laser intensities, which cause variations in the strength of the relatively large nonresonant signal. We delay the formal signal to noise analysis until the new forms of polarization sensitive-CARS are described.

It is natural at this point to describe two new forms of four-wave mixing spectroscopy — Background Suppression-CARS (BS-CARS) and Optical Heterodyned Detection-CARS (OHD-CARS). Within the framework established in section IIC, these two techniques follow logically as specific forms of polarization-sensitive signal generation processes — direct analogues of the SRS techniques RIKES and OHD-RIKES. In fact, we can now establish the hierarchy of four-wave mixing Raman techniques as shown in Fig. 6. Each acronym thus has its own place within this general structure. Of course, this framework applies equally well to the lesser studied two-photon absorption resonances, only the catchy acronyms have yet to be invented.

For completeness, however, let us describe these new techniques and indicate explicit expressions for the output intensity at the detector and modifications in the experimental apparatus of Fig. 5. In the case of background suppression (nulled local oscillator), the polarization analyzer is adjusted to null the output signal with the frequency far from resonance. As one scans through the resonance the detected intensity as given by Eq. (15) is

$$I_D(\omega) = \left(\frac{8\pi}{cn}\right)^2 \beta^2 |\hat{e}_\alpha^* \cdot \overleftrightarrow{\chi}_R(\omega = \omega_a + \omega_a - \omega_c) : \hat{e}_a \hat{e}_a \hat{e}_c^*|^2 I^2(\omega_a) I(\omega_c)$$

where $\hat{e}_\alpha$ is orthogonal to the polarization state of $\overleftrightarrow{\chi}_{NR}(\omega = \omega_a + \omega_a -$

ω_c)$\vdots\hat{e}_a\hat{e}_a\hat{e}_c^*$. As a concrete example, we return to the case of linear input polarizations and an isotropic medium. We choose the ω_a beam to be polarized along the $\hat{x}$-axis and the ω_c beam to be polarized at angle δ to the ω_a beam.

$$\hat{e}_a = \hat{x} \qquad \hat{e}_c = \cos\delta\ \hat{x} + \sin\delta\ \hat{y}$$

so that the effective nonresonant and resonant susceptibilities are

$$\overleftrightarrow{\chi}_{NR}\vdots\hat{e}_a\hat{e}_a\hat{e}_c^* = [\chi_{NR}]_{1111}\cos\delta\ \hat{x} + [\chi_{NR}]_{1221}\sin\delta\ \hat{y}$$

$$\overleftrightarrow{\chi}_{R}\vdots\hat{e}_a\hat{e}_a\hat{e}_c^* = [\chi_{R}]_{1111}\cos\delta\ \hat{x} + [\chi_{R}]_{1221}\sin\delta\ \hat{y}$$

and

$$\hat{e}_\alpha = \frac{-[\chi_{NR}]_{1221}\sin\delta\ \hat{x} + [\chi_{NR}]_{1111}\cos\delta\ \hat{y}}{\left[[\chi_{NR}]_{1111}^2\cos^2\delta + [\chi_{NR}]_{1221}^2\sin^2\delta\right]^{\frac{1}{2}}} \tag{31}$$

where the frequency dependence of the susceptibilities are suppressed. The total output signal becomes

$$I_D(\omega) = \left(\frac{8\pi}{cn}\right)^2\beta^2\left|\frac{(\rho_R - \rho_{NR})\sin\delta\ \cos\delta}{(\cos^2\delta + \rho_{NR}^2\sin^2\delta)^{\frac{1}{2}}}\right|^2 |[\chi_R]_{1111}|^2 I^2(\omega_a) I(\omega_c) \tag{32}$$

where $\rho_{NR} \equiv [\chi_{NR}]_{1221}/[\chi_{NR}]_{1111}$ and $\rho_R \equiv [\chi_R]_{1221}/[\chi_R]_{1111}$. It can be shown[22] that ρ_R is the depolarization ratio for the Raman mode; ρ_{NR} is similarly defined. As mentioned in the general discussion, one can optimize the output signal by choosing the proper input polarization states. In the example, we are free to optimize $I_D(\omega)$ with respect to

the choice of δ. The signal is maximized when

$$\tan\delta = (\rho_{NR})^{-\frac{1}{2}}. \tag{33}$$

If the isotropic medium obeys the Kleinman symmetry,[23] we have $\rho_{NR} = 1/3$ and $\delta = 60°$. For a strongly polarized Raman mode, $\rho_R = 0$, we can evaluate Eq. (32),

$$I_D(\omega) = \left(\frac{8\pi}{cn}\right)^2 \beta^2 \left(\frac{1}{16}\right) |[\chi_R]_{1111}|^2 I^2(\omega_a) I(\omega_c). \tag{34}$$

This can be compared to the signal one would have if there were no nonresonant term, i.e., this is in the limit of a strong Raman mode. In this case optimization occurs when all polarizations are parallel with the resulting idealized output

$$I_D^{IDEAL}(\omega) = \left(\frac{8\pi}{cn}\right)^2 \beta^2 |[\chi_R]_{1111}|^2 I^2(\omega_a) I(\omega_c).$$

We see that the use of polarization analysis has reduced the signal by a factor of 16 (compare with Eq. (34)). In most cases, this loss in signal can be either tolerated or overcome with increased input intensities. Clearly, it is possible to take a background free CARS spectrum without sacrificing too much signal, thus eliminating the lineshape distortions caused by the interference with the nonresonant term.

On the other hand, in the limit of a weak Raman mode, we should compare the intensity in Eq. (34) with the intensity of the total signal one would measure in an amplitude CARS experiment,

$$I_{AMP} \approx \left(\frac{8\pi}{cn}\right)^2 \beta^2 (\cos^2\delta + \rho_{NR}^2 \sin^2\delta)[\chi_{NR}]_{1111}^2 I^2(\omega_a) I(\omega_c)$$

$$= \left(\frac{8\pi}{cn}\right)^2 \beta^2 \left(\frac{1}{3}\right)[\chi_{NR}]_{1111}^2 I^2(\omega_a) I(\omega_c) \tag{35}$$

where δ and ρ_{NR} are evaluated at 60° and 1/3 as above. Forming the ratio of the signal transmitted through the analyzer (Eq.(34)) and the signal incident on the analyzer I_{AMP} (which will be essentially totally rejected), we have

$$I_D/I_{AMP} = \frac{3}{16}\left[\frac{[\chi_R]_{1111}}{[\chi_{NR}]_{1111}}\right]^2. \tag{36}$$

This expression shows two interesting features. First, the expected quadratic dependence on the ratio of resonant to nonresonant susceptibilities, which means the actual detected signal strength will become very weak for weak resonances. From this point of view, background suppression may not be the best technique to detect weak resonances. A second point to be made is the independence of this ratio on the laser powers. If, as part of a background suppression setup, the rejected signal from the analyzer is also monitored, we have a "built-in" normalization signal to eliminate fluctuations in the BS-CARS signal due to laser power fluctuations. A general experimental arrangement is indicated in Fig. 7.

Finally, let us compare this form of background suppression with that proposed by Song, et al.[21] Figure 8 shows the polarization arrangement suggested in their Letter. The frequency difference $\omega_a - \omega_c$ drives the Raman mode. With this polarization arrangement the nonlinear local oscillator field is of the form

$$\vec{\mathcal{E}}_{LO}(\omega) = i\beta\{\tfrac{1}{2}([\chi_{NR}]_{1221} - [\chi_{NR}]_{1212})\hat{x} + \tfrac{1}{2}([\chi_{NR}]_{1122} - [\chi_{NR}]_{1111})\hat{y}\}\mathcal{E}(\omega_a)\mathcal{E}(\omega_b)$$

$$\times\ \mathcal{E}(\omega_c)$$

$$= i\beta\{-\frac{1}{3}\ [\chi_{NR}]_{1111}\hat{y}\}\mathcal{E}(\omega_a)\mathcal{E}(\omega_b)\mathcal{E}(\omega_c)$$

where $\omega = \omega_a + \omega_b - \omega_c$ in this "four-color" CARS experiment and where Kleinman's symmetry is assumed. The orientation of the analyzer along $\hat{x}$ is correct to suppress the nonresonant susceptibility contribution in this case. Hence, this is the first example of polarization analysis used for background suppression in a CARS experiment. Unfortunately, it requires the use of a third input frequency, not commonly available in most amplitude CARS setups. Furthermore, Song, et al. describe only minor variations in their technique to compensate for the fact the Kleinman's symmetry is not precisely obeyed and do not address the more general polarization situation. The technique described in this section only requires the two input lasers normally used in CARS and can be used with general input polarization states. As such, the method described here is far superior to the previous techniques.

The second form of polarization-sensitive detection in signal generation processes is OHD-CARS, in which the analyzer is uncrossed to allow heterodyning between the nonresonant and resonant parts of the signal. Applying the general form of Eqs. (18) and (19) with $\omega = \omega_a + \omega_a - \omega_c$ to the example used in the description of BS-CARS above, the detected intensity is

$$I_D(\omega) \simeq |\Theta|^2 I_{LO} + I'_H$$

with

$$I_{LO} = \left(\frac{8\pi}{cn}\right)^2 \beta^2 (\cos^2\delta + \rho_{NR}^2 \sin^2\delta)[\chi_{NR}]_{1111}^2 I^2(\omega_a) I(\omega_c)$$

$$I'_H = \left(\frac{8\pi}{cn}\right)^2 \beta^2 (\rho_R - \rho_{NR}) \sin\delta \cos\delta [\chi_{NR}]_{1111} 2\mathrm{Re}(i\Theta^* [\chi_R]_{1111}) I^2(\omega_a) I(\omega_c) \tag{37}$$

where Θ is the generalized uncrossing angle, as defined in Eq. (21). The heterodyned term in this case is proportional to the product of the nonresonant and the real part of a phased portion of the resonant susceptibility. A more explicit form for Θ is needed before the lineshape of this heterodyned term can be established. We have from Eq. (31)

$$\hat{e}_\beta \equiv (\cos\delta\ \hat{x} + \rho_{NR} \sin\delta\ \hat{y})/(\cos^2\delta + \rho_{NR}^2 \sin^2\delta)^{1/2}$$

and

$$\vec{\mathcal{E}}_{LO} = i\beta[\chi_{NR}]_{1111} \mathcal{E}^2(\omega_a) \mathcal{E}^*(\omega_c) \hat{e}_\beta = |\vec{\mathcal{E}}_{LO}|(i\hat{e}_\beta). \tag{38}$$

The angles of the quarter-wave plate and linear analyzer, η and ζ, respectively, which block the polarization state, can be found to be

$$\eta = \zeta = \tan^{-1}\left(-\frac{1}{\rho_{NR} \tan\delta}\right). \tag{39}$$

Therefore, the expression for Θ in Eq. (21) becomes

$$\Theta = (d\zeta - d\eta) + i\, d\eta \tag{40}$$

where $d\zeta$ is a small uncrossing of the linear analyzer alone and $d\eta$ is similarly defined for the quarter-wave plate. Combining this with Eq. (37) the heterodyned term becomes

$$I_H' = \left(\frac{8\pi}{cn}\right)^2 \beta^2 (\rho_R - \rho_{NR}) \sin\delta \cos\delta [\chi_{NR}]_{1111}{}^2 \{d\eta\, \mathrm{Re}([\chi_R]_{1111}) + (d\eta - d\zeta)$$

$$\times\, \mathrm{Im}([\chi_R]_{1111})\} I^2(\omega_a) I(\omega_c). \tag{41}$$

The simplest heterodyned spectra occur when either only the linear analyzer is uncrossed or when both quarter-wave plate and linear analyzer are uncrossed together by the same angle. In the first instance we have

$$d\eta = 0 \Rightarrow I_H' \propto \mathrm{Im}([\chi_R]_{1111}) \tag{42a}$$

and in the second case

$$d\eta = d\zeta \Rightarrow I_H' \propto \mathrm{Re}[(\chi_R)_{1111}]. \tag{42b}$$

Thus, under easily achievable circumstances, either the real or the imaginary part of the resonant susceptibility can be displayed superimposed on the leakage local oscillator signal. The modulation depth for heterodyned detection becomes

$$M_{OHD} \equiv |I_H'|/|\Theta|^2 I_{LO}$$

cont'd

$$= \frac{(\rho_R - \rho_{NR})\sin\delta\cos\delta}{\cos^2\delta + \rho_{NR}^2\sin^2\delta} \frac{2\mathrm{Im}([\chi_R]_{1111})}{\theta_o[\chi_{NR}]_{1111}} \tag{43}$$

where $d\eta = 0$ and $d\zeta = \theta_o$. The factor involving the polarization angle δ can be optimized by choosing $\tan\delta = (\rho_{NR})^{-1}$. For $\rho_{NR} = 1/3$ and $\rho_R = 0$, the expression for M_{OHD} becomes

$$M_{OHD} = \frac{\mathrm{Im}([\chi_R]_{1111})}{\theta_o[\chi_{NR}]_{1111}} . \tag{44}$$

Comparing this to the modulation depth in the amplitude case, and assuming the Raman line is an isolated Lorentzian, we have an increase in the modulation by a factor of θ_o^{-1} when using the OHD technique. (Since the value of θ_o is as yet arbitrary, this increase may become infinite as $\theta_o \to 0$, i.e., in the background suppression case.) To confirm that this improvement carries over to the detection sensitivity we now perform a signal to noise analysis for the various forms of CARS experiments. We shall also find that there is an optimum value for θ_o, as discussed below.

E. Signal to Noise Analysis

In the previous section, the signal terms for the various forms of CARS experiments are written out explicitly for the specific case of linear input polarizations in isotropic media. We now want to consider the possible noise sources which cause fluctuations in this signal level. Three major noise sources can be identified and characterized; these are (1) laser intensity fluctuations; (2) finite extinction ratio of polarization analyzer, and (3) shot noise. Other noise sources

briefly considered are dark current, electronic noise, and linear light scattering. After the signal to noise ratio is established, it is inverted to give the limiting value of detectivity as determined by the ratio of the resonant to nonresonant susceptibilities. Typical numbers are then used to compare the techniques.

Laser intensity fluctuations are almost always the leading source of noise, especially when pulsed lasers are used. To characterize these fluctuations, the fractional mean square fluctuation is defined as[14]

$$\varepsilon_i \equiv \left\{\left(\overline{I(\omega_i)}\right)^2 - \left(\overline{I(\omega_i)}\right)^2\right\} / \left(\overline{I(\omega_i)}\right)^2 \tag{45}$$

where the bar indicates averaging over many pulses. For pulsed laser systems this mean square fluctuation may range from 10^{-4} to 10^{-1}. The variation in the nonlinear signal can be calculated from

$$\left(\overline{\Delta I(\omega)}\right)^2 = \sum_i \left(\frac{\partial I(\omega)}{\partial I(\omega_i)}\right)^2 \varepsilon_i \left(\overline{I(\omega_i)}\right)^2 \tag{46}$$

where the sum is over all independent frequencies involved in the nonlinear mixing.

The finite extinction ratio of the polarization leads to a leakage even in the null case. This leakage will show the same intensity fluctuations as the output intensity, but it is an incoherent form of background. We define the extinction ratio in terms of an angle θ_e, such that the fractional leakage of the imperfect polarizer is equal to a perfect polarizer rotated by an equivalent angle θ_e. Common polarizers have extinction ratios between 10^{-4} - 10^{-6}, so $\theta_e \sim 10^{-2}$ - 10^{-3} (1 to 10 mrad uncrossing angle).

The ultimate detection limit will be determined by the quantized nature of the output photons and is termed the shot noise limit.[24] It is assumed that photons arrive at the detector in a random fashion, so that the mean square fluctuation in the number of photons equals the number of photons. The mean square current generated by a photodetector of quantum efficiency q, gain g, and area A is given by

$$\left(\overline{i^2_{shot}}\right) = \frac{2g^2e^2qAI(\omega)}{\hbar\omega}\,\Delta\nu \tag{47}$$

where e is the electronic charge, I is the optical intensity incident on the detector, $\hbar\omega$ is the energy of each photon, and $\Delta\nu$ is the bandwidth of the detection system. As the signal intensity becomes very small shot noise will begin to dominate the other noise sources.

Other noise sources (not considered in the following calculation) are the dark current, electronic noise, and linear light scattering. Dark current acts as an additional source of shot noise, but proper choice of photomultiplier and gated detection should minimize its contribution to the noise. Electronic noise (or thermal noise) is due to variations in the electrical signal introduced by the detection system itself, and should be made unimportant by the proper design of the electronics. Light striking the photomultiplier from other than the nonlinear source constitutes another form of noise which is eliminated by proper spatial and spectral filtering of the output beam.

1. Signal to Noise — Amplitude CARS

Of the total intensity reaching the detector in this case, the resonance is carried on the heterodyned term, I_H, as defined in Eq. (12).

The signal current generated by the photodetector due to I_H is

$$i_s = \left(\frac{geqA}{\hbar\omega}\right) I_H. \tag{48}$$

Next we evaluate the noise contributions. The predominant intensity at the detector comes from the nonlinear local oscillator term, $I_{LO} \propto I^2(\omega_a)I(\omega_c)$. Fluctuation in the intensities leads to a mean square fluctuation in the photocurrent of

$$\left(\overline{\Delta i^2_{fluct}}\right) = \left(\frac{geqA}{\hbar\omega}\right)^2 I^2_{LO}\{4\epsilon_a + \epsilon_c\} \tag{49}$$

and the mean square shot noise contribution will be

$$\left(\overline{i^2_{shot}}\right) = \frac{2g^2e^2qA}{\hbar\omega} I_{LO}\Delta\nu. \tag{50}$$

Thus, the signal to noise ratio is

$$(S/N)_{AMP.\ CARS} = \frac{i_s}{\left(\left(\overline{\Delta i^2_{fluct}}\right) + \left(\overline{i^2_{shot}}\right)\right)^{\frac{1}{2}}}$$

$$= \frac{I_H}{\left(I^2_{LO}(4\epsilon_a + \epsilon_c) + \left(\frac{2\hbar\omega\Delta\nu}{qA}\right) I_{LO}\right)^{\frac{1}{2}}}. \tag{51}$$

In the limit of large fluctuations, this becomes

$$(S/N)_{\substack{AMP.\ CARS \\ (fluctuation)}} \approx \frac{M_{AMP-CARS}}{(4\epsilon_a + \epsilon_c)^{\frac{1}{2}}} = \frac{2Re([\chi_R]_{1111})/[\chi_{NR}]_{1111})}{(4\epsilon_a + \epsilon_c)^{\frac{1}{2}}} \tag{52}$$

where $M_{AMP.\ CARS}$ is the modulation depth and $(4\epsilon_a + \epsilon_c)^{\frac{1}{2}}$ is the rms

fluctuation in the background signal. S/N = 1 when these quantities are equal.

The shot noise limit will be reached when the fluctuations satisfy $(4\varepsilon_a + \varepsilon_c) \lesssim I_Q/I_{LO}$ where $I_Q = \frac{2\hbar\omega\Delta\nu}{qA}$. If we assume $\hbar\omega \approx 3$eV, $\Delta\nu = 10^6$ Hz (1 μsec gate time), q = .1 so that $I_QA \sim 10^{-11}$W and that the nonresonant susceptibility of $\sim 10^{-14}$ esu and input powers of 1 kW lead to an output signal power of 10^{-6}W, we find $(4\varepsilon_a + \varepsilon_c)^{\frac{1}{2}} \lesssim 3 \times 10^{-3}$. Thus, about .1% rms fluctuation in each input laser power will bring the signal to noise ratio to the shot limit, which is given by

$$(S/N)_{\substack{\text{AMP. CARS}\\ \text{(shot)}}} \approx I_H/(I_QI_{LO})^{\frac{1}{2}}$$

$$= \left(\frac{8\pi}{cn}\right)\beta\ 2\mathrm{Re}([\chi_R]_{1111})\left(\frac{I^2(\omega_a)I(\omega_c)}{I_Q}\right)^{\frac{1}{2}}. \tag{53}$$

2. Signal to Noise - Background Suppression-CARS

In this case, the signal current is given by

$$i_s = \frac{geqA}{\hbar\omega} I_{BS} \tag{54}$$

where I_{BS} is the intensity $I_D(\omega)$ from Eq. (32). There is also a nonlinear incoherent source which strikes the photomultiplier — the polarization analyzer leakage intensity, I_L,

$$I_L = \theta_e^2\ I_{LO}. \tag{55}$$

For weak resonances, this leakage intensity dominates the signal intensity, and fluctuations in I_L are an additional source of noise. We have

$$(S/N)_{BS-CARS} \approx \frac{\left(\frac{geqA}{\hbar\omega}\right) I_{BS}}{\left[\left(\frac{geqA}{\hbar\omega}\right)^2 \theta_e^4 I_{LO}^2 (4\epsilon_a + \epsilon_c) + \frac{2g^2e^2qA}{\hbar\omega} \Delta\nu(\theta_e^2 I_{LO} + I_{BS})\right]^{\frac{1}{2}}}$$

$$\approx \frac{I_{BS}}{[(\theta_e^2 I_{LO})^2 (4\epsilon_a + \epsilon_c) + (\theta_e^2 I_{LO} + I_{BS}) I_Q]^{\frac{1}{2}}} \quad . \tag{56}$$

Considering again the two limits:

$$(S/N)_{\substack{BS-CARS \\ (fluctuation)}} \approx \frac{I_{BS}}{\theta_e^2 I_{LO} (4\epsilon_a + \epsilon_c)^{\frac{1}{2}}}$$

$$\approx \left(\frac{3}{16}\right) \frac{|[\chi_R]_{1111}|^2}{\theta_e^2 [\chi_{NR}]_{1111}^2 (4\epsilon_a + \epsilon_c)^{\frac{1}{2}}} \tag{57}$$

where we have used the same example to evaluate the ratio. One finds that $(S/N)_{BS-CARS}$ optimizes when $\tan\delta = (\rho_{NR})^{-1}$, while the signal alone maximizes for $\tan\delta = (\rho_{NR})^{-\frac{1}{2}}$. Upon evaluation, this results in only a 25% change in the signal to noise ratio and is ignored in the present calculation. In the shot noise limit, we have

$$(S/N)_{\substack{BS-CARS \\ (shot)}} \approx (I_{BS}/I_Q)^{\frac{1}{2}} \approx \left(\frac{8\pi}{cn}\right)\beta\ \tfrac{1}{4}|[\chi_R]_{1111}| \left(\frac{I^2(\omega_a) I(\omega_c)}{I_Q}\right)^{\frac{1}{2}} . \tag{58}$$

Comparing the shot noise limits for BS-CARS and AMP-CARS, assuming a Lorentzian lineshape so that the maximum value of $2\mathrm{Re}(\chi_R)$ equal the maximum value of $|\chi_R|$, we see that there is only a factor of four difference in the limits (AMP-CARS being more sensitive). Approximately half of this factor of four can be attributed to the difference in input polarizations used in the two setups, while the other factor of two is due to the use of the polarization analyzer which rejects approximately half

of the signal intensity.

3. Signal to Noise — Optical Heterodyned Detection-CARS

For OHD-CARS it is assumed that enough intensity is leaked through the analyzer such that the linear heterodyned term is much stronger than the term proportional to $|\chi_R|^2$. Thus, the signal current is derived from the intensity I'_H of Eq. (41). We must consider all sources of noise — fluctuations in the background signal from the uncrossed analyzer (see Eq. (37)), fluctuations in the background signal from the finite extinction of the analyzer (see Eq. (55)), and the shot noise from these backgrounds

$$(S/N)_{\text{OHD-CARS}} = \frac{\left(\frac{geqA}{\hbar\omega}\right) I'_H}{\left[\left(\frac{geqA}{\hbar\omega}\right)^2 \left\{(|\theta|^2 I_{LO})^2 + (\theta_e^2 I_{LO})^2\right\}(4\varepsilon_a + \varepsilon_c) + \frac{2g^2e^2qA}{\hbar\omega}\left\{|\theta|^2 I_{LO} + \theta_e^2 I_{LO}\right\}\right]^{\frac{1}{2}}}$$

$$= \frac{I'_H}{[(|\theta|^4 + \theta_e^4)\, I_{LO}^2 (4\varepsilon_a + \varepsilon_c) + (|\theta|^2 + \theta_e^2) I_{LO} I_Q]^{\frac{1}{2}}} \,. \qquad (59)$$

Since the value of $|\theta|$, the polarizer uncrossing angle, is an independent parameter, it is adjusted to give the best signal noise ratio.[14]

First consider the shot noise limit with ideal polarizer and no laser fluctuations, i.e., $\theta_e = 0$ and $\varepsilon_a = \varepsilon_c = 0$. The signal to noise ratio of Eq. (59) then becomes optimized at $|\theta| = 0$ ($S/N \to \infty$), but this is simply an artifact of ignoring the $|\chi_R|^2$ terms. In fact, the optimum S/N is given by Eq. (58) of the previous section.

In the limit of large fluctuations and non-negligible extinction

ratio, we have

$$(S/N)_{\substack{\text{OHD-CARS}\\ \text{(fluctuation)}}} \simeq \frac{I_H'}{[|\Theta|^4 + \theta_e^4]^{\frac{1}{2}} I_{LO}(4\varepsilon_a + \varepsilon_c)^{\frac{1}{2}}}$$

$$= \frac{|\Theta|}{(|\Theta|^4 + \theta_e^4)^{\frac{1}{2}}} \frac{1}{(4\varepsilon_a + \varepsilon_c)^{\frac{1}{2}}} \frac{\mathrm{Im}([\chi_R]_{1111})}{[\chi_{NR}]_{1111}} \tag{60}$$

where the last expression has been evaluated for the example discussed above. The signal to noise is maximized when $|\Theta| = \theta_e$ and is given by

$$(S/N)_{\text{OHD-CARS}} \simeq \frac{1}{(2)^{\frac{1}{2}}\theta_e(4\varepsilon_a + \varepsilon_c)^{\frac{1}{2}}} \frac{\mathrm{Im}([\chi_R]_{1111})}{[\chi_{NR}]_{1111}} . \tag{61}$$

4. Comparison of CARS Techniques

To make a comparison of these CARS techniques, consider the detection limit, defined as the ratio of resonant to nonresonant susceptibilities when S/N = 1. Solving Eqs. (52), (57), and (61) for χ_R/χ_{NR}, assuming Lorentzian lineshapes for the resonant susceptibility and dropping the tensor subscripts, we have

$$(\chi_R/\chi_{NR})_{\text{AMP-CARS}} = (4\varepsilon_a + \varepsilon_c)^{\frac{1}{2}}$$

$$(\chi_R/\chi_{NR})_{\text{BS-CARS}} = \frac{4}{\sqrt{3}}\,\theta_e(4\varepsilon_a + \varepsilon_c)^{\frac{1}{2}}$$

$$(\chi_R/\chi_{NR})_{\text{OHD-CARS}} = \sqrt{2}\,\theta_e(4\varepsilon_a + \varepsilon_c)^{\frac{1}{2}}. \tag{62}$$

In a typical experiment, each laser may fluctuate by 15% (rms) and the extinction ratio of a moderate quality polarizer may be about 10^{-4}. Thus, $\varepsilon_a = \varepsilon_c = (.15)^2$, $\theta_e = (10^{-4})^{\frac{1}{2}}$ and averaging over 10 pulses (1 sec

time constant), we have

$$(\chi_R/\chi_{NR})_{AMP-CARS} \approx 10^{-1}$$

$$(\chi_R/\chi_{NR})_{BS-CARS} \approx 8 \times 10^{-3}$$

$$(\chi_R/\chi_{NR})_{OHD-CARS} \approx 1.6 \times 10^{-3}. \qquad (63)$$

Thus, in typical situations the best signal to noise occurs in the heterodyned form of CARS. As one can see from Eq. (62), OHD-CARS is approximately a factor of $(\theta_e)^{-1}$ more sensitive than amplitude CARS.

Knowing the strength of χ_R for the bulk material allows one to predict how small of concentration will be observable using the CARS technique. Naturally if the resonant material is strongly diluted in a second substance, the nonresonant susceptibility is determined by the solvent. Ideally, one wants to use a solvent with a small χ_{NR} to increase the sensitivity. In a typical setup, it should be possible to achieve an extinction of 10^{-6} under favorable circumstances, while little improvement in laser stability can be expected (ϵ = .05). With this improvement, one speculates the practical limit of detection sensitivity to be

$$\chi_R/\chi_{NR} \sim 10^{-4} \qquad \text{(practical limit)}.$$

As an example, consider detecting benzene, using its strong 992 cm^{-1} Raman mode ($\chi_R \sim 30 \times 10^{-14}$ esu for pure benzene), diluted into carbon tetrachloride ($\chi_{NR} \sim 1 \times 10^{-14}$ esu). The practical detection limit is

reached after a volume reduction of 3×10^5, or for concentrations of benzene less than 10 ppm.

Before ending this discussion, it should be cautioned that this practical limit may not be achievable if the input laser powers are low. In a previous discussion it is shown that $I_Q A \approx 10^{-11}$ W while $I_{LO} A \simeq 10^{-6}$ W for 1 kW input beams and $\chi_{NR} = 10^{-14}$ esu. Using this information one can determine χ_R when S/N = 1 in the shot noise limit from Eq. (53). One finds

$$\chi_R \sim 3 \times 10^{-17} \text{ esu.}$$

The shot noise limit becomes $\chi_R/\chi_{NR} \sim 3 \times 10^{-3}$. Thus, the practical limit of 10^{-4} in the benzene case is not attainable in this situation. Fortunately, it is possible to use higher powered laser systems which lower the shot noise limit by $(10)^{3/2} \sim 30$ for each order of magnitude increase in input laser power. Therefore, using 10 kW lasers the practical and shot noise limits are identical, while at higher input powers, shot noise is no longer a limitation.

As mentioned in the discussion of background suppression CARS in part D, there exists the possibility of monitoring the rejected beam from the polarizer and using it for normalization against laser fluctuations. The only noise sources in this case come from shot noise and electronic noise of signal processing, the latter being more important in the experimental setup described in the next section. Principal problems are the difference in response of the two independent optical detectors needed in this arrangement and the electronic signal processing which requires dual input channels and ratioing. With some effort,

photo tubes can be matched and a microprocessor can process the data on a shot-to-shot basis, thus minimizing the electronic noise. To incorporate this noise source into the signal to noise analysis we assume that the electronic noise is proportional to the ratio being measured, similar to the laser power fluctuation contribution of Eq. (45). In the limit of large electronic noise, we have the S/N = 1 limiting susceptibility ratio of

$$(\chi_R/\chi_{NR})_{OHD-CARS} \simeq \theta_e(\varepsilon_{electronic})^{\frac{1}{2}}$$

where $\varepsilon_{electronic}$ is the mean square fluctuation in the ratio due to electronic noise. This can be compared to the result in Eq. (62) for large intensity fluctuations. Using the proper techniques, $(\varepsilon_{electronic})^{\frac{1}{2}} \lesssim 10^{-2} - 10^{-3}$, so increasing the sensitivity by one or two more orders of magnitude.

To summarize, this section has presented a new perspective on nonlinear spectroscopy. Two new techniques BS-CARS and OHD-CARS are obviously needed to complete the overall framework discussed. It is shown that these new arrangements theoretically lead to improvements in the detection sensitivity of two to three orders of magnitude over the usual amplitude CARS case. In the next section, experimental verification of these results is presented.

References

1. J. D. Jackson, Classical Electrodynamics, 2nd ed. (John Wiley & Sons, New York, 1975).
2. N. Bloembergen, Nonlinear Optics, (Benjamin, Reading, Mass., 1977).
3. R. T. Lynch, H. Lotem, and N. Bloembergen, J. Chem. Phys. 66, 4250 (1977).
4. See, for example, A. G. Jacobson and Y. R. Shen, Appl. Phys. Lett. 34, 464 (1979).
5. F. M. Kamga and M. G. Sceats, Opt. Lett. 5, 126 (1980).
6. G. Laufer, R. B. Miles, and D. Santavicca, Opt. Commun. 31, 242 (1979).
7. M. Born and E. Wolf, Principles of Optics, 5th ed. (Pergamon Press, New York, 1975) or R. M. A. Azzam and N. M. Bashara, Ellipsometry and Polarized Light, (North-Holland, New York, 1977).
8. W. M. Tolles, J. W. Nibler, J. R. McDonald, and A. B. Harvey, Appl. Spect. 31, 253 (1977); J. W. Nibler and G. V. Knighten, "Coherent Anti-Stokes Raman Spectroscopy" in Raman Spectroscopy of Gases and Liquids, ed. A. Weber (Springer-Verlag, New York, 1979).
9. A. Owyoung, IEEE J. Quantum Electron., QE-14, 192 (1978).
10. M. D. Levenson and G. L. Eesley, Appl. Phys. 19, 1 (1979).
11. J. L. Oudar, R. W. Smith, and Y. R. Shen, Appl. Phys. Lett. 34, 758 (1979).
12. S. A. Akhmanov, A. F. Bunkin, S. G. Ivanov, and N. I. Koroteev, JETP Lett. 25, 416 (1977); JETP 47, 667 (1978).
13. A. Owyoung, "CW Stimulated Raman Spectroscopy" in Chemical Applications of Nonlinear Spectroscopy, ed. A. B. Harvey (Academic, in

press).

14. G. L. Eesley, M. D. Levenson, and W. M. Tolles, IEEE J. Quantum Electron. QE-14, 45 (1978).

15. M. A. F. Scarparo, J. J. Song, J. H. Lee, C. Cromer, and M. D. Levenson, Appl. Phys. Lett. 35, 490 (1979).

16. A complete listing of macroscopic symmetry properties is contained in Nonlinear Optical Phenomena by P. N. Butcher (Ohio State, Columbus, 1965).

17. The most common signal generation processes are discussed in Ref. 8.

18. A. Compaan and S. Chandra, Opt. Lett. 4, 170 (1979).

19. A. C. Eckbreth, Appl. Phys. Lett. 32, 421 (1978).

20. M. D. Levenson and N. Bloembergen, Phys. Rev. B10, 4447 (1974); R. F. Begley, A. B. Harvey, and R. L. Byer, Appl. Phys. Lett. 25, 387 (1974).

21. J. J. Song, G. L. Eesley, and M. D. Levenson, Appl. Phys. Lett. 29, 567 (1976).

22. M. A. Yuratich and D. C. Hanna, Mol. Phys. 33, 671 (1977).

23. D. A. Kleinman, Phys. Rev. 126, 1977 (1962).

24. See, for example, A. Yariv, Introduction to Optical Electronics, Chap. 10 (Holt, Rinehart, and Winston, New York, 1971).

Figure Captions

Fig. 1 Possible pairs of parameters used to describe a general polarization state. $(\mathcal{E}_x, \mathcal{E}_y)$, (ξ, δ), or (θ, ϕ).

Fig. 2 Orientation of quarter-wave plate and linear analyzer to transmit the elliptical polarization state, $\hat{e}_\alpha$, defined in Eq. (10), propagating along + z-axis. The fast axis of the quarter-wave plate makes an angle η with the x-axis; the transmission axis of the linear analyzer makes an angle ζ with the x-axis. For transmission of $\hat{e}_\alpha$, $\eta = \theta$ and $\zeta = \theta + \phi$.

Fig. 3 Typical Stimulated Raman Gain Spectroscopy (SRGS) experimental setup, using cw probe and amplitude modulated-cw pump beams and lock-in detection.

Fig. 4 Typical Raman Induced Kerr Effect Spectroscopy (RIKES) experimental setup, using cw probe and pulsed pump beams with gated detection. Note polarization-sensitive detection.

Fig. 5 Typical Coherent Anti-Stokes Raman Spectroscopy (CARS) experimental setup, using pulsed probe and pump beams with gated detection.

Fig. 6 Hierarchy of four-wave mixing spectroscopy techniques.
SRS - Stimulated Raman Scattering Processes.
SG - Signal Generation Processes.
See text for explanation of acronyms.

Fig. 7 General polarization-sensitive CARS experimental setup. Compare with the CARS setup of Fig. 5, noting the addition of polarizers in the probe and pump beams and the signal beam analyzer ($\lambda/4$ plate and linear polarizer). The additional double monochroma-

tor and PMT (photomultiplier tube), drawn with fine lines, are used in the ratioing scheme described in the text.

Fig. 8 The polarization arrangement of Song, et al.[21] for background suppression in four-color CARS experiment, $\omega = \omega_a + \omega_b - \omega_c$. This has been appropriately dubbed "asterisk."

Figure 1

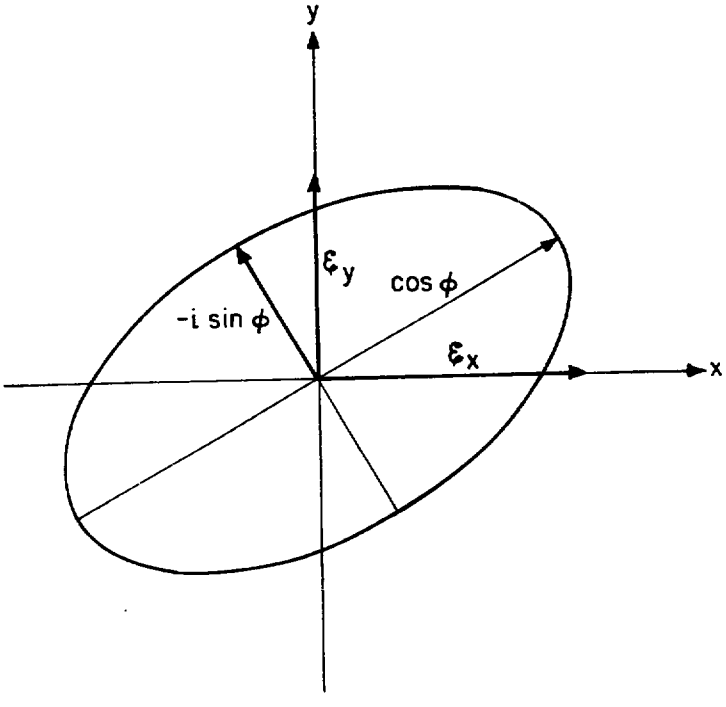

$$\tan\xi \; e^{i\delta} \equiv \mathcal{E}_y/\mathcal{E}_x$$

$$\tan(2\theta) = \frac{2\,\mathrm{Re}[\mathcal{E}_x^* \mathcal{E}_y]}{|\mathcal{E}_x|^2 - |\mathcal{E}_y|^2} = \frac{2\tan\xi\cos\delta}{1-\tan^2\xi}$$

XBL 807-5526

$$\sin(2\phi) = \frac{2\,\mathrm{Im}[\mathcal{E}_x^* \mathcal{E}_y]}{|\mathcal{E}_x|^2 + |\mathcal{E}_y|^2} = \frac{2\tan\xi\sin\delta}{1+\tan^2\xi}$$

Figure 2

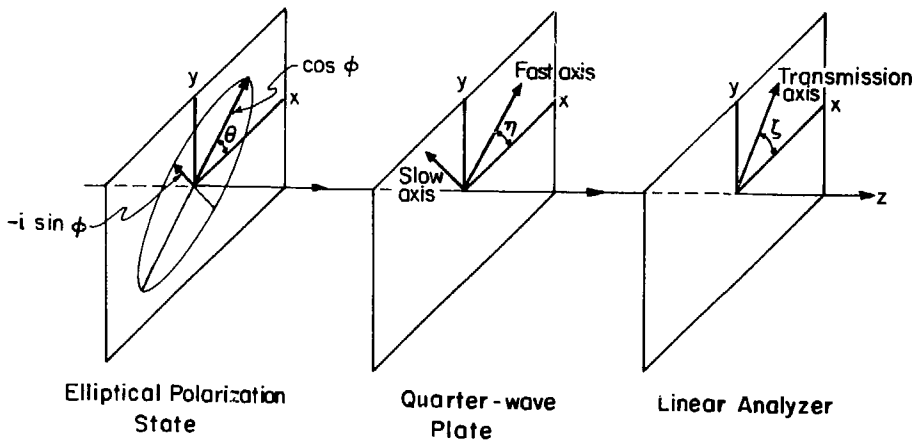

XBL 807-5527

Figure 3.

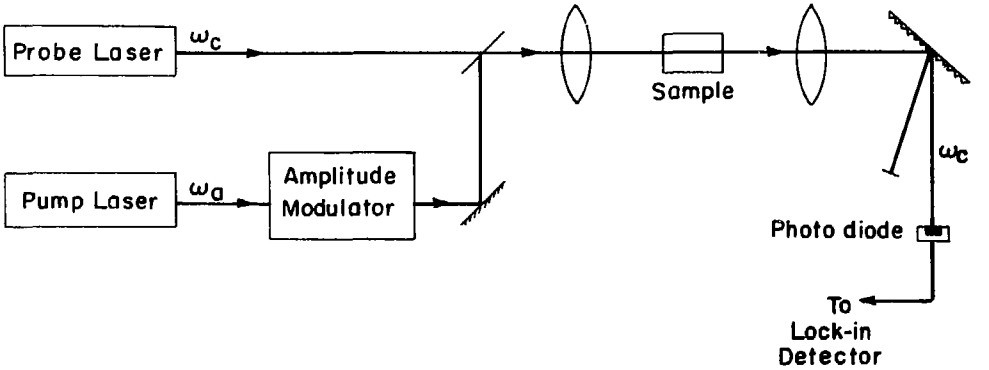

X 6L 807-5528

Figure 4

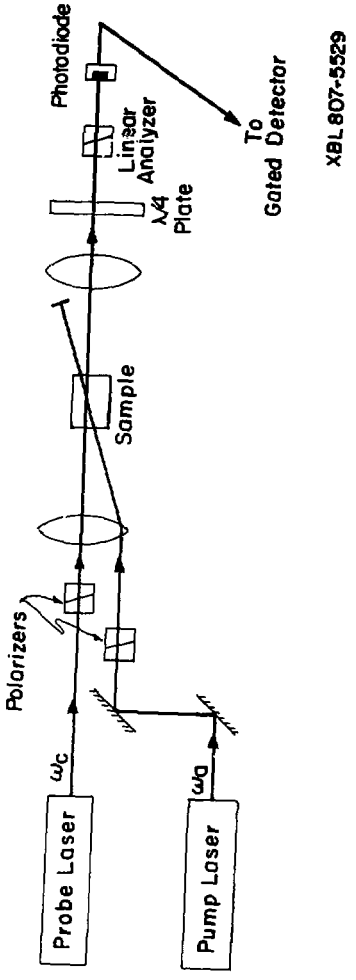
Probe Laser
Pump Laser
ω_c
ω_a
Polarizers
Sample
λ/4 Plate
Linear Analyzer
Photodiode
To Gated Detector
XBL 807-5529

Figure 5

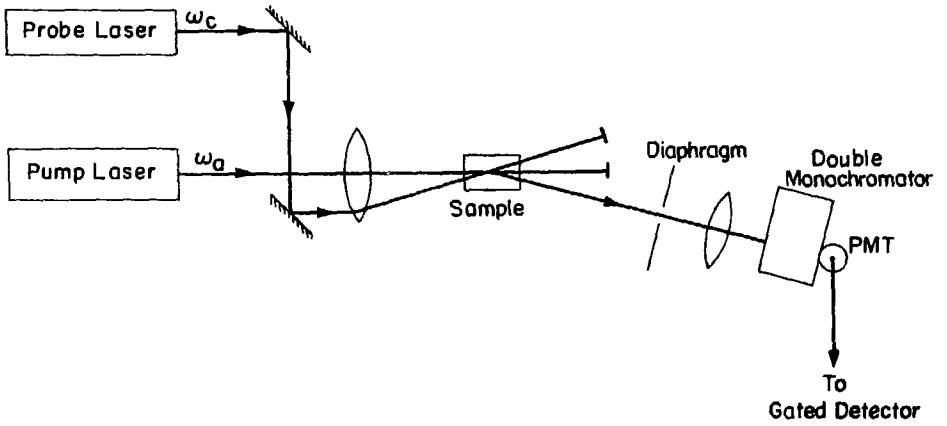

XBL 807-5530

Figure 6

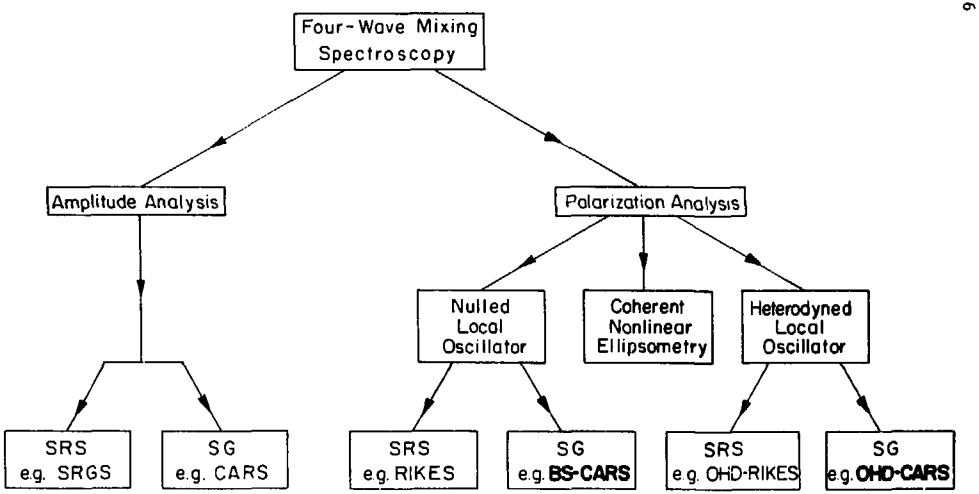

XBL 807-5531

Figure 7

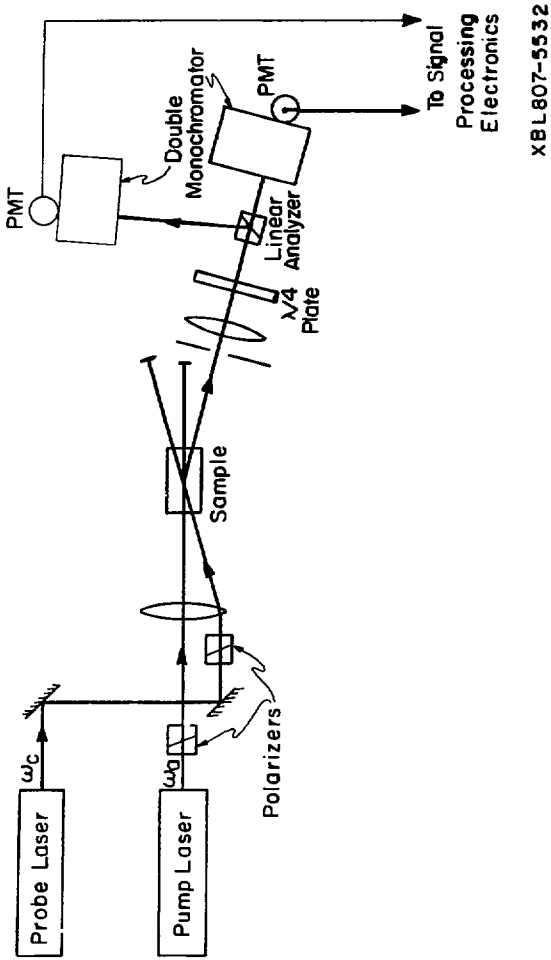
Probe Laser
Pump Laser
ω_c
ω_0
Polarizers
Sample
λ/4 Plate
Linear Analyzer
Double Monochromator
PMT
PMT
To Signal Processing Electronics
XBL807-5532

Figure 8

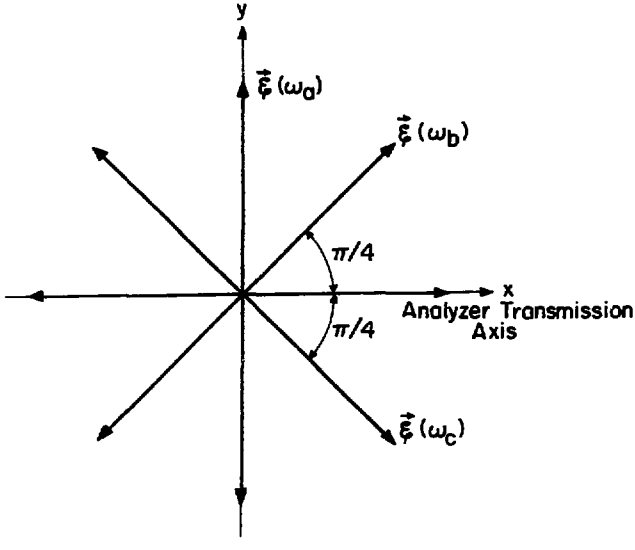

XBL 807-5533

III. EXPERIMENTAL DEMONSTRATION AND DISCUSSION OF BACKGROUND SUPPRESSION-CARS AND OPTICAL HETERODYNED DETECTION-CARS

The theoretical background for many forms of four-wave mixing spectroscopy has been presented in the preceding section, with emphasis placed on the possible forms of coherent anti-Stokes Raman spectroscopy (CARS). Amplitude-CARS (CARS without polarization analysis) has been a well established technique[1] and has become the most popular type of nonlinear spectroscopy.[2] In Section II we have introduced two new methods of performing CARS experiments using polarization-sensitive detection techniques. With one polarization arrangement, the nonresonant background may be eliminated leaving only the resonant spectrum — this has been called "background suppression"-CARS or BS-CARS. A modified polarization scheme may allow the examination of either the real or the imaginary part of the resonant susceptibility and has been named "optical heterodyned detection"-CARS or OHD-CARS. In both cases, it has been predicted that there should be an increase in the ability to detect weak resonances over the amplitude-CARS technique. In this section, we present the results of experimental studies[3] made to demonstrate BS-CARS and OHD-CARS and to evaluate their detection sensitivity.

We begin this section with a description of the technique and apparatus used earlier in our laboratory to perform amplitude-CARS measurements. This was the basic nonlinear spectroscopy system which was later modified to make polarization-sensitive measurements, although many of its features remained unchanged. Next, the method to separate the resonant and nonresonant contributions to the CARS signal is described in a form appropriate for the experimental work to be presented.

Included in this discussion are the explicit changes made in the amplitude-CARS setup. This is followed by the experimental demonstration of BS- and OHD-CARS, including a discussion of the sample, the experimental spectra, the analysis of these spectra and the detection sensitivity of these techniques. This section concludes with a discussion of the types of problems which can be studied with these polarization-sensitive techniques and their limitations.

A. The Standard Amplitude-CARS Technique and Apparatus

In the usual CARS setup two pulsed lasers with frequency separation equal approximately to a vibrational excitation of the sample are used to generate a nonlinear output beam at frequency $\omega = 2\omega_a - \omega_c$, where $\omega_a > \omega_c$ are the two input frequencies. As described in Section II, when $\omega_a - \omega_c$ matches a Raman-active excitation, there is an enhancement in the resonant susceptibility which enhances the nonlinear output (thus allowing CARS to be used as a form of spectroscopy). In this segment, we describe the experimental aspects of this technique.

The primary parts of the CARS setup (and often the most expensive) are the laser sources. High peak power (> 1 kW) and narrow bandwidth (< 1 cm^{-1}) characterize useful laser systems for nonlinear spectroscopy, since the nonlinear output is strongly dependent on the input intensities and typical Raman modes have widths from 1 to 10 cm^{-1}. Furthermore, at least one of the laser sources must be tunable, so that the dispersion of the susceptibility can be measured. Flashlamp-pumped dye lasers satisfy these criteria and were easily constructed for use in these experiments. (Details of this system can be found in Ref. 4). Tuning of the dye lasers

was achieved by either an interference filter/etalon combination[5] or a telescope/grating combination,[6] with each scheme giving a linewidth less than 0.2 cm^{-1} and peak power of 1-10 kW. Operating at 10 pps, this laser system has proven quite useful for CARS measurements.

Another important experimental consideration, especially in dispersive media, is the achievement of phasematching as described in Section IIA. Essentially, this is a statement of momentum conservation among the four photons. Materials with normal dispersion ($\frac{dn}{d\omega} > 0$) require the use of a noncollinear geometry to achieve phasematching. The usual arrangement for phasematching is shown in Fig. 1, with the angle ψ between $\vec{k}_a$ and $\vec{k}_c$ being about 1-2°. To calculate ψ, precise information is needed about $n(\omega)$, the linear refractive index. In many cases ψ can only be roughly estimated, thus the experimental setup must allow for the optimization of the phasematching by having ψ be easily adjustable. A convenient arrangement to bring the two input beams to a common focus while maintaining the flexibility in the phasematching angle is shown in Fig. 2. The two input beams are made parallel before they are brought to a focus by lens L1. The angle ψ is determined by the spacing of the beams before the lens and the focal length of L1. The phasematching is adjusted by varying the separation of the beams through translation of mirror M2 normal to the axis of the lens. (This arrangement also allows easy alignment of the detection system along the expected output beam path. The ω_c beam can be translated to duplicate the direction of the output beam as shown in the insert of Fig. 2.)

Figure 2 also indicates the other major part of a CARS setup — the detection system. A photomultiplier (PMT) is usually needed to detect the nonlinear output in experiments involving the generation of a new

frequency (signal generation processes, section IID), such as CARS. The spatial separation of the beams after the sample (due to the phasematching condition) aids in discriminating against the input beams, while the double monochromator further spectrally discriminates against linear scattering of the input frequencies. It is possible then to obtain a PMT signal dependent only on the nonlinear output and the ever-present dark current. The latter is minimized by using gated detection of the PMT signal. The present system included dual-channel gated electrometers[7] (reference and signal channels) with the capability of outputting the analogue quotient of these signals onto a recorder.

An amplitude-CARS spectrum is recorded by the following procedure: (1) input frequencies adjusted to the desired frequency difference, (2) the phasematching angle calculated and the appropriate separation of the input beams set, and (3) the detection system approximately aligned (as described above) and the double monochromator adjusted to the output frequency. The nonlinear signal will be present even if the frequency difference does not match the Raman mode, due to contributions from the nonresonant susceptibility (Section IIA). Once the nonlinear signal is found and optimized, the dispersion of nonlinear signal can be recorded versus the difference frequency $\omega_a - \omega_c$. The CARS system in Fig. 2 is capable of scanning over a range of approximately 100 cm^{-1} while taking an undistorted spectrum. (Note: This scanning range requires that the double monochromator be continuously adjusted to match the changing output frequency.) For usual Raman resonances, 1-10 cm^{-1} wide, this scanning range is adequate to record useful CARS spectra.

The dispersion of the amplitude-CARS signal is a direct measurement of the square magnitude of the resonant and nonresonant susceptibilities

(see Section IID for details and Section IVC for the inclusion of linear absorption effects). The presence of the nonresonant background alters the lineshape of the resonant signal through interference effects and provides a nondispersive background whose fluctuations mask weak resonances. In spite of these problems, amplitude-CARS spectra are very informative and relatively easy to obtain (spontaneous Raman spectra requiring hours are being supplanted by CARS spectra taken in a few minutes). The principal information in these spectra are the frequency and strength of the Raman resonances. Because four photons are involved, a great deal about the polarization properties of the resonant susceptibility can also be extracted. As shown in Fig. 2, each input beam is polarized before entering the sample. The inclusion of a half-wave plate in the ω_a beam allows this beam's linear polarization to be rotated to an arbitrary angle to the ω_c beam's polarization. In isotropic media, we are generally only interested in two input polarization arrangements — ω_c parallel to ω_a or ω_c perpendicular to ω_a. From the strengths of $[\chi_R]_{1111}$ and $[\chi_R]_{1221}$, all independent elements of χ_R can be found.[8] In crystalline media, there is a wealth of information to be learned using an oriented sample and different polarization combinations — each case must then be considered separately.[9]

We end this section by briefly describing the limitations of this CARS setup. First of all, fluctuations in the laser intensity, including long term drifts, were uncompensated, since the use of nonlinear reference signal required additional detection equipment. Variations in the CARS spectrum from this source could be eliminated only by ensuring the stability of the input lasers (using new dye, flashlamps, etc.). A second source of distortion in the spectra results from a deviation from

perfect phasematching as the difference frequency is scanned. For small Raman shifts the phasematching angle ψ is linearly proportional to the Raman shift — typically $\psi \sim 30$ mrad for $\omega_R \sim 1000$ cm^{-1} and the phasematching peak has a half-width of about 1 mrad. Scans of 30 cm^{-1} or more require adjustment of ψ. Our CARS setup had no provision for such adjustments, except for manual changes made during the scan. Finally, a nonlinearity in the electro-mechanical linkage which simultaneously varied the ω_c laser frequency and the double monochromator setting caused loss of signal during extended scans. It was empirically determined that useful scans of ~ 200 cm^{-1} could be made if the monochromators were used at low resolution ($\Delta\lambda \approx 20$Å, 500 μm slits) and if ψ was tweaked during the scan. If reductions of the slit widths became necessary to eliminate unwanted signals, the useful frequency range was greatly reduced — in some instances scans had to be limited to ~ 10 cm^{-1}. However, being cognizant of these shortcomings, this system proved quite adequate to perform CARS experiments, including the polarization-sensitive measurements described in the next section.

B. Polarization-Sensitive CARS Techniques and Apparatus

To circumvent the basic limitations of the amplitude-CARS technique one needs to control the nonresonant contribution to the nonlinear signal, so the resonant part can be studied in more detail. The technique described here to manipulate the nonresonant contribution is polarization-sensitive detection, i.e. the introduction of a polarization analyzer into the nonlinear output beam before it reaches the detector.

The first use of such a detection scheme in a CARS system was by Levenson and Bloembergen[10] in studies of Raman modes in benzene and diamond. They clearly demonstrated that near a Raman resonance the polarization state of the total nonlinear output is highly dispersive by measuring the variation with frequency of the angle of the semi-major axis of the elliptically polarized output (see Fig. 6, Ref. 10). To observe this dispersive behavior, it was necessary to introduce an angle (other than 0° or 90°) between the linear polarizations of the input fields, $\vec{\mathcal{E}}(\omega_a)$ and $\vec{\mathcal{E}}(\omega_c)$. Also included in this work were several polarization-sensitive CARS spectra in which the signal intensity through a fixed polarizer was monitored versus $\omega_a - \omega_c$. Although one of the polarization arrangements used by Levenson and Bloembergen with benzene completely eliminated the resonant contribution to the output, the ability of the technique to discriminate against the nonresonant background was not discussed or demonstrated.

The full utility of polarization-sensitive CARS was not understood until a simple distinction was made between the resonant and nonresonant parts of the total nonlinear output field.[3] In the simple case of benzene used in Ref. 10, we can write

$$\vec{\mathcal{E}}_R = B\{[\chi_R]_{1111}\cos\delta\ \hat{x} + [\chi_R]_{1221}\sin\delta\ \hat{y}\}$$

$$\vec{\mathcal{E}}_{NR} = B\{[\chi_{NR}]_{1111}\cos\delta\ \hat{x} + [\chi_{NR}]_{1221}\sin\delta\ \hat{y}\} \qquad (1)$$

where we have written the resonant (R) and nonresonant (NR) fields for an isotropic medium[8] assuming the input fields to be polarized as $\hat{\mathcal{E}}(\omega_a) = \hat{x}$ and $\hat{\mathcal{E}}(\omega_c) = \cos\delta\ \hat{x} + \sin\delta\ \hat{y}$. B is a nondispersive constant.

If we assume that the nonresonant susceptibility is also nondispersive and is a real quantity (away from any resonances), then $\vec{\mathcal{E}}_{NR}$ is in a fixed linear polarization state and is constant in magnitude. On the other hand the resonant susceptibility is very dispersive in both magnitude and in phase (relative to $\vec{\mathcal{E}}_{NR}$). It is usually true however, that the ratio $[\chi_R]_{122i}/[\chi_R]_{1111}$ is real and nondispersive for tens of wavenumbers, so that $\vec{\mathcal{E}}_R$ is also in a fixed linear polarization state. Figure 3 shows one possible set of directions of the input and output polarizations using the strongly polarized 992 cm^{-1} Raman mode of benzene as an example.

With the separation of the resonant and nonresonant fields as in Eq. (1) it is immediately clear how polarization-sensitive detection can totally eliminate the nonresonant field leaving only a spectrum of resonances. We insert a linear polarization analyzer after the sample and adjust it to transmit the polarization state orthogonal to $\vec{\mathcal{E}}_{NR}$. (In Fig. 3 the transmission axis is indicated by $\hat{\zeta}$). Experimentally, this can be done by nulling the nonlinear signal when the frequency difference is far from any Raman resonance, then only the nonresonant field contributes. To achieve a good null (say reduction of the signal strength by four to six orders of magnitude), a calcite Glan-Thompson prism polarizer mounted on a precision rotational mount with 3 mrad resolution should be used as the analyzer. (Similar polarizers should be used to define the polarization states of the incoming laser beams). In addition, one should expect $\vec{\mathcal{E}}_{NR}$ to be slightly elliptically polarized, since there is nearly always a residual strain birefringence in the sample cell windows or in the other pieces of optics in the beam path. A quarter-wave plate should help to eliminate this

slight ellipticity and can be as simple as a plastic-sheet wave plate or as sophisticated as a Babinet-Soleil compensator. Figure 4 shows a complete experimental setup to eliminate the nonresonant field — a technique we call "background suppression"-CARS. The only distinction between the setup in Fig. 4 and the standard amplitude-CARS setup in Fig. 2 is the addition of a collimating lens, a quarter-wave plate, and a Glan-Thompson polarizer. Thus only minor modifications are necessary to make the conversion from amplitude-CARS to background suppression-CARS. (See Section II for additional theoretical details, such as the optimal choice of the angle δ).

The experimental apparatus for the second new variation of the CARS technique, optical heterodyned detection-CARS, is identical to that used for background suppression — only the technique is altered. The basic idea is illustrated in Fig. 5(a), where the transmission axis of the linear analyzer, $\hat{\zeta}$, is rotated by a small angle θ_0. The intensity transmitted through the analyzer becomes

$$I \propto |\theta_0 \mathcal{E}_{NR} + \mathcal{E}_R \sin\alpha|^2$$

$$\propto \theta_0^2 \mathcal{E}_{NR}^2 + 2\theta_0 \mathcal{E}_{NR} \sin\alpha \; \mathrm{Re}[\mathcal{E}_R] \qquad (2)$$

where $(\theta_0 \mathcal{E}_{NR})$ is the amount of the nonresonant amplitude allowed to leak through the analyzer; $(\mathcal{E}_R \sin\alpha)$ is the component of $\vec{\mathcal{E}}_R$ which is normally transmitted by the analyzer (even in the null position). In the second line of Eq. (2) we assume a weak resonance so the only dispersion is linear in the real part of $\mathcal{E}_R$. Since $\mathrm{Re}[\mathcal{E}_R] \propto \mathrm{Re}[\chi_R]$, uncrossing the linear polarizer yields a spectrum displaying the real

part of the resonant susceptibility. [Note: if a quarter-wave plate is present, it too must be rotated by the same angle θ_0 so that its axes match the axes of the polarizer, thus introducing the same phase shift to the total transmitted field].

An alternate form of OHD-CARS involves the intentional inclusion of a fixed quarter-wave plate with fast axis $\hat{n}$ along the direction of $\vec{\mathcal{E}}_{NR}$ as shown in Fig. 5(b). Again the linear analyzer is rotated by θ_0 with the resulting transmission becoming

$$I \propto |-i\theta_0\mathcal{E}_{NR} + \mathcal{E}_R \sin\alpha|^2$$

$$\propto \theta_0^2\mathcal{E}_{NR}^2 + 2\theta_0\mathcal{E}_{NR}\sin\alpha \mathrm{Re}[-i\mathcal{E}_R] \tag{3}$$

where now the quarter-wave plate has phase-shifted the nonresonant contribution by $-\pi/2$ relative to the transmitted component of $\mathcal{E}_R$. Since $\mathrm{Re}[-i\mathcal{E}_R] = \mathrm{Im}[\mathcal{E}_R]$, this arrangement displays a spectrum of the imaginary part of the resonant susceptibility. The ability to display either the real or the imaginary part of χ_R is very useful in spectroscopy, especially when the spectrum contains many closely spaced lines.

As pointed out in Section IID, we have a "built-in" nonlinear reference signal which can be used to eliminate power fluctuations in the BS- or OHD-CARS signal. As shown in Fig. 7 of Section II, the rejected signal from the Glan-Thompson (GT) polarizer is monitored for this purpose, since it depends predominantly on the nondispersive, nonresonant signal (at least in the weak resonance case). Although conceptually correct, the apparatus described in this figure is some-

what impractical, since it requires the use of a second double monochromator. Two alternative systems using one double monochromator are shown in Fig. 6. In part (a) of this figure the GT polarizer is held in a fixed position after the double monochromator, while a half-wave plate is used to rotate the output from the quarter-wave plate. Rotating the half-wave plate is the equivalent to a rotation of the GT polarizer. This setup was used in the experiment, but was found to have poor extinction (nulls of only 10^{-3} could be obtained), since the double monochromator altered the polarization state of the signal beam before it reached the GT analyzer. The arrangement shown in Fig. 6(b) is proposed to allow the polarization analysis before the double monochromator. In this case the signal beam transmitted through the GT polarizer and the redirected reference (rejected) beam are passed through the same monochromators but at different heights — and then sent to different photomultipliers. Such a scheme thus eliminates any polarization distortion occurring within the monochromators.

In conclusion, we have described the experimental techniques and apparatus to be used in BS- and OHD-CARS. In addition we have indicated futher modifications to the experimental setup to use the built-in reference signal rejected by the polarization analyzer. Thus we have seen how to control the nonresonant field $\vec{\mathcal{E}}_{NR}$, allowing normalized spectra proportional to either $|\chi_R|^2$, $\mathrm{Re}[\chi_R]$, or $\mathrm{Im}[\chi_R]$ to be taken. The experimental confirmation of these ideas is demonstrated in the next section.

C. Background Suppression- and Optical Heterodyned Detection-CARS: Experimental Measurements and Analysis

This section provides experimental verification that polarization-sensitive CARS techniques can yield additional information about the resonant susceptibility, beyond that attainable from amplitude-CARS experiments. We present spectra demonstrating the suppression of the nonresonant background and the exhibition of the separate real and imaginary parts of χ_R. Futhermore, it is shown that both BS- and OHD-CARS have much improved detection sensitivity over the previously used CARS technique. The specific techniques and apparatus are described in the two preceding parts of this section. We begin this segment with a characterization of the sample and laser sources used in this study. This is followed by a presentation of the experimental spectra and an analysis of these measurements, including a comparison with earlier work and an estimation of the detection sensitivity.

1. Sample Selection

Although many materials exhibit Raman resonances, it was important to choose a well characterized sample for demonstration purposes. The Raman modes of benzene have been well studied, especially the 992 cm^{-1} mode (the symmetric stretch mode, ν_2) which has been examined in both linear[11] and nonlinear[12] spectroscopy. Spontaneous Raman spectra show that in addition to the strong mode ν_2 at 992.2 cm^{-1} there are four weaker modes nearby. The strengths, widths, and frequencies of these five modes have been measured by Lynch and Lotem[12] and a table of their results is presented in Fig. 7. The assumed form of the resonant susceptibility is a sum of individual complex Lorentzians. We write

$$[\chi_R]_{1111} = \sum_j \frac{(A_R)_j}{(\omega_R)_j - (\omega_a - \omega_c) - i(\Gamma_R)_j} \tag{4}$$

It has also been established that these modes are very strongly polarized, that is the measured depolarization ratio, ρ_R, is zero. As pointed out in Section II, ρ_R can be written as the ratio of $[\chi_R]_{1221}$ to $[\chi_R]_{1111}$, so $[\chi_R]_{1221} \approx 0$ for these modes.

To control the strength of the resonant susceptibility, increasingly dilute solutions of benzene in carbon tetrachloride were prepared — from 10% to 0.1% by volume. Carbon tetrachloride was chosen as the solvent because it is known to be nondispersive in this frequency range and is readily available in high purity. Furthermore, Levenson and Bloembergen[13] have previously made a direct comparison of the resonant susceptibility of benzene and the nonresonant susceptibility of carbon tetrachloride, which can be used for comparison with the result determined here. As shown in Section II, it is this ratio of χ_R/χ_{NR} which determines the signal to noise ratio for CARS; and it is χ_R/χ_{NR} which can be measured from the CARS spectrum. A discussion of the results Ref. 13 will be included with the analysis of the present experimental determination given below.

2. Lasers

The general characteristics of the flashlamp-pumped dye lasers used in the experiment have already been discussed. For the Raman mode in benzene, the frequency separation of 992 cm^{-1} required the use of two different laser dyes. For the ω_a-laser (upon which the signal was quadratically dependent) we used Rhodamine 6G tuned[5] to $\lambda_a \approx$

5950Å (16805 cm^{-1}). The ω_c-laser was operated at a frequency of about ω_a - 992 cm^{-1} or 15813 cm^{-1} corresponding to 6323Å (Kiton Red dye). Both dyes were used at 10^{-4}M concentrations in 1:1 water to methanol solutions. During the course of the experiment the Rhodamine 6G laser remained fixed at λ_a, while the Kiton Red laser was tuned.[6] A hand-held viewing etalon (Molectron) with a free spectral range of 1.1 cm^{-1} allowed frequent observation of the lasers' linewidths, ensuring narrow-band operation (< 0.2 cm^{-1}).

The lasers had pulse durations of about 1 μsec and operated at 10 pulses per second. For these experiment, the output powers were 7 kW at ω_a and 3 kW at ω_c in beams that were ~ 2 mm in diameter with a full angle divergence of ~ 1 mrad. Both beams were predominantly linearly polarized with multi-mode transverse profiles. Throughout these experiments, laser characteristics remained stable.

3. Experimental Spectra

Using the experimental setup indicated in Fig. 4 (with an angle of ~ 71.5° between the input polarizations), initial observations were made of polarization-sensitive spectra using a 10% solution of benzene in CCl_4. Background suppression was achieved by nulling the nonlinear signal with the frequency detuned aproximately 40 cm^{-1} below the expected Raman resonance. The scanable laser was then tuned through the resonance, giving the spectrum proportional to $|\chi_R|^2$ with a very high signal to noise ratio. The concentration of benzene was further reduced to 0.1%, and the spectrum repeated. The result is displayed in part (a) of Fig. 8, which shows the "CARS" signal of the 992 cm^{-1} Raman mode of benzene free from any nonresonant contribution. It is well known[12] that

this mode of benzene is very nearly Lorentzian (as given in Eq. (4)), therefore $|\chi_R|^2 \propto (\Delta\omega^2 + \Gamma_R^2)^{-1}$ where $\Delta\omega = \omega_R - (\omega_a - \omega_c)$. Although this spectrum of $|\chi_R|^2$ is noisy, it has the general shape of a Lorentzian without the distortion apparent in the usual amplitude-CARS spectrum. In fact, a conventional CARS spectrum of this resonance with 0.1% benzene would have a resonant signal strength of only about 3% of the non-resonant background, which is more difficult to detect than the BS-CARS signal in Fig. 8(a).

Using the heterodyning techniques described in part B, we have also displayed the imaginary and real parts of this resonant susceptibility, as shown in Figs. 8(b) and (c), respectively. These spectra were made using the experimental apparatus of Fig. 6(a), which provides a normalized output signal. To obtain the heterodyned spectrum of $\mathrm{Im}(\chi_R)$, the quarter-wave plate and Glan-Thompson analyzer were first set to the same positions used in background suppression case discussed above, then only the Glan-Thompson was rotated by an angle $\theta_0 = 2.7°$ or 47 mrad (see Eq. (3)). The dispersion of $\mathrm{Re}(\chi_R)$ was recorded by rotating the analyzer to about 8° or 140 mrad (see Eq. (2)) without including the quarter-wave plate in the apparatus. Again, assuming a complex Lorentzian form for χ_R, the frequency dependences of the imaginary and real parts are: $\mathrm{Im}(\chi_R) \propto (\Delta\omega^2 + \Gamma_R^2)^{-1}$ and $\mathrm{Re}(\chi_R) \propto \Delta\omega/(\Delta\omega^2 + \Gamma_R^2)$, which are approximately confirmed by the experimental spectra.

In Fig. 8 we have plotted the "relative" signal strength versus the Stokes shift, $\omega_a - \omega_c$, of the input frequencies. The relative signal strength $\mathcal{R}$ is to be defined as the ratio of the intensities derived from the output field components parallel to the transmission axis of the analyzer ($\mathcal{E}_\parallel$) and orthogonal to this axis ($\mathcal{E}_\perp$). Formally,

$$\mathcal{R} \equiv \frac{|\mathcal{E}_{\parallel}|^2}{|\mathcal{E}_{\perp}|^2} \approx \frac{I_{\parallel}}{I_{\perp}} \tag{5}$$

In this way the spectra in Fig. 8 are independent of the absolute signal strengths.

The heterodyned signals were taken already incorporating this normalization, with the scales for these signals determined by the height of the off-resonant (background) signal. The amount of the nonresonant signal leaked through in this case was θ_0^2 times the total signal before the analyzer, so that $\mathcal{R} = \theta_0^2$ for the background level. $\mathcal{R} = (.047)^2 = 2.2 \times 10^{-3}$ for the imaginary spectrum and $\mathcal{R} = (.140)^2 = 20. \times 10^{-3}$ for the real spectrum (see the vertical scale of Fig. 8).

The background suppression spectrum, however, was not taken with the normalization setup, and therefore required an independent measurement of $I_{\perp}$ to determine the relative signal strength. This measurement was performed in the following way: (I) at the peak of the $|\chi_R|^2$ spectrum, the height of the resonant signal was noted, (2) going far off resonance the analyzer was then uncrossed until the signal level matched the resonant signal level, and (3) the uncrossing angle, γ, was noted. γ^2 became a measure of the ratio of resonant to nonresonant signals, or $\mathcal{R} = \gamma^2$. For the 0.1% benzene in carbon tetrachloride solution, we found $\gamma = 1.1°$ (19 mrad) ± 15%. Thus the peak height of Fig. 8(a) was scaled to $\mathcal{R} = (.019)^2 = 0.36 \times 10^{-3}$. From the information of the relative strengths of $I_{\parallel}$ and $I_{\perp}$ we can determine the ratio of χ_R/χ_{NR} for this solution of benzene and estimate the detection sensitivity of these new techniques.

As a final note on the methods used to obtain the spectra in

Fig. 8, it should be noted that even in the null position the nonresonant signal was never totally extinguished by the polarization analyzer. Therefore, each spectrum had this residual background which was subtracted from the signal before the relative scale was marked on the vertical axis. For the background suppression case, this residual background is indicated by the height of the zero level above the baseline of the figure.

A. Analysis and Discussion

Using the information provided in the preceding section, we first determine our experimental value of χ_R/χ_{NR} for the benzene-carbon tetrachloride solution, then compare this result with that obtained by Levenson and Bloembergen.[13] As we will see, additional information about this sample is obtained upon examining these spectra and making this comparison. Also we estimate the limiting value of χ_R/χ_{NR} observable with this experimental setup and indicate what this limiting value will be for other samples.

In the preceding section we have described experimental measurements to determine the relative signal strength $\mathcal{R}$, defined in Eq. (5) and used in Fig. 8; now we relate $\mathcal{R}$ to the fields and susceptibilities involved in this sample. For example, in the background suppression case we have (from Fig. 3) the field parallel to the analyzer axis given by $\mathcal{E}_R \sin\alpha$, while the orthogonal component is dominated by $\mathcal{E}_{NR}$. Therefore,

$$\mathcal{R} \equiv \frac{|\mathcal{E}_{\parallel}|^2}{|\mathcal{E}_{\perp}|^2} = \frac{|\mathcal{E}_R \sin\alpha|^2}{|\mathcal{E}_{NR}|^2} = \frac{|\chi_R|^2}{4|\chi_{NR}|^2} \tag{6}$$

where we have taken $\alpha = 45^\circ$ as in Fig. 3 and used the expressions for the fields given in Eq. (1), which matches our experimental situation. On the other hand, for the heterodyned cases, $\mathcal{E}_{\parallel}$ can be deduced from Eqs. (2) and (3), while the rejected intensity is still predominantly due to the nonresonant field. For the real part of χ_R we have

$$\mathcal{R} = \frac{|\theta_0 \mathcal{E}_{NR} + \mathcal{E}_R \sin\alpha|^2}{|\mathcal{E}_{NR}|^2}$$

$$\approx \theta_0^2 + \theta_0 \mathrm{Re}[\chi_R]/\chi_{NR} \tag{7}$$

which clearly shows that away from resonance, we have the background value of $\mathcal{R} = \theta_0^2$ as discussed previously. A similar expression can be derived for the imaginary part. (Here we have assumed θ_0 is a small angle, but this restriction can be removed by proper consideration of Fig. 5).

The best measurement of $\mathcal{R}$ (as it depends upon the resonant susceptibility) comes from the background suppression case, Eq. (6), since this value is quadratically dependent on χ_R/χ_{NR}. From the measured value of $\mathcal{R}$ at the resonance peak, we have

$$\mathcal{R} = \gamma^2 = \frac{|\chi_R|^2}{4|\chi_{NR}|^2} \Rightarrow \chi_R/\chi_{NR} = 2\gamma \tag{8}$$

which implies $\chi_R/\chi_{NR} = 2(.019) = .038$ for our 0.1% sample. Correcting for the reduced concentration, we have

$$\chi_R(C_6H_6)/\chi_{NR}(CC\ell_4) = 38. \tag{9}$$

where $\chi_R(C_6H_6)$ is the peak value of the resonant susceptibility for pure benzene and $\chi_{NR}(CC\ell_4)$ is the nonresonant susceptibility of pure carbon tetrachloride. The angle γ was only measurable to ±15% (this corresponds to the 3 mrad accuracy of the rotation mount used in making the measurement of the 19 mrad angle), thus this ratio may also be in error by this percentage. Of course, the measurement accuracy of γ would be much improved if we had chosen to perform the calibration with a 1% solution, where γ would be an order of magnitude larger.

Let us now compare this value of χ_R/χ_{NR} with that obtained by Levenson and Bloembergen (LB).[13] In their case the ratio was measured by finding the frequency separation between the maximum and minimum of an amplitude-CARS spectrum.[14] To predict the frequency separation, $\Delta\bar{\nu}$ (cm^{-1}), they first had to assume a form for the resonant susceptibility — the Lorentzian form of Eq. (4) being their choice, $\chi_R(\Delta\omega) = \chi_R\Gamma_R/(\Delta\omega - i\Gamma_R)$. Since a conventional CARS signal is proportional to $|\chi_{NR} + \chi_R(\Delta\omega)|^2$, we can predict the frequency separation (max to min) to be

$$\Delta\bar{\nu} = \Gamma_R[(\chi_R/\chi_{NR})^2 + 4]^{1/2}$$

inverting, we find

$$\chi_R/\chi_{NR} = [(\Delta\bar{\nu}/\Gamma_R)^2 - 4]^{1/2}$$

$$\approx (\Delta\bar{\nu}/\Gamma_R)[1 - 2(\Delta\bar{\nu}/\Gamma_R)^{-2}] \tag{10}$$

where Γ_R is also measured in cm^{-1} the latter expression applying for $\Delta\bar{\nu}/\Gamma_R >> 1$). Thus the frequency separation explicitly determines the ratio of the susceptibilities. Since measurements of frequencies can be made quite accurate, this approach is a potentially precise method of finding χ_R/χ_{NR}.

LB have performed two measurements of $\Delta\bar{\nu}$ for samples of interest here: the first for a spectrum of 50% benzene and 50% carbon tetrachloride, the second for a spectrum of pure benzene. From the former we have a measure of $\chi_R(C_6H_6)/[\chi_{NR}(C_6H_6) + \chi_{NR}(CC\ell_4)]$ and from the latter just $\chi_R(C_6H_6)/\chi_{NR}(C_6H_6)$. In particular, $\Delta\bar{\nu} = 15.5\ cm^{-1}$ for the mixture and $27.5\ cm^{-1}$ for neat (pure) benzene. LB also give the Raman linewidth of the 992 cm^{-1} mode with more precision than that given in Fig. 7, $\Gamma_R = 1.15\ cm^{-1}$. Therefore we have,

$$\frac{\chi_R(C_6H_6)}{\chi_{NR}(C_6H_6) + \chi_{NR}(CC\ell_4)} = 13.3$$

$$\frac{\chi_R(C_6H_6)}{\chi_{NR}(C_6H_6)} = 23.8 \qquad (11)$$

From which we find $\chi_R(C_6H_6)/\chi_{NR}(CC\ell_4) = 30.1$.

Comparing the two values of $\chi_R(C_6H_6)/\chi_{NR}(CC\ell_4)$, 30.1 and 38., we see a large discrepancy — even more than the estimated 15% error which would lead to 38. ± 6. We must look elsewhere to find the reason for this significant difference.

Careful examination of the experimental spectra in Fig. 8 reveals an important new feature overlooked in our previous work.[3] Although

these spectra have the general forms associated with a Lorentzian lineshape, the linewidths do not match the expected width $\Gamma_R = 1.15$ cm^{-1}. In fact, the experimentally determined linewidth from the spectra of the 0.1% benzene solution is $\Gamma_R = 0.8$ cm^{-1} (HWHM). Such a reduction in Γ_R will strongly influence the peak magnitude of χ_R, which may be written as $\chi_R = A_R/\Gamma_R$ for a simple Lorentzian. In this case let us reexamine the determination of the ratio of the resonant susceptibility of pure (100%) benzene to the nonresonant susceptibility of pure carbon tetrachloride.

From Eqs. (6) and (8) we actually determine that the ratio $\chi_R(0.1\%C_6H_6)/\chi_{NR}(99.9\%CCl_4) = 0.038$, where we have explicitly included the concentration of each species. Since the 992 cm^{-1} mode has been well characterized as a Lorentzian,[12] we can write (at the peak)

$$\chi_R(0.1\%C_6H_6) = A_R(0.1\%C_6H_6)/\Gamma_R(0.1\%C_6H_6) \tag{12}$$

where $A_R(0.1\%C_6H_6)$ and $\Gamma_R(0.1\%C_6H_6)$ are the Raman amplitude and linewidth evaluated for a sample of 0.1% benzene. Normally we can assume that the Raman amplitude is linearly proportional to the density of benzene molecules and that the linewidth is independent of concentration, so that χ_R is also linearly dependent on concentration. In benzene, we still expect the usual dependence of the Raman amplitude:

$$A_R(0.1\%C_6H_6) = (0.1\%)A_R(100\%C_6H_6)$$

since, apart from the usual factor of the density, A_R contains only dipole matrix elements and nonresonant energy denominators which are

quantities dependent on the internal structure of the benzene molecule — not on the density of molecules. The Raman linewidth, on the other hand, is dependent upon both the internal structure of the molecule and the molecule's interaction with its enviroment. This latter effect can lead to a dependence of Γ_R upon the density through collision processes as we will see below. In benzene we have observed

$$\Gamma_R(0.1\%C_6H_6) = \left(\frac{0.8\ \mathrm{cm}^{-1}}{1.15\ \mathrm{cm}^{-1}}\right)\Gamma_R(100\%C_6H_6) = 0.70\ \Gamma_R(100\%C_6H_6)$$

Using these relationships between parameters measured at 0.1% and at 100% benzene, we can determine the value of $\chi_R(100\%C_6H_6)/\chi_{NR}(100\%CC\ell_4)$ in terms of the experimentally determined value of this ratio for 0.1% benzene given above (0.038). One has

$$\frac{\chi_R(100\%C_6H_6)}{\chi_{NR}(100\%CC\ell_4)} = \frac{A_R(100\%C_6H_6)/\Gamma_R(100\%C_6H_6)}{\chi_{NR}(100\%CC\ell_4)}$$

$$= \frac{[A_R(0.1\%C_6H_6)/10^{-3}]/[\Gamma_R(0.1\%C_6H_6)/0.70]}{\chi_{NR}(100\%CC\ell_4)}$$

$$= (7.0 \times 10^2)\ \chi_R(0.1\%C_6H_6)/\chi_{NR}(100\%CC\ell_4)$$

$$= 26. \qquad (13)$$

where the 0.1% difference between $\chi_{NR}(99.9\%CC\ell_4)$ and $\chi_{NR}(100\%CC\ell_4)$ is neglected.

Having made the correction we see that the value of the ratio has been substantially reduced and the agreement with LB is somewhat better. Of course, since we know the linewidth is concentration dependent, we require that the value of χ_R/χ_{NR} of LB similarly be corrected for the reduced linewidth which should have been present in their spectra of the 50% benzene solution. Unfortunately, there were no published plots[13] of the CARS spectra used to determine the ratio of susceptibilities, so the linewidth of the resonance at this concentration cannot be directly determined.

To estimate the Raman linewidth at 50% benzene concentration we refer to the work of Griffiths, et al.[15] who have examined this problem using spontaneous Raman scattering and who offer a pausible explanation of the effect. They point out that at high concentrations of benzene, there are a large number of collisions between benzene molecules during which it is energetically possible to undergo nonradiative transitions. The most favorable transition being an excitation of the nearby 983.5 cm^{-1} mode with the additional 8.7 cm^{-1} of energy going into kinetic energy. As the concentration is decreased, the number of collisions and nonradiative transfers decrease — leading to increased lifetime and decreased linewidth. Their data indicates a limiting linewidth of 0.75 cm^{-1}, which is in good agreement with our measured value of 0.8 cm^{-1}. Furthermore, the concentration dependence of the linewidth is fairly linear with a value of 0.95 cm^{-1} for a 50% solution of benzene.

Using this value of Γ_R, we can now correct the measured χ_R/χ_{NR} of LB. Again, their ratio was $\chi_R(50\%C_6H_6)/\chi_{NR}(CCl_4) = 30.1$ and after performing the corrections as in Eqs. (12) and (13), we find

$$\frac{\chi_R(100\%\ C_6H_6)}{\chi_{NR}(100\%\ CC\ell_4)} = 24.9 \tag{14}$$

Which is in excellent agreement with our value of 26. determined using the polarization-sensitive detection techniques. As a further indication of the quality of this measurement, we show in Fig. 9 computer generated plots of the expected ratio signal strength $I_{\parallel}/I_{\perp}$ vs. Stokes shift (assuming a Lorentzian resonance with $\Gamma_R = 0.8\ cm^{-1}$ and $\chi_R(0.1\%\ C_6H_6)/\chi_{NR}(CC\ell_4)=.038$). The computed lineshapes are also in good agreement with the experimental ones of Fig. 8.

To conclude the discussion of the work on the 992 cm^{-1} mode of benzene, we consider what the experimental limits of detection are. The analysis has shown that the ratio of χ_R/χ_{NR} is the important parameter determinable from the spectra. Since the magnitude of χ_R is a directly proportional to the number of resonant scatterers while χ_{NR} is due only to the solvent (for dilute solutions), the ratio χ_R/χ_{NR} is a direct measure of concentration of the resonant species. For 10^{-3} (by volume) C_6H_6 in $CC\ell_4$, we have found $\chi_R/\chi_{NR} \approx 3.8 \times 10^{-2}$. Consider now the signal to noise ratio, S/N, of Fig. 8(a) — the background suppression spectrum — roughly S/N ~ 10, in this case. However, since the spectrum is quadratic in the ratio of susceptibilities, we estimate a limiting (S/N = 1) value of χ_R/χ_{NR} to be $3.8 \times 10^{-2}/(10)^{\frac{1}{2}} \approx 1.2 \times 10^{-2}$ or a benzene concentration of 3×10^{-4}.

The advantage of heterodyning becomes clear by examining Fig. 8(b), which displays the imaginary part of χ_R. Here again S/N ~ 10, but this spectrum is linear in χ_R. Thus, the heterodyned spectra will have S/N ~ 1 for $\chi_R/\ \chi_{NR} = 3.8 \times 10^{-3}$ or a benzene concentration of 10^{-4}. This

concentration would correspond to 100 ppm of benzene in carbon tetrachloride and is approximately two order of magnitude better than the detection sensitivity of the conventional CARS technique.

D. Applications and Limitations of Polarization-Sensitive CARS Techniques

1. Applications

There are several interesting applications of these new techniques which are discussed below. First, though, we will briefly summarize the two applications emphasized in the experimental section — namely, the measurement of relative susceptibilities and the detection of weak concentrations.

As demonstrated in part C, making a measurement of the relative signal strength of the transmitted and rejected signals (as suggested in Fig. 6), is in effect making a measurement of χ_R/χ_{NR}. In the present work we have only studied benzene diluted in carbon tetrachloride, but this is not an isolated example. Using other liquids with Raman modes (either strong or weak), we can measure the ratio of their resonant susceptibility to $\chi_{NR}(CC\ell_4)$ and so have a *relative measurement of the* resonant susceptibilities. Similarly, different solvents may be used with benzene to establish their relative nonresonant susceptibilities.

This technique is superior to that proposed by Levenson[14] and used in the above determination of $\chi_R(C_6H_6)/\chi_{NR}(CC\ell_4)$ by Levenson and Bloembergen.[13] Although it is true that their technique involves only measuring the ratio of $\Delta\bar{\nu}/\Gamma_R$ (the frequency splitting of the maximum and minimum of the CARS signal over the Raman linewidth - HWHM), the dependence of χ_R/χ_{NR} on $\Delta\bar{\nu}/\Gamma_R$ for a particular concentration can only be de-

termined by assuming that the resonance has a particular lineshape. On the other hand, the polarization-sensitive technique presented here does not rely on the lineshape of the resonance but only requires information about the angle between $\vec{\mathcal{E}}_R$ and $\vec{\mathcal{E}}_{NR}$ which can be found experimentally, if necessary.

At the end of the last section we established that the detection limit of our apparatus was 100 ppm of benzene in $CC\ell_4$ or $\chi_R/\chi_{NR} \approx 4 \times 10^{-4}$. It is this latter number which should be emphasized. Consider, as an illustration, an experiment involving the detection of low concentrations of hydrogen in a nitrogen atmosphere, such as exists in a methane flame.[16] It is known that the Q_1 Raman mode of H_2 at STP has a resonant susceptibility approximately 4×10^5 stronger than the nonresonant susceptibility of nitrogen at STP. Using the polarization-sensitive CARS techniques, the expected detection limit would be $\chi_R(H_2)/\chi_{NR}(N_2) = 4 \times 10^{-3}$, the same as before. In this illustration, however, the large strength of the resonance implies a minimum detectable concentration of $4 \times 10^{-3}/4 \times 10^5$ or 10 ppb H_2 in N_2. Previous measurements using amplitude-CARS were limited to 1-10 ppm.[16]

Another application of the polarization-sensitive detection schemes was briefly discussed in Section IIC. The situation considered was a weak resonance in the wing of a stronger resonance. It was described how the polarization analyzer could be adjusted to null both the strong resonance and the nonresonant background fields over a limited spectral range. This allowed the weak mode to be more readily observable. We have been able to experimentally demonstrate this application using the Raman modes of benzene listed in Fig. 7. An approximate null of the background and the strong 992.2 cm^{-1} mode was obtained near 975 cm^{-1}

(Raman modes appear at 983.5 and 979.3 cm^{-1}), then the polarizer was slightly uncrossed (by 2°) to allow for some heterodyning of the weak resonance. The resulting spectrum is shown in Fig. 10. The upper spectrum is the usual amplitude-CARS spectrum of the 4% C_6H_6 in CCl_4, showing the weak Raman mode at 983.5 cm^{-1} on the shoulder of the stronger 992.2 cm^{-1} mode. The lower spectrum (using the polarization analyzer) shows much more clearly the 983.5 cm^{-1}, even the measured width of 0.7 cm^{-1} is in agreement with Lynch and Lotem.[12] It is also apparent in Fig. 10(b) that the weaker mode at 979.3 cm^{-1} is now observable, whereas it was lost in the noise of the amplitude-CARS spectrum. Of course, the polarization analysis of this form is useful only over a limited spectral range, thus no attempt was made to examine the weak resonances on the high frequency side of 992 cm^{-1}. This would require a different polarization adjustment.

Finally, as a word of caution, there will always be some amount of distortion of the weak signal lineshape as we scan across the weak-resonance frequency. This is due to the slow variation with frequency of the nonlinear output field associated with the strong Raman mode located many linewidths away. Since the polarization analyzer is fixed during the scan, varying amounts of this strong-resonance field will pass through the analyzer and be detected along with the rapidly changing field due to the weak-resonance under examination.

Yet another application of these techniques is to separate Raman modes of different symmetries. The basic idea here is to set the polarization analyzer to purposely discriminate against Raman modes for a particular symmetry. Levenson and Bloembergen[13] first did this when they presented a CARS spectrum of benzene with the analyzer set ortho-

gonal to the resonant field, e.g. along $\hat{y}$ in Fig. 3. In their case, only the nonresonant signal remained. A much more interesting situation has been recently presented by Rahn et al.[17] in which it is pointed out that the degenerate vibrational and rotational transitions in gases have a different symmetry from the symmetric Q-branch modes. (The former are anisotropic, $\rho_R = 3/4$, while the latter are isotropic, $\rho_R = 0$.) It was then possible to produce spectra showing Q-branch modes but not rotational modes and vice-versa. Discrimination such as this can be quite useful in spectroscopic studies.

In related work, Koroteev et al.[18] have used polarization-sensitive CARS to study the broad, featureless Raman mode of water from 3200 cm^{-1} to 3600 cm^{-1}. Making a series of spectra with differing polarization arrangements, they have been able to partially resolve several lines of different symmetries within this band. They also point out techniques which can be used to separate closely spaced modes with differing depolarization ratios. Thus, polarization-sensitive detection has many possible uses, especially in the area of nonlinear spectroscopy.

2. Limitations

In this segment, we discuss the limitations of polarization-sensitive CARS, i.e., the factors which can improve and/or degrade the useage of these techniques. We begin by considering possible improvements in the previously described experimental setup.

Two features of the apparatus used in the demonstration of BS- and OHD-CARS which can be improved are: the polarization optics and the data acquisition system. The importance of quality polarization components cannot be overly emphasized, since these techniques rely on the electric

fields being in nearly pure polarization states. With the simple setup used in the background suppression case (Fig. 4) it was possible to achieve an extinction ratio (for the nonlinear signal) of about 2-5 × 10^{-5}, but with higher quality components it should be possible to obtain an extinction of a few times 10^{-6}. (This limit being due primarily to scattering from the surfaces of the analyzer.) This would lead to about one order of magnitude improvement in the detection sensitivity, when using the heterodyning techniques.

Further increase in the signal to noise ratio would occur if the data acquisition system were modified to a shot-to-shot, digital data processing system. Such a system would perform the ratio of $I_{\parallel}$ to $I_{\perp}$ after each shot, then evaluate the average ratio of some specified number of shots. The present system[7] instead performs an exponential average of each input channel over a specified time constant, then outputs the analog ratio of the averaged signals. This type of system leads to an unequal weighting of the pulses coming in during the time constant and thus has additional electronic noise. The actual improvement in the CARS signal to noise ratio to be expected by the use of the proposed data processing system may be a factor of four or more. With these two changes, the expected minimum detectable ratio of resonant to nonresonant susceptibility would be reduced from 4 × 10^{-3} to 2 × 10^{-4}. Any larger decrease in this ratio would be experimentally very difficult. Thus, we may claim that the practical detection sensitivity of these polarization-sensitive forms of CARS is

$$\chi_R/\chi_{NR} \approx 2 \times 10^{-4} \text{ (practical limit, } \rho_R = 0)$$

which for benzene implies a concentration of about 5 ppm or for hydrogen about 1 ppb.

At this point, we must also indicate that there are factors which will cause a loss of sensitivity and, in effect, raise the practical limit proposed above. One source of this degradation is noise in the CARS spectrum which may make the small signals of the weak resonances difficult to observe. As described in Section IIE, laser intensity fluctuations are one source of noise in a spectrum without normalization, and electronic noise in the detection system plays a similar role for intensity normalized spectra. Quantum fluctuations in the photon field, i.e., shot noise, can also be an important noise source in measurements involving small numbers of photons. To formalize the signal to noise considerations, we draw on the analysis given in Section II. In particular, Eq. (62) of that section gives the limiting value of χ_R/χ_{NR} in terms of θ_e^2, the finite extinction ratio of the polarization analyzer, and ε_a and ε_c, the fractional mean square intensity fluctuations on the input beams at ω_a and ω_c. For the case of OHD-CARS we have

$$(\chi_R/\chi_{NR})_{min} \approx \sqrt{2}\,\theta_e(4\varepsilon_a + \varepsilon_c)^{\frac{1}{2}} \tag{15}$$

applying in the limit that fluctuations are dominant over shot noise. Assuming $\varepsilon_a = \varepsilon_c = (0.15)^2$ (15% rms laser intensity fluctuations), and $\theta_e^2 = 10^{-4}$, we found that averaging with a one second time constant gave a limiting value of $\chi_R/\chi_{NR} \sim 2 \times 10^{-3}$ for the detection sensitivity, which compares reasonably well with the experimentally determined value of $\sim 4 \times 10^{-3}$ determined above.

For the present discussion we want to generalize Eq. (15) to in-

clude the shot noise contribution. This can be easily done starting from Eq. (59) of Section II as before, but keeping the extra term describing the shot noise. The resulting expression is

$$(\chi_R/\chi_{NR})_{min} \approx \sqrt{2}\ \theta_e[\varepsilon + 1/N_P']^{\frac{1}{2}}\mathcal{N}^{-\frac{1}{2}} \tag{16}$$

where N_P' is the product of N_p, the number of photons incident on the detector through the analyzer, and q, the detector's quantum efficiency (i.e., N_P' is the number of photoelectrons produced at the photocathode). Here we have written ε for either the total fluctuations due to the laser intensities $(4\varepsilon_a + \varepsilon_c)$ when no intensity normalization is used or for $\varepsilon_{electronic}$ when intensity normalization is included. Also in Eq. (16), the increased sensitivity derived from averaging over $\mathcal{N}$ measurements of the same signal is explicitly shown.

Several features of Eq. (16) are important for the determination of the limiting value of χ_R/χ_{NR}. As indicated previously, using a better analyzer (reducing θ_e) or less fluctuating laser sources (reducing ε) help to decrease $(\chi_R/\chi_{NR})_{min}$. However, upon reducing ε, the shot noise term $(N_P')^{-1}$ becomes increasingly important. In particular, consider the case of an ideal laser system which has no shot-to-shot power fluctuations, i.e., $\varepsilon = 0$ (or an ideal data acquisition system if normalization is used). We can then show that the minimum detectable value of χ_R is determined — independent of χ_{NR} (as shown at the end of Section IIE). Bascially, we have for $\varepsilon = 0$

$$(\chi_R/\chi_{NR})_{min} \propto \theta_e N_P^{-\frac{1}{2}} \propto \theta_e(\theta_e^2\chi_{NR}^2)^{-\frac{1}{2}}$$

where the latter proportionality uses the fact that N_P (the number of photons after the analyzer) is determined predominantly by the leakage of the nonresonant signal through the analyzer, so N_P is proportional to the extinction ratio times the nonresonant signal (which goes as χ_{NR}^2), or $\theta_e^2\chi_{NR}^2$. Rewriting the above, we see that

$$(\chi_R/\chi_{NR})_{min} \propto \chi_{NR}^{-1}$$

so, in this limit, the value of $(\chi_R)_{min}$ is actually determined, not the ratio of resonant to nonresonant susceptibilities. In other terms, the limiting detectable value of χ_R is determined only by the shot noise fluctuations of the leakage signal through the analyzer — the smaller N_P, the larger $(\chi_R)_{min}$ becomes.

Although the ideal case of no laser or electronic noise ($\epsilon = 0$) is not attainable in practice, we can encounter the same problem, if $(N_P')^{-1} \gg \epsilon$. This can happen if we are in a situation with weak signals. To avoid this limitation of the detection sensitivity, it is advisable to use higher-powered laser systems to ensure that $(N_P')^{-1}$ not dominate the fluctuation (ϵ) term. Even though we have discussed the effect of shot noise for the case of OHD-CARS, the conclusion of this analysis applies equally well to both background suppression- and amplitude-CARS. In all cases, we have maximum detection sensitivity by increasing the nonlinear signal strength until $\epsilon > (N_P')^{-1}$.

For the present system (without normalization) $\epsilon \approx .1$ so we require $N_P' \gtrsim 10$. With a typical quantum efficiency of 10%, we need at least 100 photons after the analyzer (or 10^6-10^7 photons in the signal after the sample). One often overlooked advantage of this form of nonlinear spec-

troscopy is that the nonlinear nature of the process can be used to ensure that the shot noise contribution to χ_R/χ_{NR} is minimized. (Of course, when such high powered lasers are used, other nonlinear effects, such as ellipse rotation or self-focusing, may become important.) On the other hand, if the number of photons does decrease into the shot noise regime, we can further improve the detection sensitivity only by averaging over many shots — the same technique used in linear spectroscopy.

Also, it should be realized that the practical limiting value of χ_R/χ_{NR} depends upon the symmetry of the Raman mode, i.e. upon the depolarization ratio, ρ_R. In fact, using the formalism defined in Section II, we can include this dependence by the inclusion of a simple multiplicative factor. In general,

$$\chi_R/\chi_{NR} = (2 \times 10^{-4})/|3\rho_R - 1| \quad \text{(practical limit)}$$

where we have assumed Kleinman's symmetry ($\rho_{NR} = 1/3$). We note that as the depolarization ratio approaches 1/3 the sensitivity decreases rapidly ($\chi_R/\chi_{NR} \to \infty$), but this is to be expected since $\vec{\mathcal{E}}_R$ becomes more nearly parallel to $\vec{\mathcal{E}}_{NR}$ (making polarization separation increasingly difficult). Fortunately, there is very little difference in the limit for an isotropic mode with $\rho_R = 0$ and an anisotropic mode with $\rho_R = 3/4$ (see Ref. 17).

Finally, the detection sensitivity may also depend upon the quality of the sample. Although a general elliptical birefringence in the sample, e.g. optical activity in certain liquids or crystalline anisotropy in solids, complicates the interpretation of the nonlinear output

field, it does not destroy the purity of the output polarization state. (The presence of such birefringence may preclude the possibility of phasematching, however.) If there is an inhomogeneity in this birefringence, such as from macroscopic strains in solids, the output field will leave the sample in a nonuniform polarization state. It will then be impossible to null the output over the entire beam profile, i.e. there will be poor extinction and, consequently, poor detection sensitivity.

In summary, this section has described the techniques and apparatus used in making polarization-sensitive CARS measurements. Two new techniques — background suppression- and optical heterodyned detection -CARS — have been experimentally demonstrated using the 992 cm^{-1} Raman mode of benzene diluted in carbon tetrachloride, and the ratio of resonant to nonresonant susceptibilities has been measured and compared to other work. We have estimated the minimum detectable concentration of benzene observable with this apparatus and suggested what the practical limit might be. We also indicate the limitations of these techniques and possible interesting applications.

References

1. Historical note: The first use of the four-wave mixing process, $\omega=2\omega_a-\omega_c$, to observe a Raman resonance was F. DeMartini, G. P. Giuliani, and E. Santamato, Opt. Commun. 5, 126 (1972). The acronym "CARS" was first used by R. F. Begley, A. B. Harvey, and R. L. Byer, Appl. Phys. Lett. 25, 387 (1974).
2. For a recent review of current work in amplitude-CARS, see J. W. Nibler and G. V. Knighten, "Coherent Anti-Stokes Raman Spectroscopy" in Raman Spectroscopy of Gases and Liquids, ed. A. Weber (Springer-Verlag, New York, 1979).
3. J.-L. Oudar, R. W. Smith, and Y. R. Shen, Appl. Phys. Lett. 34, 758 (1979).
4. S. Chu and R. W. Smith, Opt. Commun. 28, 221 (1979).
5. Interference filters (having peak transmissions of >90% and transmission widths of about 30Å) and etalons (having reflectivities of about 80% and thicknesses of 0.15 mm) were purchased from Lambda Physik (West Germany). See also Ref. 4.
6. R. Wallenstein and T.W. Hänsch, Appl. Opt. 13, 1625 (1974). In this case the telescope with ×10 beam expansion was purchased from Oriel Corp. and the grating (50 mm square with a 61°10' blaze angle and 625 grooves/mm) was purchased from Bausch-Lomb.
7. H. Rosen and P. Robrish, Rev. Sci. Instrum. 46, 1115 (1975).
8. This follows since, in general for an isotropic medium, we have $[\chi_R]_{1111}=[\chi_R]_{1122}+[\chi_R]_{1212}+[\chi_R]_{1221}$ and for the CARS process we have $[\chi_R]_{1122}=[\chi_R]_{1212}$. Thus there are only two independent el-

ements of the CARS susceptibility in an isotropic medium.

9. Tensor properties for different spatial symmetries are tabulated in Nonlinear Optical Phenomena by P. N. Butcher (Ohio State, Columbus, 1965).

10. M. D. Levenson and N. Bloembergen, Phys. Rev. B10, 4447 (1974).

11. See, for example, Raman Spectroscopy of Gases and Liquids, ed. A. Weber (Springer-Verlag, New York, 1979) and the references therein.

12. See, for example, R. T. Lynch, Jr. and H. Lotem, J. Chem. Phys. 66, 1905 (1977); H. Lotem, R. T. Lynch, Jr. and N. Bloembergen, Phys. Rev. A14, 1748 (1976); A. Owyoung and P. S. Peercy, J. Appl. Phys. 48, 674 (1977).

13. M. D. Levenson and N. Bloembergen, J. Chem Phys. 60, 1323 (1974).

14. M. D. Levenson, IEEE J. Quant. Electron. QE-10, 110 (1974).

15. J. E. Griffiths, M. Clerc, and P. M. Rentzepis, J. Chem. Phys. 60, 3824 (1974).

16. See, for example, P. R. Regnier and J. P. E. Taran, Appl. Phys. Lett. 23, 240 (1973).

17. L. A. Rahn, L. J. Zych, and P. L. Mattern, Opt. Commun. 30, 249 (1979).

18. N. I. Koroteev, M. Endemann, and R. L. Byer, Phys. Rev. Lett. 43, 398 (1979).

19. Y. R. Shen, Rev. Mod. Phys. 48, 1 (1976) and the references therein.

Figure Captions

Fig. 1 Standard phasematching geometry in normally dispersive media. The angle ψ between the two input wavevectors, $\vec{k}_a$ and $\vec{k}_c$, is greatly exaggerated; typically $\psi \approx 1\text{-}2^\circ$. Note ψ is determined in the medium of refractive index n.

Fig. 2 Amplitude-CARS setup used in the laboratory. Half-wave plate W1 and polarizer P1 allow rotation of ω_a polarization; P2 defines polarization of ω_c. Fixed mirror M1, translatable mirror M2, and lens L1 determine the phasematching angle. S - sample, DM - double monochromator. Insert shows positioning of M2 for alignment of detection system.

Fig. 3 Unit vectors showing directions of the input fields $\hat{\mathcal{E}}_a$ and $\hat{\mathcal{E}}_c$ and the resonant and nonresonant output $\hat{\mathcal{E}}_R$ and $\hat{\mathcal{E}}_{NR}$, respectively. A strongly polarized Raman mode and Kleinman's symmetry are assumed. $\delta = 71.5^\circ$, $\alpha = 45^\circ$.

Fig. 4 Basic polarization-sensitive CARS setup used for background suppression and heterodyning, showing the alterations in the detection system. Compare with Fig. 2.

Fig. 5 Polarization arrangements used in OHD-CARS. (a) To display the spectrum of $\mathrm{Re}(\chi_R)$, (b) to display the spectrum of $\mathrm{Im}(\chi_R)$. $\hat{\zeta}$ - transmission axis of linear analyzer, $\hat{\eta}$ - fast axis of quarter-wave plate.

Fig. 6 Possible detection systems for normalized polarization-sensitive detection. (a) Setup actually used, with fixed Glan-Thompson analyzer after the monochromator and separate PMTs. (b) Proposed setup with Glan-Thompson before monochromator,

with separated beams going in at different slit heights.

Fig. 7 Table of Raman parameter for benzene near 992 cm^{-1}. ω_R - central frequency, A_R - strength, Γ_R - linewidth (HWHM), and $(\chi_R)_{max}$ - maximum resonant susceptibility (A_R/Γ_R) for each Raman mode.

Fig. 8 Experimental spectra of 992 cm^{-1} mode of 0.1% benzene in carbon tetrachloride (a) using background suppression-CARS, (b) and (c) using different arrangements of optical heterodyned detection-CARS. The vertical scale - relative signal strength $I_{\parallel}/I_{\perp}$, the horizontal scale - Stokes shift in cm^{-1}.

Fig. 9 Theoretical plot of polarization-sensitive CARS spectra in Fig. 8. We assume Lorentzian lineshape with $\Gamma_R = 0.8$ cm^{-1} and $\chi_R(0.1\%\ C_6H_6)/\chi_{NR}(CC\ell_4) = 3.8 \times 10^{-2}$. Compare with Fig. 8.

Fig. 10 CARS spectra of 4% benzene in carbon tetrachloride in the vicinity of 980 cm^{-1}. (a) Unpolarized detection, (b) transmitted signal through a quarter-wave plate and a slightly uncrossed polarizer — arbitrary scale between (a) and (b).

Figure 1

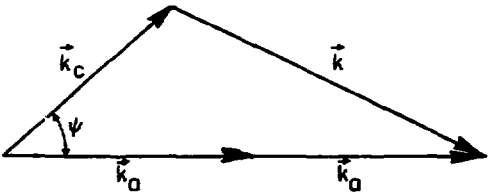

$$\sin^2(\psi/2) = \frac{(k - k_c + 2k_a)(k + k_c - 2k_a)}{8\,k_a\,k_c}$$

$$\psi \approx \left[\frac{2}{n\omega_a}\left(\frac{\partial n}{\partial \omega}\right)\right]^{1/2} \omega_R$$

XBL 807-5534

Figure 2

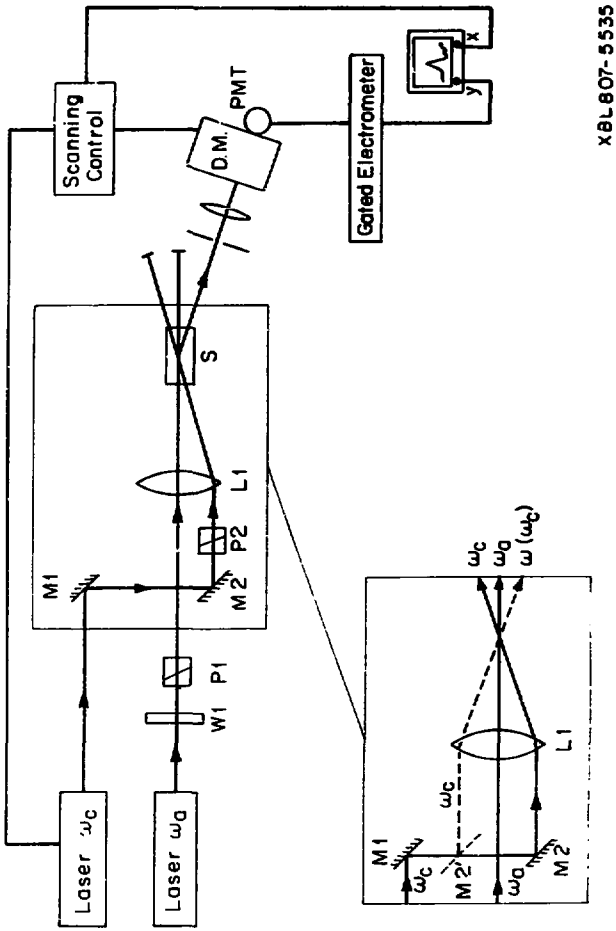
Scanning Control
PMT
D.M.
Gated Electrometer
x
y
S
L1
P2
M1
M2
P1
W1
Laser ω_c
Laser ω_a
ω_c
ω_a
$\omega(\omega_c)$
L1
M1
M2'
M2
ω_c
ω_a
XBL807-5535

Figure 3

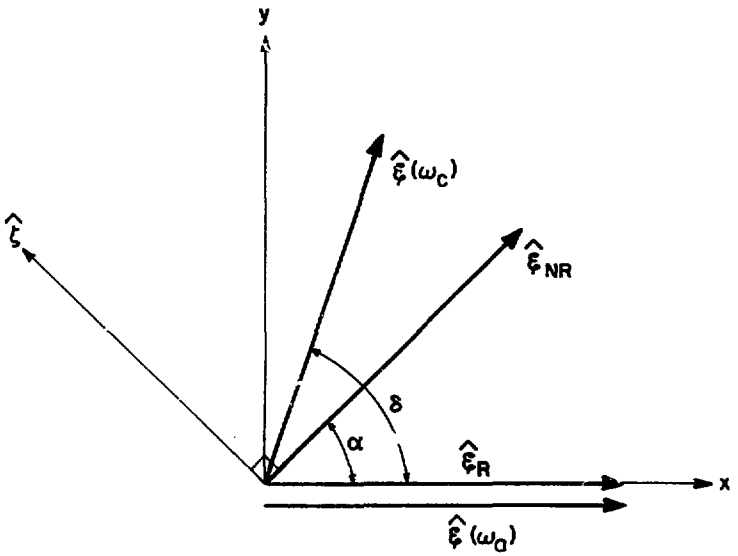

XBL807-5536

Figure 4

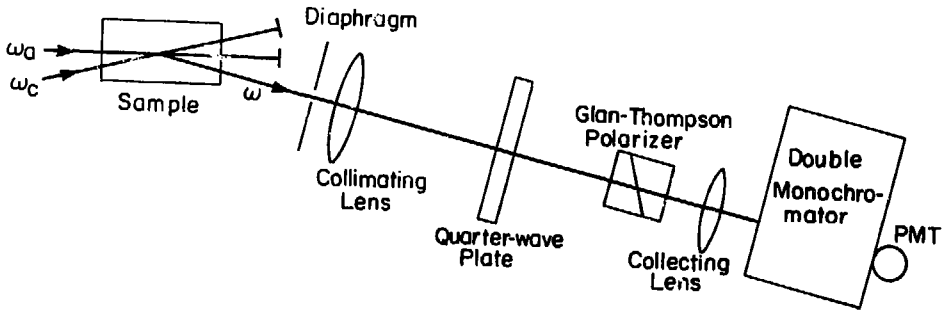

XBL807-5537

Figure 5

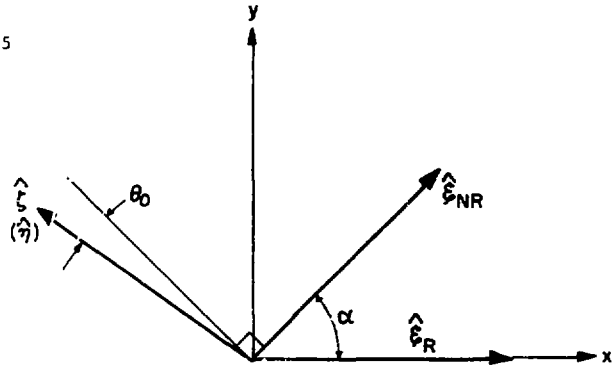

(a)

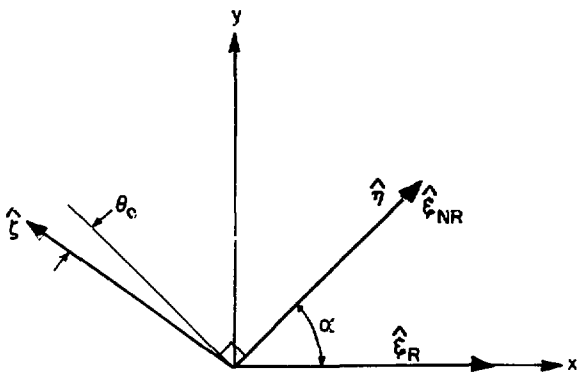

(b)

XBL 807-5538

Figure 6

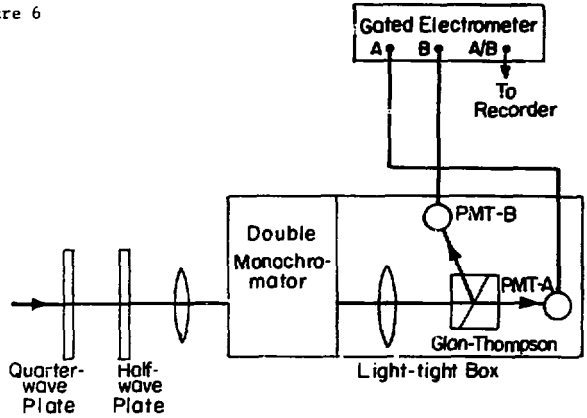

(a)

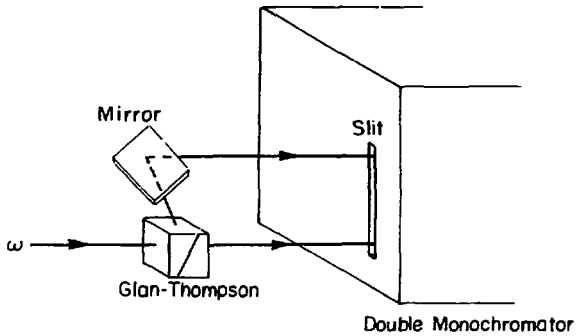

(b)

XBL 807-5539

Figure 7

Raman Parameters of Benzene[a]

ω_R (cm^{-1})	A_R (esu - cm^{-1})	Γ_R (cm^{-1})	$(\chi_R)_{max}$ (esu)
979.3	1.47	2.0	0.74
983.5	1.46	0.7	2.1
992.2	35.84	1.2	30.
998.4	1.92	1.5	1.2
1006.4	0.29	0.8	0.36

[a] From R. T. Lynch, Jr. and H. Lotem, J. Chem. Phys. 66, 1905 (1977).

Figure 8

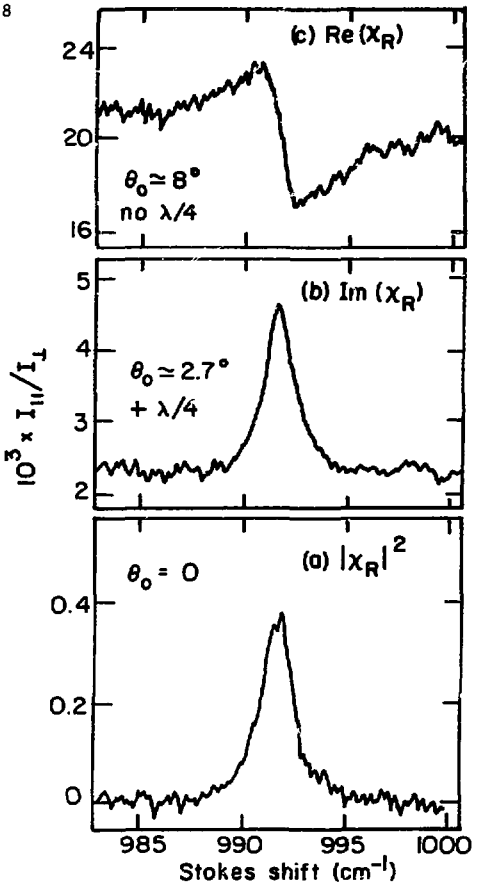

XBL807-5540

Figure 9

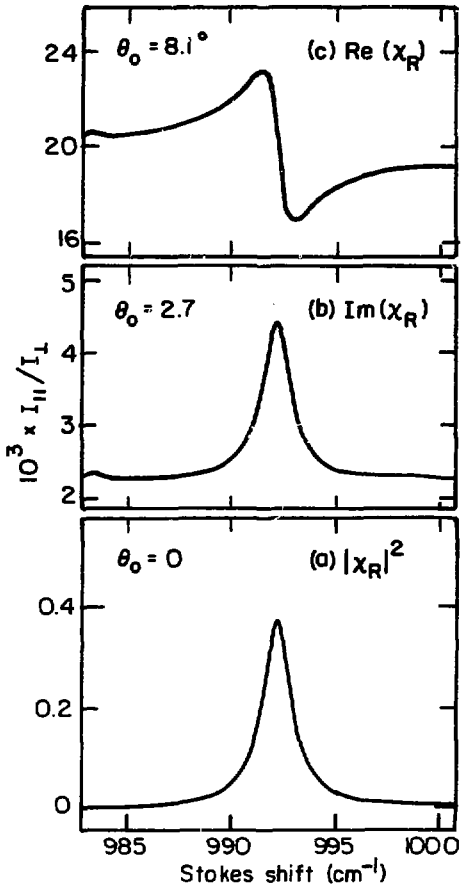

XBL 807-5541

Figure 10

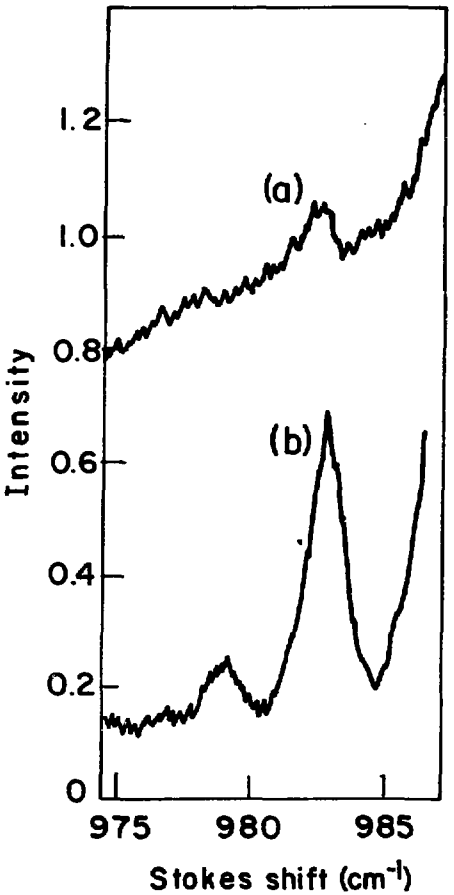

XBL 791-5630

IV. MULTI-RESONANT FOUR-WAVE MIXING IN INHOMOGENEOUSLY BROADENED MEDIA — THEORY

In Sections II and III we have discussed one method to study two-photon transitions and to improve the detectivity of these single resonances using polarization-sensitive detection. We now consider another form of four-wave mixing spectroscopy which uses double or triple resonances to yield additional spectroscopic information and also improve detection sensitivity.[1] As each additional resonance is approached the strength of the resonant susceptibility increases dramatically, as has been recently demonstrated experimentally.[2] It has also been recently shown by Druet, et al.[3] that it is possible to obtain Doppler-free spectra with multi-resonant four-wave mixing.

In this section, we give a more complete discussion of doubly and triply resonant processes along the lines of Oudar and Shen.[4] We begin by deriving the forms of particular multi-resonant nonlinear susceptibilities for processes such as CARS, CSRS and RIKES (see Section II for a description of these mixing processes). Of interest here is the nonlinear response of a medium showing inhomogeneous broadening, thus explicit expressions are derived to characterize this situation. We will see that the singly-resonant susceptibility is always dominated by the inhomogeneous broadening, while in some cases double and triple resonances show considerable narrowing. The measured strength of χ_R can be used to determine matrix elements involved in the process. The discussion here centers on studies of rare-earth ions in solids, but the Doppler broadened case is also included. Since real absorption can occur in multi-resonant processes, the nonlinear susceptibilities involve not

only the transverse (off-diagonal) damping terms, but also longitudinal (diagonal) damping. The effects of this linear absorption upon the nonlinear output are also considered. (The following section contains experimental work performed on $Pr^{+3}:LaF_3$.)

A. Multi-Resonant Nonlinear Susceptibilities

As pointed out in Section II, the density matrix formalism can be used to find $\overleftrightarrow{\chi}^{(3)}$ when the radiation fields are treated as a perturbation.[5] In general, there will be 48 terms in the third-order nonlinear susceptibility. Recently, a diagrammatic technique has been utilized in nonlinear calculations (Yee and Gustafson[6]) which allows one to easily write out all terms in $\overleftrightarrow{\chi}^{(3)}$. The following discussion makes use of this technique without further explanation.

We are specifically interested in terms of the nonlinear susceptibility which show double or triple resonances. The damping terms included in the resonance denominators then take on great importance. The relaxation of off-diagonal elements of the density matrix is written as[7]

$$\left(\frac{\partial \rho_{nn'}}{\partial t}\right)_{\text{damping}} = -\Gamma_{nn'}\rho_{nn'} \tag{1}$$

where $\Gamma_{nn'}$ is the phenomenological damping constant with $\Gamma_{n'n} = \Gamma_{nn'}$. The transverse relaxation time $(T_2)_{nn'} = (\Gamma_{nn'})^{-1}$ describes the dephasing of transitions between $|n\rangle$ and $|n'\rangle$. The damping of on-diagonal elements of the density matrix is given by

$$\left(\frac{\partial \rho_{nn}}{\partial t}\right)_{\text{damping}} = \sum_{n''} W_{nn''}(\rho_{n''n''} - \rho^{(0)}_{n''n''}) - \sum_{n'} W_{n'n}(\rho_{nn} - \rho^{(0)}_{nn}) \tag{2}$$

where $W_{nn''}$ is the transition probability of going from state $|n''\rangle$ to state $|n\rangle$ and $\rho^{(0)}_{n''n''}$ is the equilibrium population of state $|n''\rangle$. In a simple two level system there is only one time, $(T_1)_n = (W_{n'n})^{-1}$, which describes the decay of the population. However, in more complicated systems, one cannot use the concept of a longitudinal relaxation time, T_1, unless simplifying assumptions are made. If we assume there is no pumping into the state $|n\rangle$ from the decay of higher levels, the first sum on the right side of Eq. (2) can be neglected, leaving an effective damping constant Γ_{nn} given by $\sum_{n'} W_{n'n}$. We then have

$$\left(\frac{\partial \rho_{nn}}{\partial t}\right)_{\text{damping}} = - \Gamma_{nn}(\rho_{nn} - \rho^{(0)}_{nn}). \tag{3}$$

In our derivation of nonlinear susceptibilities, we assume that the damping is adequately described by the terms $\Gamma_{nn'}$ and Γ_{nn}.

We consider four particular examples of multi-resonant four-wave mixing of interest for our experimental studies. In each example, we assume that only two input frequencies, ω_1 and ω_2, are involved. Furthermore, the material system is assumed to be initially in its ground state $|g\rangle$. A Raman-type, low-lying level is designated $|g'\rangle$, while excited states are $|n\rangle$ and $|n'\rangle$.

1. Doubly-Resonant Processes

The doubly-resonant processes of interest have a single-photon resonance and a two-photon resonance. The first example is double resonance CARS which involves ω_1 being resonant with the transition $|g\rangle \rightarrow |n\rangle$ while $\omega_1 - \omega_2$ is resonant with $|g\rangle \rightarrow |g'\rangle$, as shown in Fig. 1(a). From the diagrams[6] we find

$$[\chi_R^{(3)}(\omega_3=\omega_1-\omega_2+\omega_1)]_{ijk\ell} = -\frac{N(\alpha_{gg'})_{ij}(\mu_{g'n})_k(\mu_{ng})_\ell \rho_{gg}^{(0)}}{\hbar^2(\omega_1-\omega_{ng}+i\Gamma_{ng})(\omega_1-\omega_2-\omega_{g'g}+i\Gamma_{g'g})} \tag{4}$$

with

$$(\alpha_{gg'})_{ij} \equiv \frac{1}{\hbar}\sum_m \left[\frac{(\mu_{gm})_i(\mu_{mg'})_j}{(2\omega_1-\omega_2-\omega_{mg})} + \frac{(\mu_{gm})_j(\mu_{mg'})_i}{(2\omega_1-\omega_2+\omega_{mg'})}\right]$$

$$+ \text{ terms with } j \text{ and } \ell \text{ interchanged}$$

where we have used $\vec{\mu} = -e\vec{r}$ for the dipole moment and have defined the Raman polarizability $\overleftrightarrow{\alpha}_{gg'}$. Damping terms are shown explicitly only in resonant denominators. Only transverse damping factors are necessary since the CARS process cannot result in any population changes. This is the familiar form of resonant CARS[2] that is analogous to resonant Raman scattering. The lineshape of this process in homogeneously broadened media is discussed by Bloembergen et al.[5].

Another type of CARS has the Raman resonance replaced by an upper state resonance[5] as depicted in Fig. 1(b). The frequency difference $\omega_1 - \omega_2$ is equal to the splitting between states $|n\rangle$ and $|n'\rangle$. The most strongly resonant terms of this susceptibility are[4]

$$[\chi_R^{(3)}(\omega_3=\omega_1-\omega_2+\omega_1)]_{ijk\ell} = -\frac{N(\alpha_{nn'})_i(\mu_{n'g})_j(\mu_{gn})_k\rho_{gg}^{(0)}}{\hbar^2(\omega_1-\omega_2-\omega_{n'n}+i\Gamma_{n'n})}$$

$$\times\left[\frac{1}{(\omega_1-\omega_{n'g}+i\Gamma_{n'g})} - \frac{1}{(\omega_2-\omega_{ng}-i\Gamma_{ng})}\right]$$

$$+ \text{ terms with } j \text{ and } \ell \text{ interchanged} \tag{5}$$

with

$$(\alpha_{nn'})_{i\ell} \equiv \frac{1}{\hbar}\sum_m \frac{(\mu_{mn'})_i(\mu_{nm})_\ell}{(2\omega_1 - \omega_2 - \omega_{n'm})} .$$

Although the frequencies $\omega_3 = 2\omega_1 - \omega_2$ and $\omega_1 - \omega_2$ appear in the resonant denominators, this process requires both ω_1 and ω_2 to be tuned to one-photon absorption transitions. The lineshape of the output must then be corrected for the effects of these absorptions in both input field strengths (see Section IVC).

CSRS (Coherent Stokes Raman Spectroscopy) is a technique very similar to CARS, except its output is at the frequency $\omega_4 = 2\omega_2 - \omega_1$ (as discussed in Section II). We consider a two-photon Raman resonance as before, while ω_4 is resonant between the excited state $|n\rangle$ and the Raman level $|g'\rangle$ (Fig. 1(c)). The resonant susceptibility is

$$[\chi_R^{(3)}(\omega_4 = \omega_2 - \omega_1 + \omega_2)]_{ijk\ell} = -\frac{N(\alpha_{gg'})_{k\ell}(\mu_{g'n})_i(\mu_{ng})_j\rho_{gg}^{(0)}}{\hbar^2(\omega_4 - \omega_{ng'} + i\Gamma_{ng'})(\omega_1 - \omega_2 - \omega_{g'g} - i\Gamma_{g'g})}$$

$$+ \text{ terms with } j \text{ and } \ell \text{ interchanged} \qquad (6)$$

with

$$(\alpha_{gg'})_{k\ell} \equiv \frac{1}{\hbar}\sum_m \left[\frac{(\mu_{gm})_k(\mu_{mg'})_\ell}{(\omega_1 - \omega_{mg})} - \frac{(\mu_{gm})_\ell(\mu_{mg'})_k}{(\omega_2 + \omega_{mg})}\right].$$

As we will show below, this process and the upper state resonance CARS process have a feature which distinguishes them from other forms of resonant CARS or CSRS. Even though we have examined only three doubly-resonant possibilities, all other cases are easily managed with the

diagrammatic technique.[4]

2. Triply-Resonant Processes

We now consider what happens when all three denominators approach resonances. As before, we consider the case of only two independent input frequencies, $\omega_1 > \omega_2$. The process of interest here is a RIKES-type process involving $\omega_2 = \omega_1 - \omega_1 + \omega_2$, thus only a three level system need be considered (as shown in fig. 2). The three principal diagrams yield

$$[\chi_R^{(3)}(\omega_2 = \omega_1 - \omega_1 + \omega_2)]_{ijk\ell} = -\frac{N(\mu_{g'n'})_i(\mu_{n'g})_j(\mu_{gn'})_k(\mu_{n'g'})_\ell \rho_{gg}^{(0)}}{\hbar^3(\omega_2 - \omega_{n'g'} + i\Gamma_{n'g'})}$$

$$\times \left[\frac{1}{(\omega_1 - \omega_{n'g} - i\Gamma_{n'g})(\omega_1 - \omega_2 - \omega_{g'g} - i\Gamma_{g'g})}\right.$$

$$+ \frac{1}{(i\Gamma_{n'n'})(\omega_1 - \omega_{n'g} + i\Gamma_{n'g})}$$

$$\left. - \frac{1}{(i\Gamma_{n'n'})(\omega_1 - \omega_{n'g} - i\Gamma_{n'g})}\right] \qquad (7)$$

This resonant susceptibility shows both coherent and population-change terms; the former involving only off-diagonal damping, the latter showing explicitly the lifetime dependence of the level $|n'\rangle$.

The multi-resonant susceptibilities derived above have assumed that each scatterer is in exactly the same environment, thus only homogeneous broadening was considered. We now examine the effects of inhomogeneous broadening on these susceptibilities.

B. Inclusion of Inhomogeneous Broadening

When the local environment of each resonant scatterer is not uniform, there is the possibility that the resonant energy levels of each scatterer are also not identical. This leads to a distribution of resonant frequencies for each state, dependent upon some physical parameter of the local environment. For example, the apparent resonant frequencies of molecules in a gas are determined by the longitudinal velocity due to the Doppler shift effect. In solid state physics the local crystal field causes a distribution in the transition frequencies. In general, we assume that there is a distribution function, $g(\alpha,\beta,\ldots)$ dependent on the physical parameters α,β, etc., which describes the probability that a particular resonant frequency will occur. Any physical property of the system dependent on the transition frequencies, such an $\overleftrightarrow{\chi}_R^{(3)}$, must be averaged over this distribution. For example,

$$\langle\overleftrightarrow{\chi}_R^{(3)}\rangle = \int (d\alpha d\beta\ldots) g(\alpha,\beta,\ldots)\overleftrightarrow{\chi}_R^{(3)}. \tag{8}$$

We now examine more closely this general expression by considering first the case of Doppler broadening in gases and then strain broadening in solids.

1. Doppler Broadening

The best characterized form of inhomogeneous broadening is that due to the Doppler effect in gaseous media. In this case there is essentially only one physical parameter — the longitudinal velocity v, and the functional form of the distribution is a simple Gaussian.

We consider a simple geometry in which the optical fields propagate along one axis — either co-propagating or counter-propagating. A molecule with a velocity $\vec{v}$ along this axis (as seen in the lab frame) will see a Doppler shifted optical field of frequency $\omega' = \omega - \vec{k}\cdot\vec{v}$, where $\vec{k}$ is the wavevector of this field. The nonlinear susceptibility associated with this particular molecule must involve this same Doppler shifted frequency. For example, the resonant denominators of the doubly-resonant CARS susceptibility in Eq. (4) should be transformed as

$$\frac{1}{(\omega_1 - \omega_{ng} + i\Gamma_{ng})} \rightarrow \frac{1}{(\omega_1 - \vec{k}_1\cdot\vec{v} - \omega_{ng} + i\Gamma_{ng})}$$

$$\frac{1}{(\omega_1 - \omega_2 - \omega_{g'g} + i\Gamma_{g'g})} \rightarrow \frac{1}{(\omega_1 - \omega_2 - (\vec{k}_1 - \vec{k}_2)\cdot\vec{v} - \omega_{g'g} + i\Gamma_{g'g})} \quad (9)$$

where the small frequency shifts in the nonresonant denominator can be neglected.

The distribution function of velocities is given by the well known Maxwellian distribution

$$g(v) = (\pi^{\frac{1}{2}} v_o)^{-1} e^{-(v^2/v_o^2)} \quad (10)$$

where v is the component of the velocity along the axis of propagation and v_o is the characteristic temperature dependent velocity describing the halfwidth at the e^{-1} point of the velocity distribution. The explicit expressions in Eqs. (9) and (10) can now be used in Eq. (8) to determine the effective nonlinear susceptibility in a Doppler broad-

ened medium.

In the case of co-propagating beams we take $\vec{k}_1$ and $\vec{k}_2$ along the $+\hat{z}$ direction so that the Doppler shifts in Eq. (9) become

$$\vec{k}_1 \cdot \vec{v} = \omega_1 (v/c) \cong \omega_{ng} (v/c)$$

$$(\vec{k}_1 - \vec{k}_2) \cdot \vec{v} = (\omega_1 - \omega_2)(v/c) \cong \omega_{g'g} (v/c) \tag{11}$$

where the fact that ω_1 and $\omega_1 - \omega_2$ are very close to the transition frequencies has been used. An alternative viewpoint is to assume that, instead of the fields shifting frequency, the transition frequency of the molecule has changed. Thus we can write for co-propagating beams

$$\omega_{ng} = \omega^o_{ng} (1 + v/c)$$

$$\omega_{g'g} = \omega^o_{g'g} (1 + v/c) \tag{12}$$

where ω^o_{ng} and $\omega^o_{g'g}$ refer to the central ($v = 0$) transition frequencies and effectively each energy level of the molecule is shifted by the same fractional amount $(1 + v/c)$.

For counter-propagating beams this alternate point of view is not valid, for in this case Eq. (9) becomes

$$\vec{k}_1 \cdot \vec{v} = \omega_1 (v/c)$$

$$(\vec{k}_1 - \vec{k}_2) \cdot \vec{v} = (\omega_1 + \omega_2)(v/c) \tag{13}$$

where $\vec{k}_2$ is assumed to be counter-propagating ($\vec{k}_2 = -\omega_2/c\ \hat{z}$). In this case the Doppler shift of the two-photon transition cannot be written as $\omega_{g'g}(v/c)$ as before and the idea of a molecule with uniformly shifted levels is incorrect. However, this only slightly complicates the evaluation of the averaged susceptibility of Eq. (8). As we will see, there are some four-wave mixing processes in which the Doppler broadening is eliminated.[3] For the rest of this discussion, we consider only the co-propagating beams case.

First consider the general double-resonance term of $\chi_R^{(3)}$ so that only two resonant denominators are present. The averaged value of this term is of the form

$$\langle\chi_D\rangle = C_D \int dv \frac{g(v)}{(\omega_\alpha - \omega_{ij}(v) \pm i\Gamma_{ij})(\omega_\beta - \omega_{k\ell}(v) \pm i\Gamma_{k\ell})} \qquad (14)$$

where ω_{ij} and $\omega_{k\ell}$ are general transition frequencies ($\omega_{ij}(v) = \omega_{ij}^o \times (1 + v/c)$), ω_α and ω_β are general combinations of the input frequencies, and C_D contains all factors independent of v. The plus and minus signs are to be chosen to conform to the particular term under scrutiny. Defining,

$$\nu \equiv v/v_o$$

$$\zeta_\alpha \equiv \zeta_\alpha' + i\zeta_\alpha'' = \left(\frac{\omega_\alpha - \omega_{ij}^o \pm i\Gamma_{ij}}{\omega_{ij}^o}\right)\left(\frac{c}{v_o}\right)$$

$$\zeta_\beta \equiv \zeta_\beta' + i\zeta_\beta'' = \left(\frac{\omega_\beta - \omega_{k\ell}^o \pm i\Gamma_{k\ell}}{\omega_{k\ell}^o}\right)\left(\frac{c}{v_o}\right)$$

we rewrite Eq. (14) as

$$\langle x_D \rangle = C_D\left(\frac{c^2}{v_o^2\omega_{ij}^o\omega_{k\ell}^o}\right)\int_{-\infty}^{\infty} d\nu \, \frac{\pi^{-\frac{1}{2}}e^{-\nu^2}}{(\nu - \zeta_\alpha)(\nu - \zeta_\beta)} \tag{15}$$

The integration of products of Lorentzians and Gaussians can only be performed numerically and is related to the well known plasma dispersion function.[8] Using the properties of this function described below we can further reduce Eq. (15) to a more useful form.

Definitions of the plasma dispersion function are

$$Z(\zeta) \equiv \pi^{-\frac{1}{2}}\int_{-\infty}^{\infty} dt \, \frac{e^{-t^2}}{t - \zeta} \qquad \text{for } \mathrm{Im}(\zeta) = \zeta'' > 0$$

$$Z(\zeta) \equiv 2ie^{-\zeta^2}\int_{-\infty}^{i\zeta} dt \, e^{-t^2} \qquad \text{for all } \zeta'',$$

with the following properties:

$$Z(\zeta^*) = Z^*(\zeta) + 2i\pi^{\frac{1}{2}}e^{-(\zeta^*)^2}$$

$$Z(-\zeta) = -[Z(\zeta^*)]^*$$

$$Z'(\zeta) \equiv dZ/d\zeta = -2(1 + \zeta Z), \qquad \text{with } Z(0) = i\pi^{\frac{1}{2}}$$

$$Z''(\zeta) \equiv d^2Z/d\zeta^2 = -2(Z + \zeta Z') \tag{16}$$

With these properties we can define a function $F(\zeta)$ as

$$F(\zeta) \equiv \pi^{-\frac{1}{2}} \int_{-\infty}^{\infty} dt \, \frac{e^{-t^2}}{t - \zeta} = \begin{cases} Z(\zeta) & \text{for } \zeta'' > 0 \\ Z(\zeta) - 2i\pi^{\frac{1}{2}} e^{-\zeta^2} & \text{for } \zeta'' < 0 \end{cases} \quad (17)$$

In order to complete the transformation of Eq. (15), we realize that

$$\frac{1}{(\nu - \zeta_\alpha)(\nu - \zeta_\beta)} = \left(\frac{1}{\zeta_\alpha - \zeta_\beta}\right)\left(\frac{1}{\nu - \zeta_\alpha} - \frac{1}{\nu - \zeta_\beta}\right) \quad (18)$$

so $\langle \chi_D \rangle$ can be written as the sum of two terms, each involving $F(\zeta)$. The exact form of this expression depends upon the relative signs of the damping terms which are proportional to ζ''_α and ζ''_β. If both are positive, we find

$$\langle \chi_D \rangle = K_D \left[\frac{F(\zeta_\alpha) - F(\zeta_\beta)}{\zeta_\alpha - \zeta_\beta}\right]$$

$$= K_D \left[\frac{Z(\zeta_\alpha) - Z(\zeta_\beta)}{\zeta_\alpha - \zeta_\beta}\right] \xrightarrow{(\zeta_\alpha \to \zeta_\beta)} K_D [Z'(\zeta_\alpha)] \quad (19)$$

where $K_D = C_D c^2/(v_o^2 \omega_{ij}^o \omega_{k\ell}^o)$. This expression is slowly varying as $\zeta_\alpha \to \zeta_\beta$ and has a width approximately equal to the sum of the Doppler width of the two transitions. Similar features occur when ζ''_α and ζ''_β are both less than zero. Thus, in these cases, the nonlinear signal also shows the inhomogeneous broadening.

If one considers the cases with ζ''_α and ζ''_β being of opposite signs the resonant susceptibility shows a sharp narrowing on resonance. Consider explicitly $\zeta''_\alpha > 0$, $\zeta''_\beta < 0$. Eq.(15) becomes

$$\langle\chi_D\rangle = K_D\left[\frac{Z(\zeta_\alpha) - Z(\zeta_\beta)}{\zeta_\alpha - \zeta_\beta} + 2i\pi^{\frac{1}{2}}\frac{e^{-\zeta_\beta^2}}{\zeta_\alpha - \zeta_\beta}\right]$$

$$\xrightarrow{(\zeta_\alpha \to \zeta_\beta)} K_D\left[Z'(\zeta_\beta) + \frac{2i\pi^{\frac{1}{2}}e^{-\zeta_\beta^2}}{\zeta_\alpha - \zeta_\beta}\right] \tag{20}$$

In the limit as $\zeta_\alpha \to \zeta_\beta$, the first term approaches the first derivative of $Z(\zeta_\beta)$ and is the usual Doppler broadened profile, while the second term shows a sharp Lorentzian resonance with a width of $\zeta_\alpha'' - \zeta_\beta'' = (c/v_o)(\Gamma_{ij}/\omega_{ij}^o + \Gamma_{k\ell}/\omega_{k\ell}^o)$. It the Doppler width is much broader than the homogeneous widths, the resonant susceptibility contains a term which is essentially "Doppler-free". We note that reversing the signs of ζ_α'' and ζ_β'' amounts to an exchange of α and β in Eq. (20), thus this case will also show that same characteristic narrowing. Examining the doubly-resonant susceptibilities given in Eqs. (4) - (6), we find that the normal resonant CARS provides a Doppler broadened spectrum, whereas the upper state resonance CARS and the particular form of CSRS both will yield "Doppler-free" spectra.

It is straightforward to extend the above discussion to the triply-resonant case. Using the same procedure as in Eq. (18), the triple product in the denominator may be written as a sum of three single-resonance denominators, each of which is related to $Z(\zeta)$ using Eq. (17). For the general triply-resonant case we find

$$\langle\chi_T\rangle = K_T\left[\frac{F(\zeta_\alpha)}{(\zeta_\alpha - \zeta_\beta)(\zeta_\alpha - \zeta\ )} + \frac{F(\zeta_\beta)}{(\zeta_\beta - \zeta_\alpha)(\zeta_\beta - \zeta_\gamma)} + \frac{F(\zeta_\gamma)}{(\zeta_\gamma - \zeta_\alpha)(\zeta_\gamma - \zeta_\beta)}\right] \tag{21}$$

where K_T is a constant (independent of v) and the ζ's are defined as in

the text above Eq. (15). The interesting cases of "Doppler-free" spectra are determined again by examining the combinations of positive and negative damping constants. If all imaginary parts are positive, such that $F(\zeta) = Z(\zeta)$, and we approach resonance such that $\zeta_\alpha \to \zeta_\beta \to \zeta_\gamma$, then the combination of terms in Eq. (21) approaches $Z''(\zeta_\alpha)/2$ which is again slowly varying like the inhomogeneous lineshape. If any one of ζ_α'', ζ_β'', ζ_γ'' has a different sign from the other two, there will be narrowing similar to that shown in Eq. (20). Examining the triply-resonant susceptiblilty of Eq. (7) for the RIKES-type process, it can be seen that the coherent term (involving only off-diagonal damping) will show narrowing. The population-change terms involve a zero-frequency resonance from the denominator $(\omega_1 - \omega_1 - \omega_{n'n'} + i\Gamma_{n'n'}) = i\Gamma_{n'n'}$. This denominator can then be removed from the integral, leaving only two resonance denominators to be averaged, which is the case described in Eqs. (19) and (20). Examination reveals that one of these population terms also shows narrowing, while the other does not. Thus the total lineshape of this triply-resonant susceptibility is the sum of a broad Doppler background and a combination of narrower Lorentzian lineshapes.

The spectral narrowing described here can appear in any four-wave mixing process which satisfies the criteria related to the relative signs of the damping factors. Narrowing in the stimulated emission (gain) process has been known for some time, and the spontaneous analog, fluorescence line narrowing, is an established technique.[9] The preceding theory points out the extensions of this narrowing effect to other wave mixing processes — even some second-order processes, for example quadrupole difference frequency generation[10], can

show similar narrowing effects.

2. Inhomogeneous Broadening in Solids

We focus our attention on rare-earth ions in solids.[11] It is well known that the local crystal fields at the ionic sites act as weak perturbations, slightly shifting levels and making allowed previously forbidden transitions. At low temperatures these inner shell transitions (e.g. $4f \rightarrow 4f$) can have extremely narrow homogeneous linewidths (widths of 15 kHz have been reported[12]). However, due to random microscopic strains, the local fields at structurally identical sites take on a spread of values, which leads to a distribution in the energy levels of the ions. It is generally assumed that there is a Gaussian distribution of random strains, leading to a Gaussian profile for the inhomogeneous broadening. In the simplest case we assume that there is only one crystal field parameter which effects all levels proportionately, i.e. all levels of each ion are shifted by the same fractional amount. In this way, we treat the strain broadening in a solid with the same formalism as Doppler broadening in a gas (as described above).

At best this is only an approximation since there are often many crystal field parameters (especially if the lattice site has low symmetry), each with its own strength and spatial symmetry. Futhermore, the coupling between an ion and a given crystal field will depend upon the symmetry of the particular ionic level being considered. The net result is that the crystal field perturbation may cause an "accidental degeneracy" of ionic levels. By "accidental", it is meant that different ions may have the same transition frequency within the inhomo-

geneous profile even though these ions do not interact with the exact same crystal fields. Thus, there are several possible combinations of the crystal fields which will result in the same transition frequency. This is indicated schematically in Fig. 3. Although all of these ions will absorb the photon $\omega_1 = \omega_{ng'}$, the transition frequency $\omega_{ng'}$, to level $|g'\rangle$ need not be the same, since the different crystal fields at the different sites may interact differently with the level $|g'\rangle$. Therefore, a two-photon transition from $|g\rangle$ to $|g'\rangle$ will show a resonance width of $\Delta\nu_D$ as ω_2 is scanned through the resonance. This is to be compared to the homogeneous width of $\Gamma_{g'g}$ which would occur if only a single parameter determined the energy levels. One can use the deviations of the measured width from the homogeneous width to probe the extent of this "accidental degeneracy". Even with this "accidental degeneracy" width, if $\Delta\nu_D$ is much less than the Doppler width, there should still be considerable narrowing in the four-wave mixing spectra.

C. Effects of One-Photon Absorption

When considering multi-resonant processes, the effects of one-photon absorption become very important. To incorporate linear absorption into the theory of the nonlinear output signal, we define a complex wavevector, $\vec{k} = \vec{k}' + i\vec{k}''$, to describe propagation in an absorbing media. Then, for example, the output field is of the form

$$\vec{E}(\omega) = \vec{\mathcal{E}}(\omega)\, e^{ik'z}\, e^{-k''z}$$

and

$$|\vec{E}(\omega)| = |\vec{\mathcal{E}}(\omega)|\, e^{-k''z} \quad . \tag{22}$$

Eq. (4) of Section II describing the growth of the signal amplitude $\vec{\mathcal{E}}(\omega)$ is generalized by including the imaginary parts of all wavevectors in the expression for $\Delta\vec{k}$

$$\Delta\vec{k} = (\vec{k}'_a + \vec{k}'_b + \vec{k}'_c - \vec{k}') + i(\vec{k}''_a + \vec{k}''_b + \vec{k}''_c - \vec{k}'') \tag{23}$$

Again assuming plane wave inputs, we have the output amplitude $\vec{\mathcal{E}}(\omega)$ proportional to an effective interaction length, $\mathcal{L}$, given by

$$\mathcal{L} \equiv \left| \frac{e^{i\Delta kz} - 1}{i\Delta k} \right| \tag{24}$$

for propagation along the $\hat{z}$-axis. When absorption is negligible and phasematching is achieved, this expression reduces to $\mathcal{L} = z$. In general however, $\Delta k'' \neq 0$, so $\mathcal{L} < z$. In the limit of very strong absorption ($\Delta k''z >> 1$), we find $\mathcal{L} \cong (\Delta k'')^{-1}$ which implies that the signal is produced only within about one effective absorption length.

Consider a typical experimental situation in which one frequency (normally ω_1) remains fixed, while the other frequency (ω_2) is scanned. Suppose there is linear absorption at ω_2 Then as this frequency passes through resonance, χ_R will be enhanced while the effective length $\mathcal{L}$ will decrease. The enhancement increases the strength of the output field amplitude while the smaller effective length decreases this amplitude. The resulting lineshape will then be distorted by the one-photon absorption and will require correction to determine the resonant susceptibility lineshape. If sufficient information about the linear absorption is known, we may compensate for $\mathcal{L}$ at each point in the spectrum. As displayed in Eq. (22), linear absorption

at the output frequency also appears in the field amplitude (Eq. (22)) and must be taken into account. Absorption at the output frequency should then be avoided, since it both limits the phasematching factor $\mathcal{L}$ and results in the exponential attenuation of the output field.

An alternative to the above procedure is found in the polarization-sensitive techniques described in the first part of this thesis. In Section IID we described that a polarizer placed in the output beam could be used to essentially separate the resonant and nonresonant contributions to the output signal. Futhermore, it was described that if the ratio of the transmitted and rejected signals was formed, it could be used to normalize the signal against laser intensity fluctuations. In the present case this same technique could be used to remove the effects of linear absorption on the nonlinear signal. If the resonance under examination is weak compared to the strength of the nonresonant term, the rejected beam will be made up of the nonresonant signal which will be nondispersive, except for the effects of linear absorption. Forming the ratio of the transmitted resonant signal and the rejected nonresonant signal, we normalize against the absorption and determine the dispersion in the signal due only to the resonant susceptibility.

In concluding this section, we have considered multiply-resonant susceptibilities in inhomogeneously broadened systems. Explicit expressions for certain doubly- and triply-resonant susceptibilities have been given using a diagrammatic technique. It has been shown that specific four-wave mixing processes have spectral widths much narrower than the inhomogeneous widths and the means to identify such processes is described. The effects of linear absorption on the non-

linear output signal have been considered, allowing the distorted output to be corrected for the linear effects. It has also been shown that the use of polarization-sensitive detection techniques can provide a nonlinear reference signal to normalize out the effects of linear absorption. Thus, multi-resonant four-wave mixing has potential to become a useful and informative form of nonlinear spectroscopy.

References

1. R. T. Lynch, Jr., H. Lotem, and N. Bloembergen, J. Chem. Phys. 66, 4250 (1977); S. A. J. Druet, B. Attal, T. K. Gustafson, and J. P. E. Taran, Phys. Rev. A18, 1529 (1978).
2. I. Chabay, G. K. Klauminzer, and B. S. Hudson, Appl. Phys. Lett. 28, 27 (1976); A. Lau, M. Pfeiffer, and W. Werncke, Opt. Commun. 23, 59 (1977); B. Attal, O. O. Schnepp, and J. P. E. Taran, Opt. Commun. 24, 77 (1978).
3. S. A. J. Druet, J. P. E. Taran, and Ch. J. Bordé, J. de Phys. 40, 819 (1979).
4. J. L. Oudar and Y. R. Shen (to be published).
5. N. Bloembergen, Nonlinear Optics (Benjamin, New York, 1965); N. Bloembergen, H. Lotem, and R. T. Lynch, Jr., Ind. J. Pure & Appl. Phys. 16, 151 (1978).
6. T. K. Yee and T. K. Gustafson, Phys. Rev. A18, 1597 (1978).
7. N. Bloembergen, Nonlinear Optics, p. 21 (Benjamin, New York, 1965).
8. B. D. Fried and S. D. Conte, The Plasma Dispersion Function (Academic Press, New York, 1961).
9. M. S. Feld and A. Javan, Phys. Rev. 177, 540 (1969).
10. D. S. Bethune, R. W. Smith, and Y. R. Shen, Phys. Rev. Lett. 37, 431 (1976).
11. For a review of the properties of rare-earth ions in solids see, for example, S. Hüfner, Optical Spectra of Transparent Rare Earth Compounds (Academic Press, New York, 1978).
12. A. Szabo, R. G. DeVoe, S. Rand, and R. G. Brewer, Bull. Am. Phys.

Soc. 24, 444 (1979).

13. R. Flach, D. S. Hamilton, P. M. Selzer, and W. M. Yen, Phys. Rev. B15, 1248 (1977).

Figure Captions

Fig. 1 Diagrams used in determining double resonance susceptibilities. (a) CARS with $\omega_1 \approx \omega_{ng}$ and $\omega_1 - \omega_2 \approx \omega_{g'g}$ ($\omega_3 = 2\omega_1 - \omega_2$); (b) CARS with $\omega_1 \approx \omega_{n'g}$ and $\omega_2 \approx \omega_{ng}$ such that $\omega_1 - \omega_2 \approx \omega_{n'n}$ (upper state resonance, $\omega_3 = 2\omega_1 - \omega_2$); (c) CSRS with $\omega_2 \approx \omega_{ng}$ and $\omega_1 - \omega_2 \approx \omega_{g'g}$ ($\omega_4 = 2\omega_2 - \omega_1$).

Fig. 2 Diagrams used in determining the triple resonance susceptibility for the RIKES process, $\omega_2 = \omega_1 - \omega_1 + \omega_2$, with $\omega_1 \approx \omega_{n'g}$ and $\omega_2 \approx \omega_{n'g'}$.

Fig. 3 Schematic diagram showing the possibility of "accidental degeneracy" in a medium in which several parameters contribute to the inhomogeneous broadening, as in the case of the crystal fields in a solid.

Figure 1

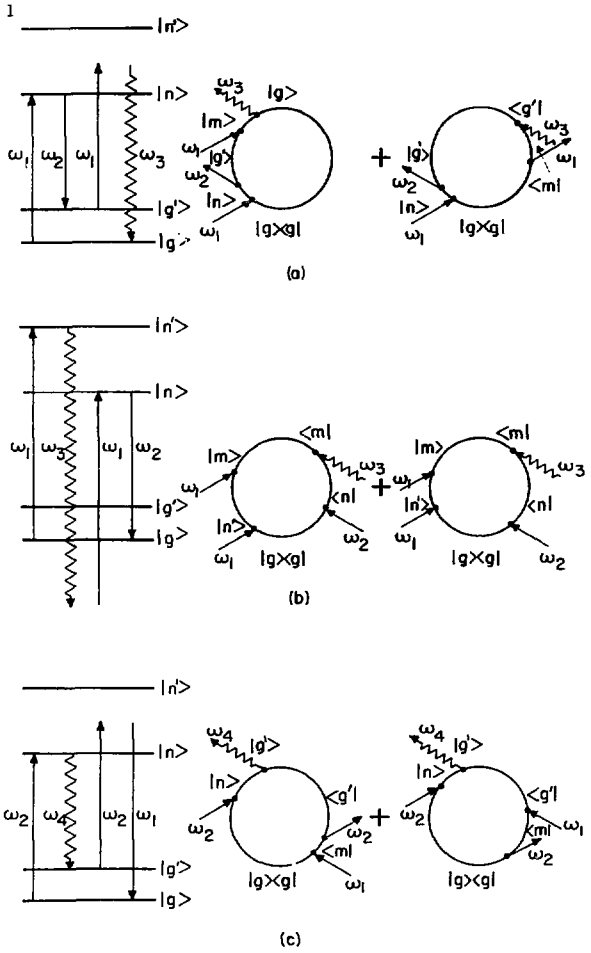

Figure 2

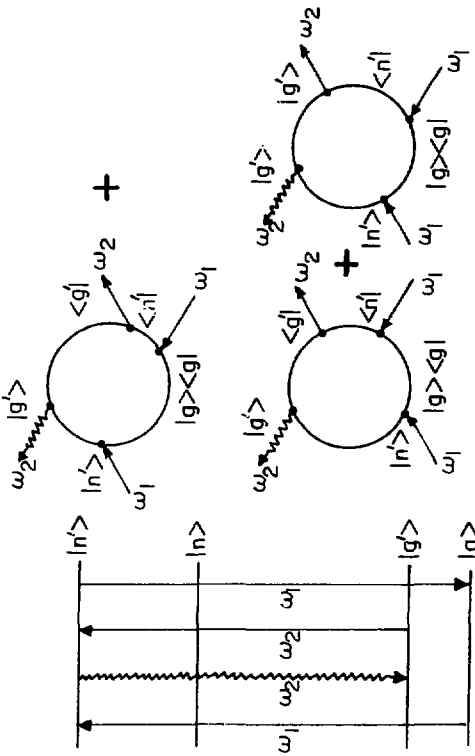

XBL 807-5543

Figure 3

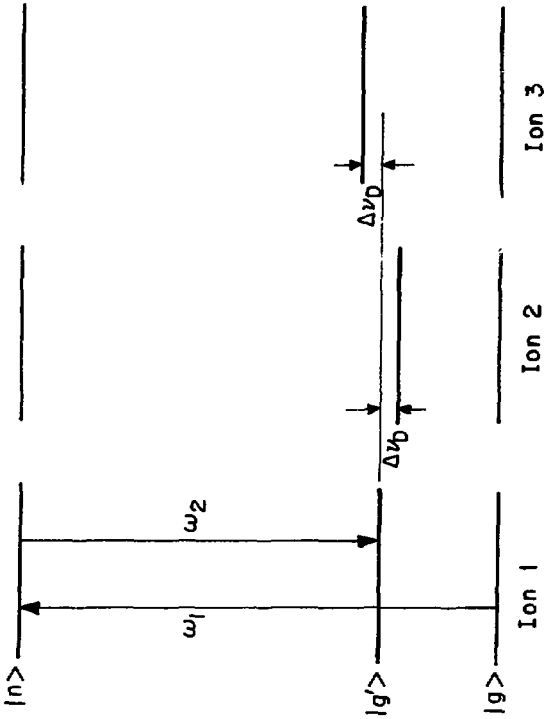

XBL807-5544

V. MULTI-RESONANT FOUR-WAVE MIXING IN INHOMOGENEOUSLY BROADENED MEDIA — EXPERIMENT

The theory of multi-resonant four-wave mixing described in the previous section indicates several interesting features to be examined experimentally. Most notable among these are the lineshapes of the processes which should show the narrowing well below the inhomogeneous width (assuming the homogeneous width is much smaller). Also it should be possible to determine dipole matrix elements and Raman polarizabilities between various levels of the material system using these nonlinear techniques. As mentioned in Section IV, ions in condensed matter can provide sharp electronic transitions that show inhomogeneous strain broadening, and so are nearly ideal to demonstrate the features of the multi-resonant susceptibilities. Furthermore, the four-wave mixing techniques can be used to study the physical parameters of the ions, which to date have been studied mostly by absorption and fluorescence techniques.

In the first part of this section we describe the sample used in this work, while the second part deals with the relevant linear optical properties of the sample. The next segment discusses a triple resonance RIKES-type measurement made to observe the predicted narrowing and to further characterize the ionic system. This is followed by a description of a double resonance CARS experiment performed on the same electronic levels. The last part of this section discusses an attempt to observe the form of double resonance CARS involving an upper state resonance.

A. Sample — $Pr^{+3}:LaF_3$

Of primary importance in the choice of the sample for use in these experiments is the location of the electronic energy levels. It is most desirable to have the transitions from the ground state accessible to ordinary dye lasers operating in the center of the visible spectrum. It is also desirable to have electronic Raman levels only a few thousand wavenumbers above the ground state to facilitate phasematching in the CARS experiment. Finally, the spectroscopic and linear optical properties should be reasonably well known to allow estimation of the strengths of the nonlinear effects. Many of these requirements are fulfilled by praseodymium-doped lanthanum trifluoride, $Pr^{+3}:LaF_3$.

The host crystal LaF_3 has a space symmetry D_{6h} with a bimolecular basis.[1] Optically, lanthanum trifluoride is transparent with no linear absorption until below 2000Å;[2] however, it is birefringent with $n_e = 1.597$ and $n_o = 1.603$. The linear dispersion of the refractive index is known from the work of Wirick,[3] and will be used to determine the phasematching angle in the CARS work. The crystals of LaF_3 can be easily grown of good optical quality, and are insoluble in water (this is important since this work requires low temperatures).

The choice of praseodymium as the dopant was made for several reasons: (a) Pr^{+3} has electronic levels accessible to blue and red dye lasers;[2] (b) these levels have been partially characterized by the relatively large amount of experimental work performed on $Pr^{+3}:LaF_3$;[4-7] (c) Pr^{+3} is very soluble in LaF_3 and shows no clustering even at high concentrations; and (d) the crystals are readily available in a wide range of concentrations (up to 20%) and in specific op-

tical orientations from Optovac, Inc.

Fig 1(a) indicates an approximate term scheme for the Pr^{+3} ions in the LaF_3 host. There are two electrons in the 4f shell which result in a $^3H_4$ ground state using Hund's rules.[8] Since the site symmetry of the praseodymium ions is known to be relatively low (C_{2v}),[4] the crystal field splits each state into the 2J + 1 substates of each manifold. Thus there are a total of 9 states in the ground ($^3H_4$) manifold. The two nearest manifolds are the $^3H_5$ and $^3H_6$ with the lowest lying states at 2179 cm^{-1} and 4222 cm^{-1} respectively. The important excited states are $^3P_0$ at 20925 cm^{-1} and $^1D_2$ at 16872 cm^{-1}. Most of the experimental work has involved the $^3H_4$, $^3H_6$, and $^3P_0$ states which are designated $|g\rangle$, $|g'\rangle$, and $|n'\rangle$ in Fig. 1(b).

As the temperature of the Pr^{+3}:LaF_3 is lowered, the thermally broadened lines of the ions narrow.[4] At liquid helium temperatures, however, the spectral lines show the inhomogeneous broadening due to the microscopic random strains. It is reported[5] that the inhomogeneous widths of the $^3P_0$ state are about 30 GHz for 5% Pr (by number) and about 1.3 GHz for 0.2% Pr. On the other hand, photon echo experiments,[9] used to determine the homogeneous linewidths of states connected to the ground state, find a natural linewidth of 3 MHz for the $^3P_0 \rightarrow {}^3H_4$ transition. Furthermore, this homogeneous width is strongly temperature dependent, due to phonon relaxation processes as described by Yen, et al., and increases to about 1 GHz at 20°K. Thus we choose to use a sample of 1% Pr at temperatures below 20°K, so that the homogeneous width will be about an order of magnitude less than the inhomogeneous linewidth.

Since any transition between the levels of Pr^{+3} ions are allowed

only through the perturbation mixing of the crystal field, all oscillator strengths are quite small,[7] typically $f < 10^{-6}$. Another characteristic to be expected is the long lifetimes of these states[6] — 47 μsec for the $^3P_0$ level and 520 μsec for the $^1D_2$ level. Another feature of the Pr^{+3}:LaF_3 system is a strong anisotropy in the transition probabilities — only $\vec{E} \perp \hat{c}$-axis transitions are allowed. A final characteristic worth noting is the lasing action between the $^3P_0$ and $^3H_6$ states which can occur when population inversion is achieved.[10]

The preceding information provides an overview of the Pr^{+3}:LaF_3 sample used in these experiments. In order to calculate the various resonant susceptibilities, more specific information is needed about the matrix elements. We consider here the doubly-resonant CARS and triply-resonant RIKES processes involving the dipole matrix elements $|\langle^3P_0|\vec{\mu}|^3H_4\rangle|$ and $|\langle^3H_6|\vec{\mu}|^3P_0\rangle|$ and the Raman polarizability $|\langle^3H_6|\overleftrightarrow{\alpha}|^3H_4\rangle|$. The dipole matrix elements are found from linear absorption and fluorescence measurements or, in this case, from measurements of the stimulated emission.[6,7] The only experimental work on electronic Raman scattering in this sample was done by Hougen and Singh[11] (using pure $PrC\ell_3$) with only qualitative measurements regarding the $^3H_4$, $^3H_5$, and $^3F_2$ levels of Pr. Observation of multi-resonant nonlinear processes in this sample will provide additional information about the values of these quantities, (in addition to testing the theoretically predicted lineshapes for these processes).

B. Linear Absorption: $^3H_4 \rightarrow {}^3P_0$

The initial experimental work performed on Pr^{+3}:LaF_3 was a simple linear absorption measurement from which the matrix element, $\mu_{n'g}$ =

$\langle {}^3P_0|\mu|{}^3H_4\rangle$ and the inhomogeneous linewidth, $\gamma_{n'g}$, are determined. This also provided the exact location of the resonant frequency.

The experimental apparatus[12] consisted of a narrow-band (FWHM $\approx$ 4 GHz) pulsed dye laser beam passing through the cooled sample and monitored on a photodiode with a gated-electronic detection system, see Fig. 2. In this case the flashlamp-pumped dye laser was operated with Coumarin 480 laser dye in methanol to obtain lasing near the 4777Å (20925 cm^{-1}) absorption line of Pr^{+3}. The maximum output of 1 kW in a 0.4 μsec pulse was attenuated to less than 1 W and then sent unfocussed into the sample (spot size $\approx$ 2 mm diameter). The 1% Pr-doped sample with the $\hat{c}$-axis in the face was placed on the cold finger of an Air Products, Inc. liquid helium cryostat. Sample temperatures of $\approx 15°K$ were routinely obtained as monitored on a chromel/gold-iron (.07%) thermocouple epoxied to the sample holder. The absorption was monitored using the dual-channel, gated electrometer/analog divider described in Section III. A beamsplitter before the sample provided a signal for the reference photodiode. The transmission was normalized to unity with the laser tuned far off-resonance, then the frequency was scanned stepwise through the absorption. Care was taken to adjust the input polarization so as to maximize the absorption.

Figure 3 shows the absorption spectrum of the ${}^3H_4 \rightarrow {}^3P_0$ transition for this 1% sample with $\vec{E}(\omega_1) \perp \hat{c}$. The measured half-width at half-maximum of this absorption is about 11 GHz which is due entirely to inhomogeneous broadening. The maximum absorption coefficient for this transition is 19 cm^{-1} at line center. For simple linear absorption, the peak absorption coefficient, α_{max}, is related to the dipole matrix element by

$$\alpha_{max} = \frac{4\pi^2 \omega_1 N |\mu_{n'g}|^2}{n\,\hbar c}\, g_{max}(\omega_1) \qquad (1)$$

where $\mu_{n'g}$ was defined above, N is the density of Pr ions, n is the index of refraction at ω_1, and $g(\omega_1)$ is the normalized lineshape function. From Fig. 3 we see that the absorption spectrum does not fall off as rapidly as the anticipated Gaussian profile, although the fit near line center is good. Yen, et al.[4] have made similar observations on the $^3P_0 \rightarrow {}^3H_4$ fluorescence spectrum and it is believed that the deviations from a Gaussian profile are due to small macroscopic strains within the sample.[13]

We take $g_{max} = (\ln 2/\pi)^{\frac{1}{2}} \gamma_{n'g}^{-1}$ for a simple Gaussian lineshape and use Eq. (1) to calculate the strength of the matrix element. With $\omega_1/2\pi c = 20925\ cm^{-1}$, n = 1.60, and N(Pr) = 1% N(La) = (.01)(1.81 × 10^{22} cm^{-3}) = 1.81 × 10^{20} cm^{-3}, we have

$$|\mu_{n'g}| = 2.2 \times 10^{-21}\ \text{esu} \qquad (^3H_4 \rightarrow {}^3P_0)$$

which implies an oscillator strength of ~2 × 10^{-7}.

In the previous discussions of multi-resonant nonlinear susceptibilities it was assumed that only the ground state was populated. However, when one of the input laser frequencies is tuned to a one-photon resonance, there will be population redistribution resulting in a reduction in the population difference, $\rho_{gg} - \rho_{n'n'}$, and a saturation broadening of the absorption linewidth. These effects both reduce the nonlinear output and are minimized by keeping the input intensity or energy below a certain saturation level defined below.

To discuss saturation we consider a simple, nondegenerate two-level system with an inhomogeneous width γ_I (HWHM). For simplicity we assume the input intensity, $I(\omega_\ell)$, is uniformly spread over the laser bandwidth, Γ_ℓ, and that $\gamma_I >> \Gamma_\ell >> \gamma_H$ (the homogeneous width). The number density of absorbers within the bandwidth of the laser is taken as N_o, and the number density in the ground state is N_g and in the upper state is N_u, such that $N_o = N_g + N_u$. The upper state density then satisfies[14]

$$\frac{dN_u}{dt} = -\frac{N_u}{\tau_{n'}} + (N_g - N_u)\left\{\frac{\alpha(\omega_\ell)I(\omega_\ell)}{N_o\hbar\omega_\ell}\right\} \tag{2}$$

where the first term on the right describes the normal decay of the excited population with a lifetime of $\tau_{n'}$, while the second term increases the excited population through absorption. In Eq. (2) $\alpha(\omega_\ell)$ is the average absorption coefficient over the laser bandwidth. Note that the bracketed term in this equation represents the probability that one ground state ion will absorb a photon and thus be excited.

We discuss saturation of this transition in terms of the population difference, $N_g - N_u$, and choose to define "saturation" to occur when $N_g - N_u = \frac{1}{2}N_o$, i.e. when the population difference equals one-half of its initial value (all ions in the ground state). This will be the case when we have $N_g = 3/4\ N_o$ and $N_u = 1/4\ N_o$.

We consider two limiting cases: steady state (with the laser pulse length, τ_ℓ, much longer than the upper state lifetime, $\tau_{n'}$) and the transient regime (with $\tau_\ell << \tau_{n'}$). In the steady state case we have no change in the upper state population, so $dN_u/dt = 0$. Using Eq. (2) we can then define a saturation intensity when $N_u = 1/4\ N_o$.

We have $I_s \equiv N_o \hbar\omega_\ell/(2\alpha\tau_{n'})$, in this case. In the physical situation studied here, we have the laser pulse length of 0.4 μsec and the upper state lifetime of 47 μsec, so we are clearly in the transient regime. In this case we discard the decaying population term and integrate the expression for dN_u/dt directly to find

$$\ln\left(\frac{N_o}{N_o - 2N_u}\right) = \left[\frac{\alpha}{N_o \hbar\omega_\ell}\right]\int_0^{\tau_\ell} I\, dt = \left[\frac{\alpha}{N_o \hbar\omega_\ell}\right] F \qquad (3)$$

where F is the energy fluence [J/cm^2] of the incoming beam. At saturation we have the saturation energy fluence F_s as

$$F_s \equiv N_o \hbar\omega_\ell \ln(2)/(2\alpha) \quad .$$

To evaluate this for the $^3H_4 \rightarrow {}^3P_0$ transition, we have $\alpha = 19$ cm^{-1}, $\hbar\omega_\ell = 4.2 \times 10^{-19}$J, and N_o (the number density within the laser bandwidth) is given approximately by the product of the total number density of ions over the whole inhomogeneous profile and the ratio of the laser bandwidth to the full inhomogeneous width, or $N_o = N \times [4\text{ GHz}/22\text{ GHz}] = 0.18\ N = 3.3 \times 10^{19}$ cm^{-3}. Thus we find $F_s = 0.3$ J/cm^2 for the energy fluence to saturate this transition with a laser of 4 GHz bandwidth. This is only a crude estimate however, since we have not considered any depletion of the incoming beam as it passes through the sample. In our case the absorption is fairly strong (only 15% transmission at the peak), so actually we should solve Eq. (2) coupled with an equation describing the decrease of the laser intensity at a depth ℓ within the sample, e.g.

$$\frac{dI}{d\ell} = \frac{N_g(\ell) - N_u(\ell)}{N_o} \alpha I(\ell)$$

which includes the effects of reduced absorption due to saturation. Solving these coupled differential equations will normally require numerical computation beyond what is necessary for this discussion. We may assume that the saturation energy fluence is of the order of 1 J/cm^2 and use this number as a rough guide to avoid saturation effects.

In nonlinear processes (such as CARS) which scale either linearly or quadratically with the input intensity, the restrictions placed on the input energy fluence by saturation greatly limit the strength of the nonlinear output. This can be overcome to some extent by going to yet shorter input pulses, while keeping the energy fluence near the saturation limit. We shall return to this point in our discussion of double resonance CARS below.

C. Triply-Resonant RIKES

The first nonlinear process to be considered here is four-wave mixing with $\omega_2 = \omega_1 - \omega_1 + \omega_2$, involving the RIKES-type triply-resonant susceptibility described in Section IVA. [We now identify the state $|g'\rangle$ with the $^3H_6$ level of Pr^{+3}.] After integration over the inhomogeneous distribution of resonant frequencies (as is approximately valid for strain broadening in solids), the most strongly resonant terms of Eq. (7), Section IV become

$$(\chi_R)_{max} \approx -i\left[\frac{N|\mu_{n'g}|^2|\mu_{n'g'}|^2}{\hbar^3}\right]\left(\frac{2\pi^{\frac{1}{2}}}{(v_o/c)\omega^o_{n'g}}\right)\left\{\frac{1}{[\Gamma_{n'g'} + (\omega^o_{n'g'}/\omega^o_{n'g})\Gamma_{n'g'}]}\right\}$$

$$\times\left\{\frac{1}{[\Gamma_{g'g} + (\omega^o_{g'g}/\omega^o_{n'g'})\Gamma_{n'g'}]} + \frac{1}{\Gamma_{n'n'}}\right\} \qquad (5)$$

where all input frequencies are assumed to be exactly on resonance. Examining this expression for $(\chi_R)_{max}$ we see that on resonance it is a negative imaginary number. From Section II we found that

$$d\mathcal{E}(\omega_2)/dz = i\beta\chi^{(3)}|\mathcal{E}(\omega_1)|^2\mathcal{E}(\omega_2)$$

which, with $\chi^{(3)} = -i|(\chi_R)_{max}|$, becomes

$$d\mathcal{E}(\omega_2)/dz = +\beta|(\chi_R)_{max}||\mathcal{E}(\omega_1)|^2\mathcal{E}(\omega_2) \ .$$

Since β is a positive, real parameter, this expression describes the exponential growth of the ω_2 field, i.e. gain. Also note that $(\chi_R)_{max}$ is made up of contributions from both coherent processes, involving the off-diagonal damping parameters, $\Gamma_{g'g}$ and $\Gamma_{n'g'}$, and a population term, involving the lifetime of the excited state $\tau_{n'} \equiv \Gamma_{n'n'}^{-1}$. Below, we will compare the strengths of these two contributions.

The expression in Eq. (5) is written for the case of Doppler broadening with the parameter $(v_o/c)\omega^o_{n'g}$ describing the inhomogeneous width of the transition from $|g\rangle$ to $|n'\rangle$. More precisely, when $v = v_o$, the frequency shift from line center is equal to the inhomogeneous width defined with respect to the e^{-1} point of the profile. Using

instead the inhomogeneous width $\gamma_{n'g}$ with respect to the half maximum (HWHM), we have

$$\omega^{o}_{n'g}(1 - v_o/c) = \omega^{o}_{n'g} - \gamma_{n'g}/(\ell n2)^{\frac{1}{2}} .$$

We generalize Eq. (5) by rewriting $(v_o/c)\omega^{o}_{n'g}$ as $\gamma_{n'g}/(\ell n2)^{\frac{1}{2}}$. Furthermore, in the present case the laser linewidths ($\Gamma_\ell = 4$ GHz) greatly dominate the homogeneous linewidths, which can be neglected in comparison. Finally, as pointed out above, we are in the transient regime ($\tau_\ell << \tau_{n'}$) so the laser pulse length must replace the upper state lifetime. Thus Eq. (5) can be rewritten,

$$(\chi_R)_{max} \approx -i\left(\frac{N|\mu_{n'g}|^2|\mu_{n'g'}|^2}{\hbar^3}\right)\left[\frac{2(\pi\ell n2)^{\frac{1}{2}}}{\gamma_{n'g}\,\Gamma_\ell}\right]\left[\frac{1}{\Gamma_\ell} + \tau_\ell\right] . \qquad (6)$$

Let us now compare the coherent and population contributions, the former is proportional to $(\Gamma_\ell)^{-1}$ and the latter is proportional to τ_ℓ. For the flashlamp-pumped dye laser system, we have $\Gamma_\ell\tau_\ell \approx 2\pi(4\text{ GHz}) \times (0.4\ \mu\text{sec}) \sim 10^4$ (which is to say that this system is very far from the Fourier transform limit). Thus the coherent term will be negligible compared to the population term.

The only unknown parameter in Eq. (6) is the dipole matrix element $|\mu_{n'g'}|$, connecting the $^3P_0$ and $^3H_6$ states. Fortunately, the fact that the crystal will lase on this transition allows us to make a crude estimate of the susceptibility for this RIKES process.

We consider the simplest model of this lasing: all photons at ω_1 which are absorbed populate the $^3P_0$ state, providing a number density

$\mathcal{N}_{n'}$ of excited ions which can emit to the $^3H_6$ level. The gain coefficient per unit length, G, defined in analogy with the absorption coefficient of Eq. (1), can be estimated from the lasing threshold condition. Assuming the feedback for lasing comes only from the 5.3% reflection at the LaF_3 - air interface of the 0.1 cm thick sample, this threshold condition becomes

$$e^{G\ell} = R^{-1} \quad \Rightarrow \quad G = 30 \text{ cm}^{-1}$$

where R is the reflectivity at the interface and ℓ is the sample thickness. To estimate the number density of ions which give rise to this gain, we have measured the amount of energy absorbed from the pump beam at ω_1. This is then a direct measure of the number density $\mathcal{N}_{n'}$ in the upper state. The energy absorbed per unit volume was the energy fluence at lasing threshold (0.7 J/cm^2) times the fraction of the beam which was absorbed (85%) divided by the sample length (0.1 cm). This leads to about 6 J/cm^3 energy density or about 1.4×10^{19} photons/cm^3 absorbed, thus $\mathcal{N}_{n'} = 1.4 \times 10^{19}$ excited ions/cm^3 within the laser bandwidth of 4 GHz.

Using Eq. (1) we can evaluate the gain coefficient, instead of the loss or absorption coefficient. With the above information we roughly estimate the matrix element $|\langle^3H_6|\mu|^3P_0\rangle|$ as

$$|\mu_{n'g'}| \approx 7 \times 10^{-21} \text{ esu} .$$

This should be considered as only an order of magnitude calculation, due to the simplicity of the argument presented here, but can be used

to estimate the strength of $(\chi_R)_{max}$.

Recall that $N = 1.8 \times 10^{20} cm^{-3}$ for the total number density of Pr ions, $|\mu_{n'g}| \approx 2 \times 10^{-21}$ esu and $|\mu_{n'g'}| \approx 7 \times 10^{-21}$ esu for the dipole matrix elements, $\gamma_{n'g} \cong 11$ GHz for the inhomogeneous width, and $\tau_\ell =$ 0.4 μsec and $\Gamma_\ell = 4$ GHz for the laser parameters. Evaluating the susceptibility from Eq. (6), we find

$$|(\chi_R)_{max}| \sim 2 \times 10^{-8} \text{ esu} \quad .$$

This is to be compared to the typical singly-resonant CARS susceptibility of 3×10^{-13} esu as for the 992 cm^{-1} Raman mode of benzene. Since real population changes are occurring, χ_R is much larger in this multi-resonant case. Instead of a RIKES-type susceptibility, it would be more appropriate to call this a stimulated emission susceptibility, since in this case it is actually a population change effect. In any case, such a strong resonance should be easily observable.

The experimental technique to measure χ_R directly was quite similar to the RIKES setup described in Section II (see Fig. 4 of that section). In this case we used the fact that the stimulated emission gain at frequency ω_2 is anisotropic due to the polarization selection rules of the Pr in the LaF_3 host. The field at $\omega_1 \cong \omega_{n'g}$ was set perpendicular to the crystal optic axis (and so was strongly absorbed) and the field at $\omega_2 \cong \omega_{n'g'}$ was at approximately 45° to this axis. A polarization analyzer was placed after the sample to null the probe beam (ω_2) when the pump beam (ω_1) was not present. The probe field experienced gain for the component along the pump field and no gain in the other component. Ideally, light at the probe frequency will only

be detected through the analyzer when the pump field is present. In reality the finite leakage of any polarizer (see discussion of polarization-sensitive CARS) will lead to a background signal which can be used to measure the relative strength of the gain signal. The ratio of the signal due to the gain process and that due to the leakage is given by

$$\mathcal{R} = \mathcal{G}^2/8\theta_e^2 \tag{8}$$

where $\mathcal{G}$ is the exponential gain factor in the low signal limit and θ_e^2 is the extinction ratio of the polarization analyzer. Figure 5 indicates a typical spectrum taken with ω_1 exactly on resonance and ω_2 scanned across the $^3P_0 \rightarrow {}^3H_6$ transition frequency. Theoretically an expression for the gain factor $\mathcal{G}$ can be derived using the plane wave approximation discussed in Section II, as in Eq. (27) of that section. The result given there is

$$\begin{aligned} \mathcal{G} &= 2\beta\,|(\chi_R)_{max}|\,|E(\omega_1)|^2 \\ &= \frac{16\pi^3}{n^2 c\lambda}\,|(\chi_R)_{max}|\;I(\omega_1)\;\mathcal{L} \end{aligned} \tag{9}$$

where $I(\omega_1)$ is the intensity at ω_1, $\mathcal{L}$ is the effective length described in Section IVC, n and λ are the index of refraction and wavelength for a mean frequency of the input frequencies. (An expression for $\mathcal{G}$ derived for Gaussian transverse profile beams is given in Ref. 16.) The maximum observed exponential gain factor was $\mathcal{G} = 0.27$ (for the spectrum shown in Fig. 5) with an intensity $I(\omega_1) \approx 100$ kW/cm^2 (derived from a power of only 20 W) and an effect length of 0.05 cm.

From Eq. (9) we find

$$(\chi_R)_{max} \approx 4.8 \times 10^{-8} \text{ esu}$$

with an estimated error of about ±30% due to the errors in measuring the intensity at ω_1 and the only approximate plane wave beam profiles.

From this value of $|(\chi_R)_{max}|$ we can now use the expression in Eq. (6) to determine the matrix element between the $^3P_0$ and $^3H_6$ states — the result being

$$|\mu_{n'g'}| \approx 9.7 \times 10^{-21} \text{ esu} .$$

which compares favorably with the value of 7×10^{-21} esu determined from the lasing threshold measurements, even though that derivation was somewhat crude.

Of interest also in this triple resonance case is the predicted lineshape of the susceptibility — both as a function of ω_1 and ω_2. Let us first discuss the dispersion of the peak value of χ_R as the frequency ω_1 is stepped across the absorption line. A series of scans — similar to that presented in Fig. 5 — were made to determine the lineshape of the RIKES susceptibility. After accounting for the changes in the linear absorption, the relative dispersion of $(\chi_R)_{max}$ is displayed in Fig. 6. The expected lineshape in this case can be found from the theory of Section IV.

Noting that we have found the most strongly resonant term of the unaveraged susceptibility to be (from Eq.(7), Section IV)

$$\chi_R = -i\frac{N|\mu_{n'g}|^2|\mu_{n'g'}|^2}{\hbar^3\Gamma_{n'n'}}\left\{\frac{1}{(\omega_1 - \omega_{n'g} - i\Gamma_{n'g})(\omega_2 - \omega_{n'g'} + i\Gamma_{n'g'})}\right\} \qquad (10)$$

we see this shows the form of a doubly-resonant susceptibility, with the extra resonance being the zero-frequency resonance previously described. Averaging over the assumed Gaussian distribution function, we find from Eq. (20) of Section IV,

$$\chi_R = -i\frac{N|\mu_{n'g}|^2|\mu_{n'g'}|^2}{\hbar^3\Gamma_{n'n'}}\left\{\frac{i\ 2(\pi\ell n2)^{\frac{1}{2}}\ e^{-\Delta\omega_1^2\ell n2/\gamma_{n'g}^2}}{\gamma_{n'g}[\omega^o_{g'g} - (\omega_1 - \omega_2) + i(\Gamma_{n'g'} + \Gamma_{n'g})]}\right\} \quad (11)$$

where the assumed Gaussian distribution manifests itself in the factor $\exp[-\Delta\omega_1^2\ell n2/\gamma_{n'g}^2]$ with $\Delta\omega_1 = \omega_1 - \omega^o_{n'g}$ and in $\gamma_{n'g}$ the inhomogeneous broadened width (which is assumed characteristic of the inhomogeneous widths of the transitions). From Eq. (11) we see that the magnitude of χ_R is maximized when $\omega_1 - \omega_2 = \omega^o_{g'g}$, and then we have

$$(\chi_R)_{max} \propto \exp[-\Delta\omega_1^2\ell n2/\gamma_{n'g}^2]$$

which implies $(\chi_R)_{max}$ has the same form as the linear absorption lineshape (assumed to be Gaussian in this case).

In Fig. 6(a) we have fitted the experimental data to a Gaussian profile and, like the linear absorption data, the fit is poor in the wings. In Fig. 6(b) we show a fit of the same data to a Lorentzian for comparison (Fig. 3(b) shows a similar fit for $\alpha(\omega_1)$). The approximate halfwidth from this data is about 11-12 GHz, in good agreement with the expected width ($\gamma_{n'g}$).

Examining the expression for χ_R given in Eq. (11), we also see that as we scan ω_2 for a fixed frequency ω_1, the expected lineshape is a simple Lorentzian with a width determined by the sum of the homo-

geneous widths. As described earlier, these widths are dominated by the laser bandwidths, so the sum is replaced by Γ_ℓ, the total laser bandwidth (each homogeneous halfwidth being replaced by a laser halfwidth). The scan in Fig. 5 with ω_1 on line center shows a halfwidth of approximately 4 to 5 GHz as expected; however, scans made with ω_1 detuned from line center show halfwidths of up to 8 GHz. This additional broadening is attributed to the "accidental degeneracy" effect discussed in Section IVB. Similar measurements made with narrower bandwidth lasers ($\Gamma_\ell \approx 1$ GHz) show that even for $\Delta\omega_1 = 0$ there is an additional width of 1 to 2 GHz, beyond that attributable to the lasers. There is no clear explanation why the accidental width should become larger in the wings of the absorption line.

In summary, the triply-resonant RIKES process does show the narrowing below the inhomogeneous width as predicted by the theory of Section IV. The nonlinear susceptibility in the case of Pr is dominated by a population term and has a peak value of $\sim 4.8 \times 10^{-8}$ esu. From this value we have estimated the dipole matrix element of the $^3P_0 \rightarrow {}^3H_6$ transition to be 9.7×10^{-21} esu. To complete the description of the observed spectra, we must include the presence of accidental degeneracy in the Pr^{+3}:LaF_3 system, which causes an additional broadening of the resonances.

D. Doubly-Resonant CARS — Raman Resonance

In Section IV we presented the form of the doubly-resonant CARS susceptibility and indicated that no narrowing below the inhomogeneous width is expected for a Raman-type resonance. However, the lineshape of the CARS signal does change dramatically as the input fre-

quency ω_1 is varied from below the resonance to above resonance. The variations of the resonant CARS lineshape for homogeneously broadened systems have been observed[17] and fully explained.[18] Let us briefly review these results before discussing the inhomogeneously broadened case.

For simplicity, consider a Raman susceptibility which is weak compared to the nonresonant background CARS susceptibility. As shown in Section II, the CARS lineshape (i.e. the CARS signal versus ω_2) will be carried on the cross term of $|\chi_{NR} + \chi_R|^2$, that is on the $2\chi_{NR}\mathrm{Re}[\chi_R]$ term. The dispersive part of the CARS signal is then directly proportional to the real part of χ_R. For doubly-resonant CARS we have from Eq. (4) of Section IV,

$$\chi_R \propto (\omega_1 - \omega_{n'g} + i\Gamma_{n'g})^{-1}(\omega_1 - \omega_2 - \omega_{g'g} + i\Gamma_{g'g})^{-1}$$

$$\propto (\omega_1 - \omega_{n'g} + i\Gamma_{n'g})^{-1}\,\mathscr{L}$$

and,

$$\mathrm{Re}[\chi_R] \propto f(\omega_1)\ \mathrm{Re}[\mathscr{L}] + g(\omega_1)\ \mathrm{Im}[\mathscr{L}] \tag{12}$$

where we have written $\mathscr{L}$ for the usual Lorentzian lineshape associated with the two-photon resonance of standard CARS, and we define $f(\omega_1)$ and $g(\omega_1)$ to be $\mathrm{Re}[(\omega_1 - \omega_{n'g} + i\Gamma_{n'g})^{-1}]$ and $-\mathrm{Im}[(\omega_1 - \omega_{n'g} + i\Gamma_{n'g})^{-1}]$, respectively. In the limit of ω_1 well below resonance with $\omega_{n'g}$, we have $|g(\omega_1)| << |f(\omega_1)|$ and the spectrum of $\mathrm{Re}[\chi_R]$ closely follows $\mathrm{Re}[\mathscr{L}]$, as in Fig. 7(a). As $\omega_1 \to \omega_{n'g}$ there is increased mixing of $\mathrm{Re}[\mathscr{L}]$ and $\mathrm{Im}[\mathscr{L}]$ until exactly on resonance we have

$$\mathrm{Re}[\chi_R] \propto \mathrm{Im}[\mathscr{L}]$$

as illustrated in Fig. 7(c). Hudson, et al.[17] have demonstrated actual CARS spectra which closely match those shown in Fig. 7.

In the case of an inhomogeneously broadened system we must first average the susceptibility as in Section IVB, with the resulting lineshape determined by the function $Z(\zeta)$, the plasma dispersion function (which is only available in tabulated form). The general variation of the CARS lineshape with ω_1 is still roughly the same as in the homogeneous case described above, except the homogeneous width is replaced by the inhomogeneous width (11 GHz) and the dispersion is somewhat more like a Gaussian. See Fig. 8(a) for the CARS lineshape derived from the plasma dispersion function when $\omega_1 = \omega_{n'g}$ and compare with the pure Lorentzian lineshape for the homogeneously broadened system exactly on resonance in Fig. 7(c).

To estimate the strength of the averaged doubly-resonant CARS susceptibility, we evaluate χ_R at its peak ($\omega_1 = \omega_{n'g}$ and $\omega_1 - \omega_2 = \omega_{g'g}$). The result is

$$(\chi_R)_{max} \cong -\frac{N\alpha_{g'g}\mu_{n'g}\mu_{n'g'}}{\hbar^2}\left[\frac{2\ln 2}{\gamma_I^2}\right] \tag{13}$$

where $\alpha_{g'g}$ is the Raman polarizability defined in conjunction with Eq. (4) of Section IV and γ_I is taken as the typical inhomogeneous width ≈ 11 GHz. The other parameters in Eq. (13) have been defined and evaluated earlier in this section; only the Raman polarizability is unknown.

We may crudely estimate the value of $\alpha_{g'g}$ for the $^3H_6$ to $^3H_4$

transition by assuming all matrix elements have a typical value of 2×10^{-21} esu, like the $^3H_4 \rightarrow {}^3P_0$ transition, so the factor $\mu_{gm}\mu_{mg'}$ may be removed from the summation. The sum over the energy denominators can then be explicitly calculated from the known energy levels of the Pr ions given by Karnall, et al.[2] This sum has a value of 1.3×10^{-2} $(cm^{-1})^{-1}$, indicating the effective energy difference of about 77 cm^{-1}. Therefore,

$$\alpha_{g'g} \approx 3 \times 10^{-28} \text{ esu}$$

in this case, which leads to a resonant susceptibility of

$$(\chi_R)_{max} \approx 3 \times 10^{-16} \text{ esu} .$$

Although this has been only an order of magnitude estimation, this value is very small compared to the familiar singly-resonant CARS susceptibility, e.g. the value of 3×10^{-13} esu for benzene. Of course, it must be kept in mind that this calculation is for a 1% doping level of Pr. If we try to use a higher concentration of Pr, the strength of $(\chi_R)_{max}$ will actually decrease, as follows. The resonant susceptibility in Eq. (13) is proportional to N/γ_I^2, and γ_I shows a dependence upon concentration which is roughly linear (see Ref. 5). Thus we find the strength of $(\chi_R)_{max}$ decreases as 1/N, so we should actually go to lower concentrations. However, if we attempt to use a lower concentration than 1%, the inhomogeneous width will quickly become comparable to the laser bandwidth (4 GHz), in which case the susceptibility will be limited by Γ_ℓ instead of γ_I. Thus, for the present

laser system, the choice of a 1% Pr doping level is nearly optimal.

As a final comment on this estimated strength of $(\chi_R)_{max}$ for CARS, we note that the doubly-resonant CARS susceptibility is about eight orders of magnitude lower than the triply-resonant RIKES susceptibility. This large factor is due almost entirely to the extra resonance in the triple resonance case, which leads to an enhancement factor of $\Delta\omega\tau_\ell$ (compare Eqs. (6) and (13) with $\Delta\omega$ being the effective frequency denominator in the Raman polarizability). With $\Delta\omega/2\pi c \cong 77\ cm^{-1}$ and $\tau_\ell \cong 0.4\ \mu sec$, we have $\Delta\omega\tau_\ell \approx 10^7$, with the extra order of magnitude coming from the different matrix elements and resonance linewidths involved in the two processes.

To complete the description of the expected CARS lineshape, it is necessary to determine the strength of the nonresonant CARS susceptibility which is due to the host crystal, LaF_3. Making a direct comparison of the nonresonant CARS signals for LaF_3 and carbon tetrachloride, we find $\chi_{NR}(LaF_3) \approx 1/15\ \chi_{NR}(CCl_4)$. Levenson and Bloembergen[19] have assigned a value of 1.1×10^{-14} esu to χ_{NR} in CCl_4, so we have

$$\chi_{NR}(LaF_3) \approx 7 \times 10^{-16}\ esu$$

This rather small nonresonant susceptibility can be attributed to the rather distant uv absorption bands in the LaF_3, which begin about 2000Å. Comparing this to the estimated resonant susceptibility, one finds

$$\chi_R(Pr)/\chi_{NR}(LaF_3) \sim 0.4$$

which would result in a CARS signal variation of about $2\chi_R/\chi_{NR}$ or 80%.

The experimental resonant CARS spectrum as shown in Fig. 8(b) and shows a modulation depth of about 20-30%, corresponding to $\chi_R(Pr)/\chi_{NR}$ $(LaF_3) \approx 0.1 - 0.15$. From this measured value of the ratio of susceptibilities, we can establish the experimentally derived value of the Raman polarizability. Using Eq. (13) we find

$$\alpha_{g'g} \sim 1. \times 10^{-28} \text{ esu}$$

with an error of about ±50% due to the poor signal to noise of the resonant CARS spectrum. Considering the gross approximations used to estimate the strength of $\alpha_{g'g}$, the factor of three difference between theory and experiment is somewhat fortuitous. Unfortunately the spectrum is quite noisy making it difficult to confirm many details of the lineshape. Other data at different $\Delta\omega_1$ frequency detunings also had noise which obsured the lineshapes. We now consider the sources of this noise and discuss an improved experimental apparatus to increase the signal to noise ratio.

As set forth in Section IIE, the formal signal to noise analysis gives the following result for conventional (amplitude-) CARS,

$$(\chi_R/\chi_{NR})_{min} = [\varepsilon + 1/N_p']^{\frac{1}{2}} \mathcal{N}^{-\frac{1}{2}} \tag{14}$$

where we have included the shot noise term as discussed in Section IIID (ε defined as the total mean square fluctuation due to either the laser fluctuations or the electronic noise; N_p' defined as the number of photoelectrons produced per shot, $N_p' = qN_p$ = quantum efficiency times the number of photons incident on the detector; $\mathcal{N}$ is the total number

of shots over which the signal is averaged). We evaluate Eq. (14) for the parameters relevant to the CARS system and laser system used in this measurement, in order to indicate which parts of the system need improvement before undertaking more accurate experiments.

The mean square fluctuation, ε, given by the weighted sum of the two input lasers' fluctuations $(4\varepsilon_1 + \varepsilon_2)$, is rather large in this case since the shot-to-shot variations of the laser intensities were greater than 30% for the ω_1 beam and about 10% for the ω_2 beam. The large fluctuations of the ω_1 beam were attributed to the fact that the laser could not be perated too far above threshold with the laser dye Coumarin 480 used in the wavelength range around 4778Å. We take $\varepsilon = 4(.30)^2 + (.10)^2 = 0.37$.

To evaluate the shot noise term in Eq. (14) we need an estimate of the total number of photons striking the detector, N_p. Directly terminating the PMT signal into 50Ω, only a random series of spikes corresponding to the CARS signal could be seen from which it was difficult to determine the average photocurrent. Rather than using photon counting equipment to determine N_p, we chose to use the known dependence of the CARS signal strength upon system parameters to extrapolate N_p in this situation from a known set of parameters taken with the $CC\ell_4$ sample. The system parameters spoken of here include: strength of the nonresonant susceptibility, the input intensities of the lasers, and the effective interaction length within the sample. The necessary information to determine $N_p(CC\ell_4)$ and $N_p(LaF_3)$ is given below:

For $CC\ell_4$:	$\chi_{NR} = 1.1 \times 10^{-14}$ esu	→ For LaF_3:	$\chi_{NR} = 7 \times 10^{-16}$ esu
	$P_1 = 1$ kW	→	$P_1 = 1$ kW
	$P_2 = 1$ kW	→	$P_2 = 10$ kW
	$A_1 = A_2 = 2 \times 10^{-4} cm^2$	→	$A_1 = A_2 = 2 \times 10^{-4} cm^2$
	$\mathcal{L} = 1.0$ cm	→	$\mathcal{L} = 0.1$ cm
	$\tau_\ell = 0.6$ μsec	→	$\tau_\ell = 0.4$ μsec

with the dependence of N_p being

$$N_p \propto \chi_{NR}^{\ 2}\ I_1^{\ 2}\ I_2\ \mathcal{L}^2\ \tau_\ell$$

where we have $I_{1,2} = P_{1,2}/A_{1,2}$.

In the case of $CC\ell_4$ we have measured a signal of 0.4V terminated into 50Ω with a photomultiplier of quantum efficiency of 15% and gain of 2×10^6, which leads to $N_p(CC\ell_4) = 1.0 \times 10^5$ photons/pulse.

Using the above information to evaluate the expected number of photons in the LaF_3 case, we have

$$N_p(LaF_3) = N_p(CC\ell_4)\left\{\left(\frac{7\times10^{-16}\text{esu}}{1.1\times10^{-14}\text{esu}}\right)^2\left(\frac{10\text{kW}}{1\text{kW}}\right)\left(\frac{0.1\text{cm}}{1\text{cm}}\right)^2\left(\frac{0.4\mu\text{sec}}{0.6\mu\text{sec}}\right)\right\}$$

$$= 3 \times 10^{-4}\ N_p(CC\ell_4) \approx 30 \text{ photons}$$

With the quantum efficiency of 15%, this corresponds to about 5 photoelectrons, N_p', to be used in Eq. (14). There is perhaps a factor of two uncertainty in this value of N_p' due to the large amount of information used in its determination.

With $\varepsilon = 0.37$ and $(N_p')^{-1} = 0.20$, we can evaluate the minimum detectable ratio of resonant to nonresonant susceptibilities. Previous experimental spectra were taken with 10 Hz laser repetition and 10 sec time constant, so $\mathcal{N} = 100$. We find

$$(\chi_R/\chi_{NR})_{min} \cong [0.37 + 0.20]^{\frac{1}{2}}(100)^{-\frac{1}{2}}$$

$$\cong 0.08$$

which would imply that the measured value of 0.1 - 0.15 would involve a signal to noise of ~ 1 - 2, in agreement with the spectrum of Fig. 8.

To improve the minimum detectable value of (χ_R/χ_{NR}), we should certainly try to reduce the laser fluctuations (decrease ε) by using a more stable laser system; however, even if $\varepsilon \to 0$, the shot noise contribution described above still limits detection to $(\chi_R/\chi_{NR})_{min}$ 0.04. To futher reduce the minimum detectable ratio, we must reduce the shot noise by increasing the number of photons over which we average the signal — either by increasing the number of photons/pulse or by increasing the number of pulses averaged. This is shown explicitly in Eq. (14) which we rewrite here with $\varepsilon = 0$,

$$(\chi_R/\chi_{NR})_{min} = (qN_p \cdot \mathcal{N})^{-\frac{1}{2}} \quad .$$

Thus, to improve the detection limit by a factor of 10, we can, for example, either increase N_p or $\mathcal{N}$ by a factor of 100. Averaging over 100 times more pulses is straight-forward but requires 100 times longer to make one spectrum, and so may be undesirable. As pointed

out in Section III, we can utilize the nonlinear nature of the output to fairly easily increase the number of signal photons. For example, the hundred fold increase in N_p requires an increase of a factor of only $(100)^{1/3} \approx 5$ in each of the input lasers' intensities. A factor which can be accomplished either by increasing the pulse energy, focussing more tightly, or using a shorter input pulse length.

In the case of $Pr^{+3}:LaF_3$, the restriction on the energy fluence due to saturation indicates that the best choice is to go to a shorter input laser pulse. If we assume that we are inputting the same pulse energy into the same area (i.e. the same energy fluence) as in the flashlamp-pumped dye laser case, then we require the pulse length to be decreased by a factor of 10 (down to 40 nsec) to achieve the desired two orders of magnitude increase in N_p. [Note: $N_p \propto \tau_\ell^{-2}$, not τ_ℓ^{-3}.]

The best choice for this $Pr^{+3}:LaF_3$ CARS experiment is to use a Nd:YAG-pumped dye laser system which can give comparable pulse energies (and bandwidths) to the flashlamp dye system, but has a pulse length of 4 - 5 nsec. This factor of 100 in pulse length will lead to a 10^4 increase in N_p and will make the shot noise contribution to the noise very small. Typical fluctuations for such a dye laser system are quoted as 8% (Ref. 20), and lead to $\varepsilon = 4\,\varepsilon_1 + \varepsilon_2 = 3.2 \times 10^{-2}$. Thus, averaging over 100 pulses, we find

$$(\chi_R/\chi_{NR})_{min} \approx 2 \times 10^{-2}$$

with this result dominated by laser fluctuations. With such a laser system we expect a signal to noise for the spectrum of Fig. 8 to be

10 - 15 as evaluated from Eq. (52) of Section II. With this system we should be able to not only make a more accurate determination of χ_R/χ_{NR} in this double resonance experiment, but also to do the line-shape studies of interest in this case.

E. Doubly-Resonant CARS — Upper State Resonance

Recently it has been pointed out that there should be another type of resonance in the four-wave mixing susceptibility — one involving the splitting of two excited states.[18a] This has been discussed theoretically in Section IVA in the context of an inhomogeneously broadened system and was found to show the "Doppler-free" narrowing below the inhomogeneous width. We consider here the determination of the resonant susceptibility for this process in Pr^{+3}:LaF_3 using the $^3P_0$ state previously described and the lowest lying level of the $^1D_2$ manifold (16872 cm^{-1}). We then describe a brief attempt to observe this "upper state resonance" process and suggest modifications to improve the experimental setup.

To estimate the peak strength of χ_R in this case we utilize the formalism of Section IV to write an expression for the peak, averaged susceptibility.

$$(\chi_R)_{max} \cong \frac{N\mu_{n'g}\mu_{gn}\alpha_{n'n}2(\pi\ell n2)^{\frac{1}{2}}}{\hbar^2\gamma_I\Gamma_\ell} \tag{15}$$

where one resonance denominator has been replaced by the typical inhomogeneous linewidth γ_I, while the second resonance denominator has been replaced by the larger of either the homogeneous width or the

laser linewidth (here the laser width is much broader). Also needed to evaluate Eq. (15) are the dipole matrix elements $\mu_{n'g} = \langle {}^3P_0|\mu|{}^3H_4\rangle$ and $\mu_{gn} = \langle {}^3H_4|\mu|{}^1D_2\rangle$ and the Raman polarizability between the excited states $\alpha_{n'n}$ as defined with Eq. (5) of Section IV. We have already determined $\mu_{n'g}$ earlier, and can estimate μ_{gn} from the linear absorption data given by Erickson.[21] The peak absorption coefficient of 2.6 cm^{-1} for the 16872 cm^{-1} line in a 1% doped sample indicates a value of $|\mu_{gn}| \cong 0.9 \times 10^{-21}$ esu. The Raman polarizability is again unknown and can be estimated in the same manner as in the previous segment. We find, $\alpha_{n'n} \approx 2 \times 10^{-28}$ esu. Evaluating Eq. (15) the peak resonant susceptibility becomes

$$(\chi_R)_{max} \sim 1.2 \times 10^{-17} \text{ esu}$$

so that the ratio of resonant to nonresonant susceptibilities is approximately 0.2. This is on the same order as in the Raman resonance case discussed in part D, but is again only an approximation due to the uncertainty in the estimation of $\alpha_{n'n}$. To experimentally determine this ratio we must investigate the dispersion of the nonlinear signal.

The simplest method of performing lineshape studies of the CARS spectra is to fix ω_1 near $\omega_{n'g}$ and to scan ω_2 around ω_{ng}. The expected lineshape for the resonant susceptibility is a Lorentzian involving the frequency offset of ω_2 from ω_{ng} and a width determined by the laser bandwidth (in the present case). With $\chi_{NR} >> \chi_R$ the spectra will display the cross term proportional to $Re[\chi_R]$ which (for the upper state resonance process) involves the imaginary part of the Lorent-

zian.

The nonlinear signal lineshape will also depend upon the variation of the effective interaction length $\mathcal{L}$ defined in Section IVC. Considering the most strongly resonantly enhanced case — ω_1 exactly on resonance — the length $\mathcal{L}$ will be determined by the strong absorption at ω_1 and shows only a few percent variation due to the absorption at ω_2. Thus, in this case, the dispersion in the CARS signal comes only from the spectral variation of $\mathrm{Re}[\chi_R]$.

The experimental arrangement used in this CARS measurement was identical to that used in the previous section, except that shorter pulsed Nd:YAG-pumped dye lasers were used for the input beams. As we have seen above, the minimum detectable ratio of susceptibilities for such a system (with 8% laser fluctuations) is expected to be $(\chi_R/\chi_{NR})_{min} \approx 0.02$. This leads to an anticipated $S/N \approx 10$ if the estimated value of the χ_R/χ_{NR} ratio is 0.2 for the upper state resonance in Pr.

Regrettably, the first attempts at developing the Nd:YAG-pumped dye lasers did not yield as stable of system as is commercially available. In fact, even after averaging over 100 pulses, the CARS output signal still showed a fluctuation of 5%. Thus the value of $(\chi_R/\chi_{NR})_{min}$ for this system was ≈ 0.05, which implies the expected signal to noise ratio was reduced to about 4. A brief attempt to observe such an upper state resonance signal did not reveal any resonance above the noise; therefore, we conclude that $\chi_R/\chi_{NR} \leqslant 0.05$ for this particular set of transitions.

Several improvements have been made in the experimental setup since the time of this attempt. Dye laser fluctuations have been

reduced by a factor of three using a more carefully optimized design, and a new computer-based data acquisition system has been developed which allows shot-to-shot data analysis. In addition, the larger laser intensities may allow either the use of an independent reference cell to normalize the nonlinear signal or the use of the polarization-sensitive techniques discussed in Sections II and III. With these improvements, it should be possible to detect a minimum ratio of χ_R/χ_{NR} of 0.02 and perhaps see the theoretically predicted upper state resonance in CARS.

To summarize this section, we have presented experimental proof that certain four-wave mixing processes can lead to a linewidth much less than that due to inhomogeneous broadening. This was demonstrated using the triply-resonant RIKES process in a study of $Pr^{+3}:LaF_3$. Using a combination of linear and nonlinear spectroscopic techniques, we have evaluated the dipole matrix elements involved in this RIKES susceptibility. In particular, we found $\langle {}^3P_0|\mu|{}^3H_4\rangle \approx 2.2 \times 10^{-21}$ esu and $\langle {}^3H_6|\mu|{}^3P_0\rangle \approx 9.7 \times 10^{-21}$ esu. From the strength of a doubly-resonant CARS spectrum, involving the same levels, we have found the Raman polarizability between the ${}^3H_6$ and ${}^3H_4$ states to be approximately $1. \times 10^{-28}$ esu. We have also included several suggestions about improvements which could be made (and some of which have already been made) to make these measurements more precise.

References

1. R. W. G. Wycoff, Crystal Structure, Vol. 2, p. 60 (John Wiley & Sons, New York, 1964); Landolt-Börnstein, vol. LBIII/7a, p. 23 (Springer-Verlag, New York, 1973).
2. W. T. Karnall, P. R. Fields, and R Sarup, J. Chem. Phys. 51, 2587 (1969).
3. M. P. Wirick, Appl. Opt. 5, 1966 (1966); American Institute of Physics Handbook, 3rd ed., p. 6-33 (McGraw-Hill, New York, 1972).
4. W. M. Yen, W. C. Scott, and A. L. Schawlow, Phys. Rev. 136, A271 (1964).
5. R. Flach, D. S. Hamilton, P. M. Selzer, and W. M. Yen, Phys. Rev. B15, 1248 (1977).
6. M. J. Weber, J. Chem. Phys. 48, 4774 (1968).
7. W. F. Krupke, Phys. Rev. 145, 325 (1966).
8. C. Kittel, Introduction to Solid State Physics, 4th ed., p. 509 (John Wiley & Sons, New York, 1971).
9. H. Takeuchi, J. Lumines. 12/13, 743 (1976).
10. R. Solomon and L. Mueller, Appl. Phys. Lett. 3, 135 (1963).
11. J. T. Hougen and S. Singh, Phys. Rev. Lett. 10, 406 (1963).
12. The apparatus is similar to the one described in Section III and the references therein.
13. G. F. Imbush, W. M. Yen, A. L. Schawlow, D. E. McCumber, and M. D. Sturge, Phys. Rev. 133, A1029 (1964).
14. See, for example, R. H. Pantell and H. E. Puthoff, Fundamentals of Quantum Electronics, p. 71 (John Wiley & Sons, New York, 1969).
15. ibid., p. 107.

16. A. Owyoung and E. D. Jones, Opt. Lett. 1, 152 (1977).

17. B. Hudson, W. Hetherington, S. Cramer, I. Chabay, and G. Klauminzer, Proc. Nat. Acad. Sci. Wash. 73, 3798 (1976).

18. (a) R. T. Lynch, Jr., H. Lotem, and N. Bloembergen, J. Chem. Phys. 66, 4250 (1977).

(b) L. A. Carriera, L. P. Goss, and T. B. Mallory, J. Chem. Phys. 66, 2762 (1977).

(c) F. Lau, M. Pfeiffer, and W. Werncke, Opt. Commun. 23, 59 (1977).

19. M. D. Levenson and N. Bloembergen, J. Chem. Phys. 60, 1323 (1974).

20. Quanta-Ray, 1250 Charleston Rd., Mountain View, Ca.

21. L. E. Erickson, Phys. Rev. B11, 77 (1975).

Figure Captions

Fig. 1 Level diagrams for $Pr^{+3}:LaF_3$. (a) Approximate energies of various manifolds ($^1S_0$ at 46986 cm^{-1} not shown); (b) levels studied in this work.

Fig. 2 Linear absorption measurement setup to study $^3H_4 \rightarrow {}^3P_0$ transition. BS beamsplitter, NDF neutral density filter, PD photo diode. Electric field polarized perpendicular to the c-axis of sample.

Fig. 3 Experimentally determined absorption lineshape. (a) Gaussian fit to central part of the profile; (b) Lorentzian fit to same data — both with peak height of 19 cm^{-1} and HWHM of 11 GHz. (See text for discussion of lineshape.)

Fig. 4 RIKES setup used to study the $^3P_0 \rightarrow {}^3H_6$ transition. P1 and P2 polarizers, P3 linear analyzer (polarizer), L1 and L2 lenses, S sample, D diaphragm, W1 quarter-wave plate, F color filter (to block fluorescence from sample), PD photodiode.

Fig. 5 RIKES spectrum with ω_1 exactly on resonance. Plot of output signal through crossed polarizer as ω_2 is scanned.

Fig. 6 Peak RIKES susceptibility as ω_1 is scanned across the one-photon resonance. (a) Gaussian fit to data; (b) Lorentzian fit to same data. (See text for discussion and compare to Fig. 3.)

Fig. 7 Resonant CARS lineshapes as ω_1 is tuned through a one-photon resonance (for homogeneously broadened system). (a) $\Delta\omega_1 \equiv \omega_1 - \omega_{n'g} = -100\ \Gamma_{n'g}$; (b) $\Delta\omega_1 = -\Gamma_{n'g}$; (c) $\Delta\omega_1 = 0$; (d) $\Delta\omega_1 = +\Gamma_{n'g}$. Vertical scale arbitrary; each plot with different

baseline. $|\chi_R| << |\chi_{NR}|$ assumed.

Fig. 8 Doubly-resonant CARS spectra for Pr^{+3}:LaF_3 system, involving the $^3H_4$, $^3P_0$, and $^3H_6$ levels. (a) Theoretical curve derived using the tabulated plasma dispersion function and assuming $\chi_R/\chi_{NR} = 0.15$ with ω_1 exactly on resonance; (b) experimental curve also with ω_1 exactly on resonance; (c) experimental curve with ω_1 about six inhomogeneous halfwidths below resonance (the latter is included to indicate the noise level in the otherwise nondispersive nonlinear signal).

Figure 1

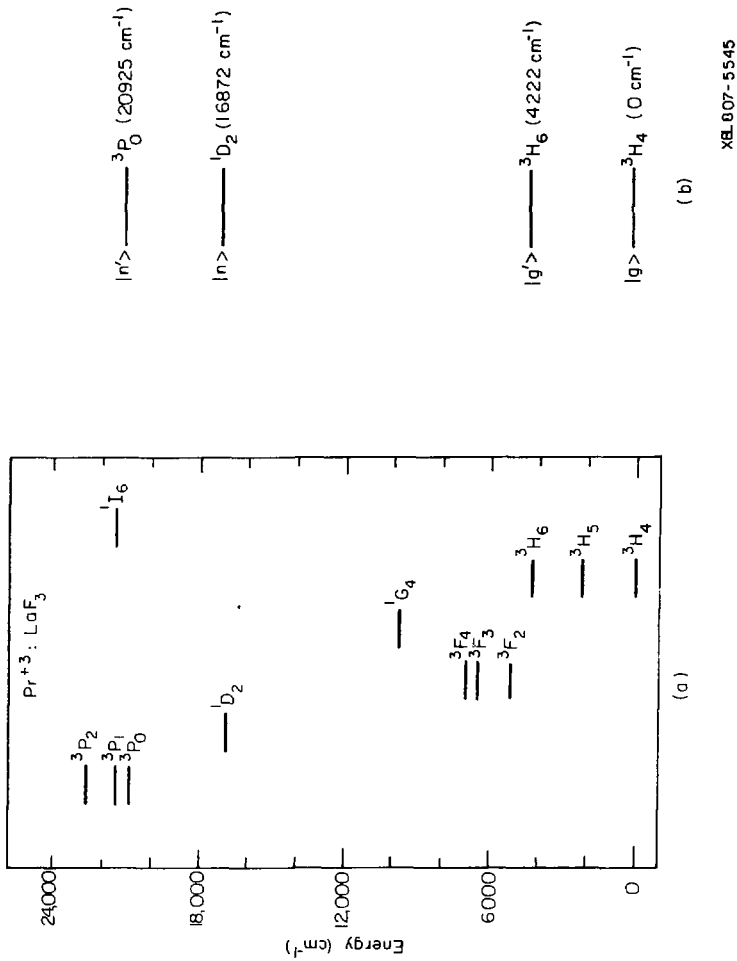
Pr+3 : LaF3
Energy (cm-1)
24,000
18,000
12,000
6000
0
3P2
3P1
3P0
1I6
1D2
1G4
3F4
3F3
3F2
3H6
3H5
3H4
(a)
|n'> 3P0 (20925 cm-1)
|n> 1D2 (16872 cm-1)
|g'> 3H6 (4222 cm-1)
|g> 3H4 (0 cm-1)
(b)
XBL 807-5545

Figure 2

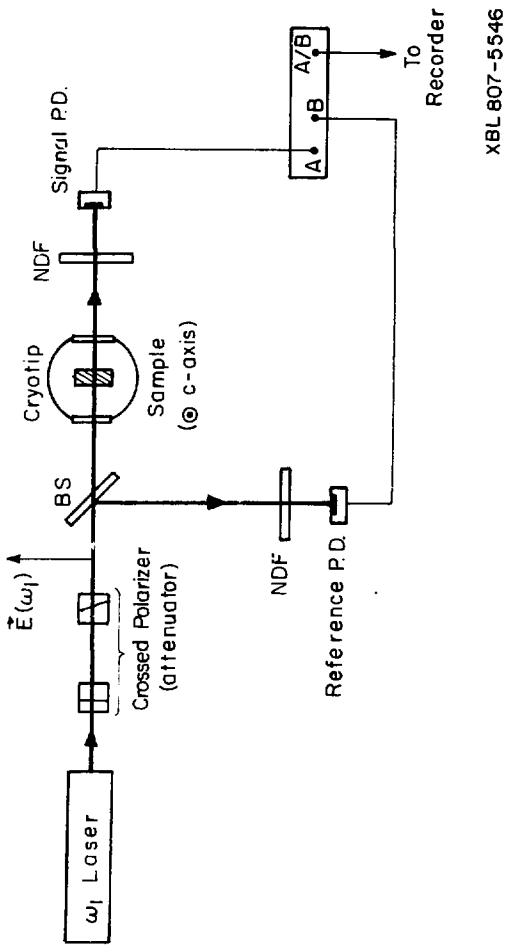
ω_1 Laser
$\vec{E}(\omega_1)$
Crossed Polarizer
(attenuator)
BS
Cryotip
Sample
(⊙ c-axis)
NDF
Signal P.D.
NDF
Reference P.D.
A
B
A/B
To
Recorder
XBL 807-5546

Figure 3

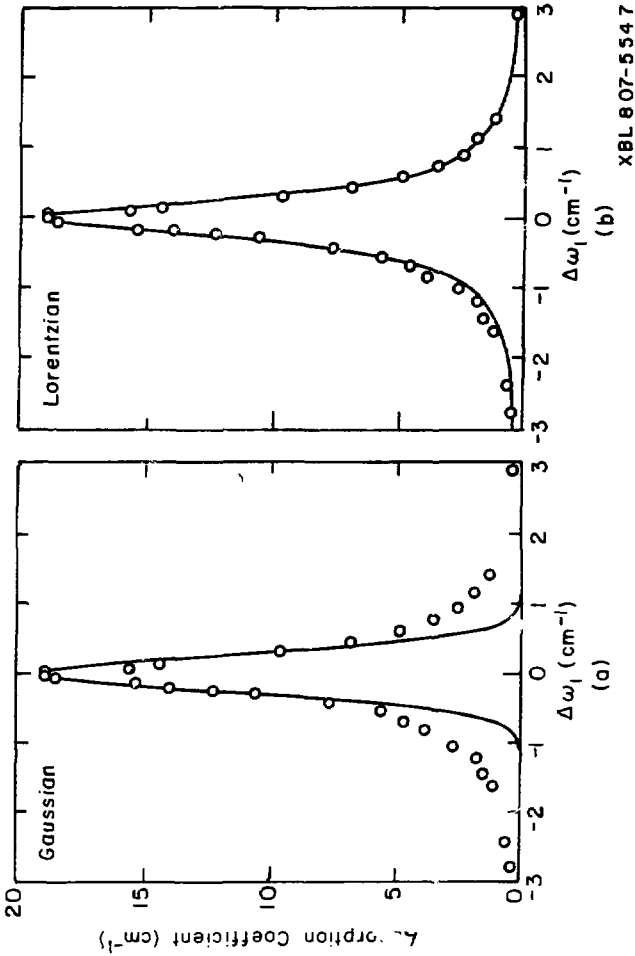
Gaussian
Lorentzian
Absorption Coefficient (cm⁻¹)
20
15
10
5
0
-3
-2
-1
0
1
2
3
Δω_l (cm⁻¹)
(a)
(b)
XBL 807-5547

Figure 4

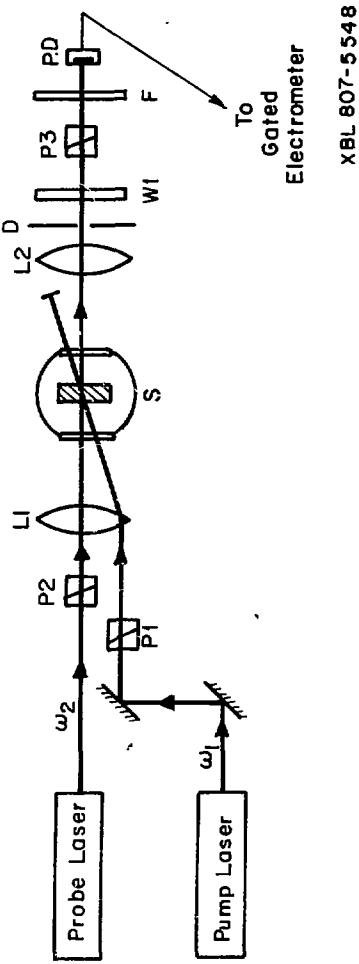
Probe Laser
Pump Laser
ω_2
ω_1
P1
P2
L1
S
L2
D
W1
P3
F
PD
To
Gated
Electrometer
XBL 807-5548

Figure 5

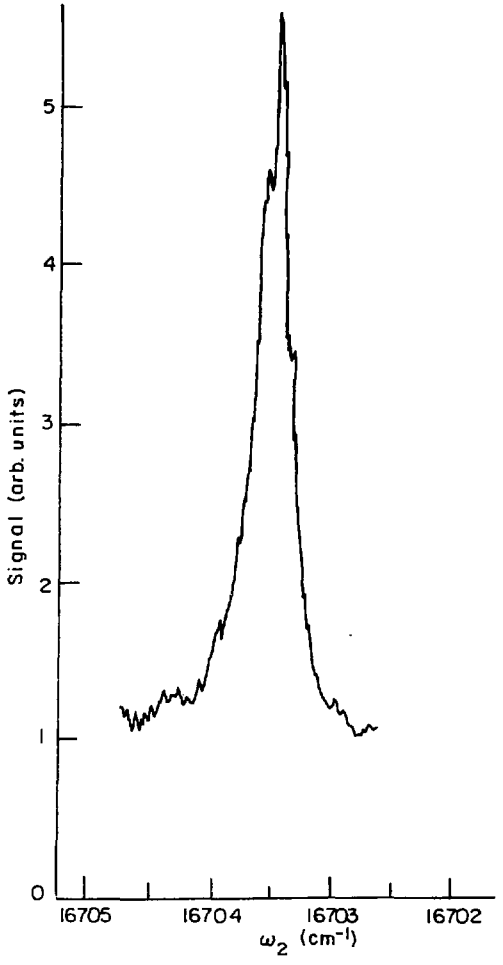

XBL 807-5549

Figure 6

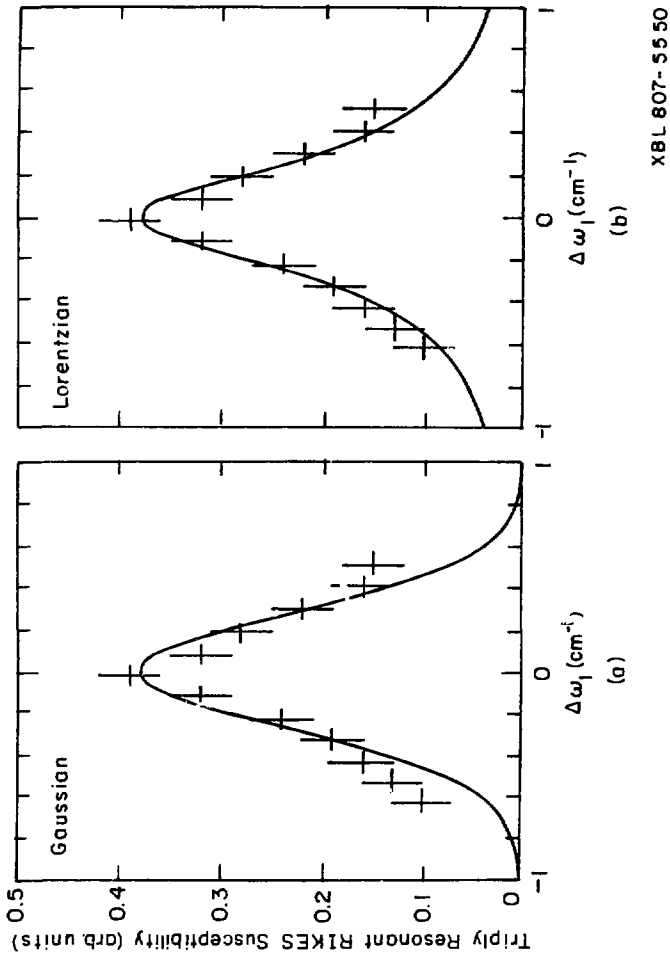
Triply Resonant RIKES Susceptibility (arb. units)
0.5
0.4
0.3
0.2
0.1
0
Gaussian
Lorentzian
−1
0
1
$\Delta\omega_1$ (cm^{-1})
(a)
(b)
XBL 807-5550

Figure 7

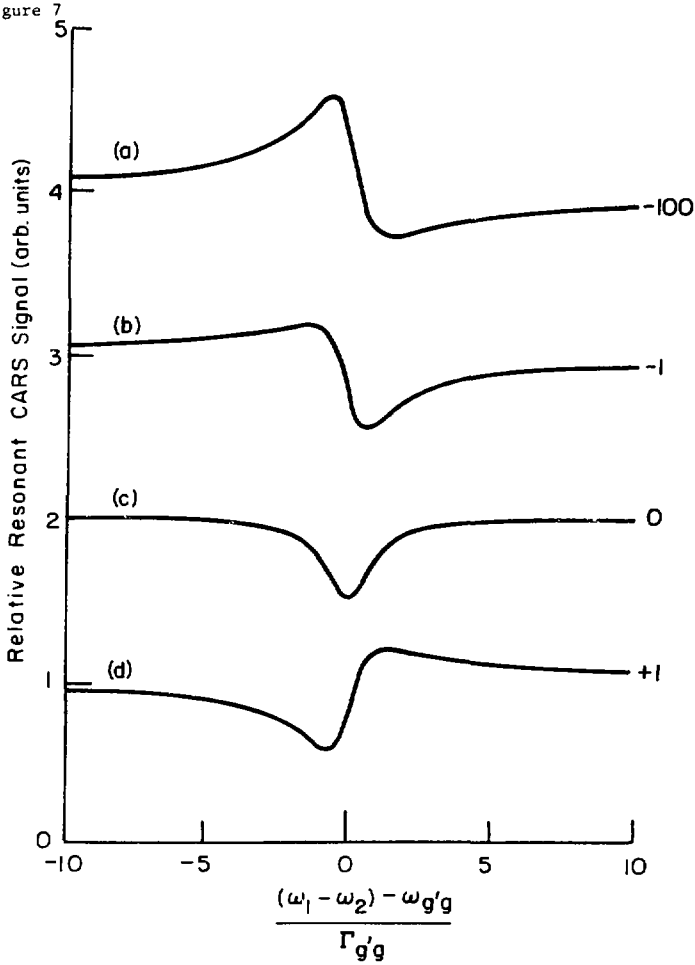

XBL 807-5551

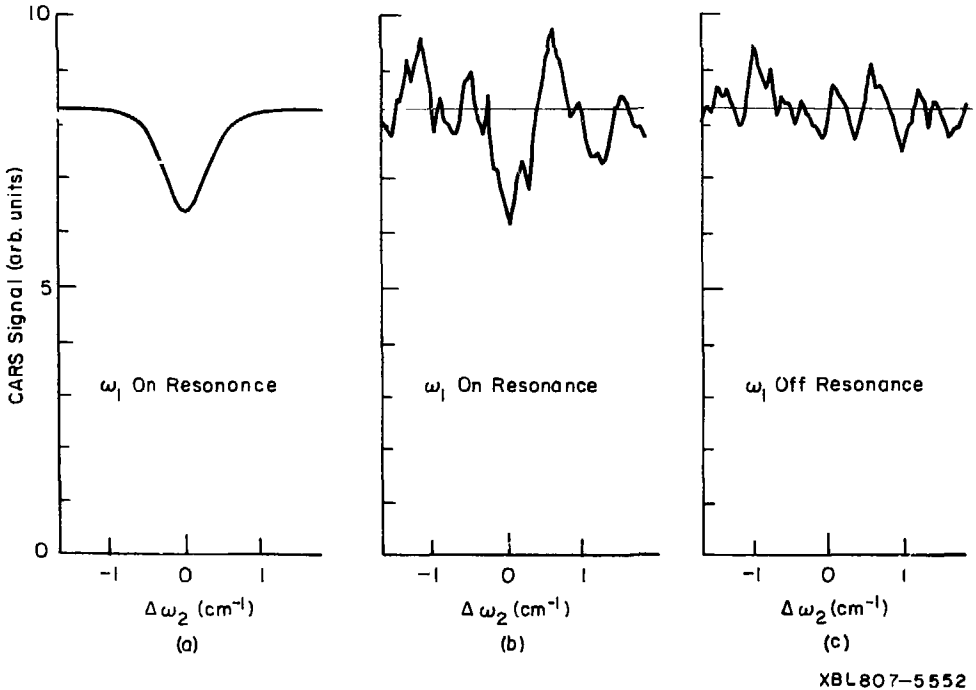
10
5
0
CARS Signal (arb. units)
ω1 On Resonance
ω1 On Resonance
ω1 Off Resonance
-1
0
1
Δω2 (cm-1)
(a)
(b)
(c)
XBL807-5552

Figure 8